Experimental, Numerical and Theoretical Study of Bias Flow Acoustic Liners

ラムダニ, スフィアン

https://doi.org/10.15017/2534452

出版情報：九州大学, 2019, 博士（工学）, 課程博士
バージョン：
権利関係：

Experimental, Numerical and Theoretical Study of Bias Flow Acoustic Liners

Supervisor: Prof. Nobuhiko Yamasaki

Examiners: Prof. Ken-ichi Abe

Prof. Masato Furukawa

Soufiane Ramdani

Kyushu University, Graduate School of Engineering

Department of Aeronautics and Astronautics

2019/07

Acknowledgments

My deep thanks go to my supervisors in the Aerospace Propulsion Laboratory Prof. Yamasaki and Mr. Inokuchi, for their guidance and recommendations and for their extraordinary support and patience all along the duration of this research.

I would like to express my gratitude to Dr. Ishii and Dr. Nagai from Japan Aerospace Exploration Agency for their numerous discussions and recommendations on different research matters.

I would like to thank Prof. Ken-ichi Abe and Prof Masato Furukawa for taking the time to examine this thesis.

I also wishes to thank Kyushu University faculty responsible for the education of the Aeronautics and Astronautics engineering students.

I would like to thank Ms. Tanaka for providing experimental data for different acoustic liners.

Thanks to the JAXA team developing the CFD tool used in this research.

I would like to thank the engineering student office and particularly Ms. Oiwa for her considerable help and support.

I sincerely thank my parents and siblings for their encouragement and moral support despite the long distance between us.

This project would have been impossible without the opportunity offered to me by the MEXT Scholarship program.

The computation was mainly carried out using the computer facilities at the Research Institute for Information Technology in Kyushu University.

Contents

Nomenclature

x	Coordinate along the i-direction
y	Coordinate along the j-direction
z	Coordinate along the k-direction
u	Velocity along the i-direction
v	Velocity along the j-direction
w	Velocity along the k-direction
x_i	Indicial notation of coordinate components
u_i	Indicial notation of velocity components
ϕ	Physical propriety
$\overline{\phi}$	Filtered physical propriety
$\tilde{\cdot}$	Favre filter operation of physical propriety
$\hat{\cdot}$	Quantity based on filtered variables
Δ	Cutoff width
G	Filtering kernel
ς_{SGS}	Error introduced by the discretization
ς_M	Error introduced by the difference by the SGS model
ς_N	Truncation error
M_{SGS}	SGS model
t	Time
p	Pressure
ρ	Density
u_i	Velocity component in the i-direction
σ_{ij}	Viscous stress tensor
τ_{ij}	Turbulent stress tensor
$\tilde{S}_{ij}$	Strain tensor
E	Total energy
q_j	Heat flux vector

ν_t	Eddy viscosity
C_s	Constant of Smagorinsky
γ_{ij}	Velocity gradient tensor
V_c	Vreman constant
B_β	Flow function
R	Reflection coefficient
I	Sound intensity
α	Absorption coefficient
Φ	Viscous dissipation function
$\overline{D}(x,y,z)$	Time-averaged dissipation rate
$E^s_{incident}$	Acoustic power through the aperture
$E^t_{incident}$	Acoustic power through the impedance acoustic tube
$E^{\mathrm{v}}_{\mathrm{viscous}}$	Acoustic power converted to viscous dissipation
h	Thickness of the perforated plated
D	Width of the straight aperture
l	Depth of the cavity
W	Width of the cavity
d	Distance between slits
b	Width at the base of trapezoidal shape of the tapered aperture
a	Width at the top of trapezoidal shape of the tapered aperture
Z_0	Characteristic impedance of air
Z_{t}	Total impedance of a Helmholtz resonator
Z_{cavity}	Impedance of the cavity of a Helmholtz resonator
Z_{aperture}	Impedance of the aperture of a Helmholtz resonator
$Z_{\mathrm{Str.aperture}}$	Impedance of the straight aperture
$Z_{Tap.aperture}$	Impedance of the tapered aperture
r	Resistance of the aperture
X	Reactance of the aperture
f_0	Resonant frequency
δ	End correction
m	Tapering slope

η	Effective compliance
Q	Volume flow rate through the aperture
M	Bias flow Mach number

List of Tables

List of Figures

I. Introduction

During the last decades, the world had experienced a continuous increase in the development and manufacturing of airplanes due to the travel time reduction and the safety this means of transportation offers. Moreover, the introduction of low-cost carriers made it possible for a huge number of people to travel via airplanes, and thus increased the demand for airplanes. Air traffic has improved people's quality of life and made it possible to shrink the world borders. Besides this, it also created thousands of jobs all around the world. However, this beneficial increase in air traffic was accompanied by an increase of multiple environmental pollutions.

One environmental pollution is the increase of greenhouse gases exhausted out of jet engines including a large amount of carbon dioxide which is detrimental to global warming, as well as pollutant emissions such as Nitrogen oxides NOx. Recent combustion chambers, aimed at low NOx emission and high combustion efficiency, tend to decrease the secondary air flow, which leads to increase the vibration in the combustion chambers caused by combustion instabilities.

The second environmental pollution is the noise produced by airplanes. Taking off and landing of large passenger airplanes are the noisiest periods during the flight which may influence on the comfort of people living in the residential areas around the airports.

The objective of this research is to study the acoustic liners used in turbofan engines to reduce the generated noise as well as the combustion instabilities, and to elucidate the influence of a bias flow passing through a perforated face sheet on the absorption capabilities of acoustic liners.

1. Background

1.1. Engine Noise

Noise certification regulation

The widespread usage of large passenger airplanes and the annoyance caused by their noise made it a necessity to quantify the noisiness of airplanes. The International Civil Aviation Organization (ICAO) is an agency of the United Nations, which ensures safe planning and development of international air transport, and the noise certification for airplanes is one of the missions that this agency deals with.

The Effective Perceived Noise level in decibel (EPNdB) is a number used to evaluate the loudness of an airplane for a human being on the ground, and it is calculated as the sum of the Effective Perceived Noise Level (a measure of sound level that takes into account the annoyance of spectral irregularities and the duration on human beings) on three different points situated nearby the runway as shown in Figure I-1:

- During takeoff at a microphone at a distance of 6.5km from the brake release.
- During takeoff at a microphone situated at a distance of 400m from the runway center
- During landing at a microphone at a distance of 2km from the runway threshold.

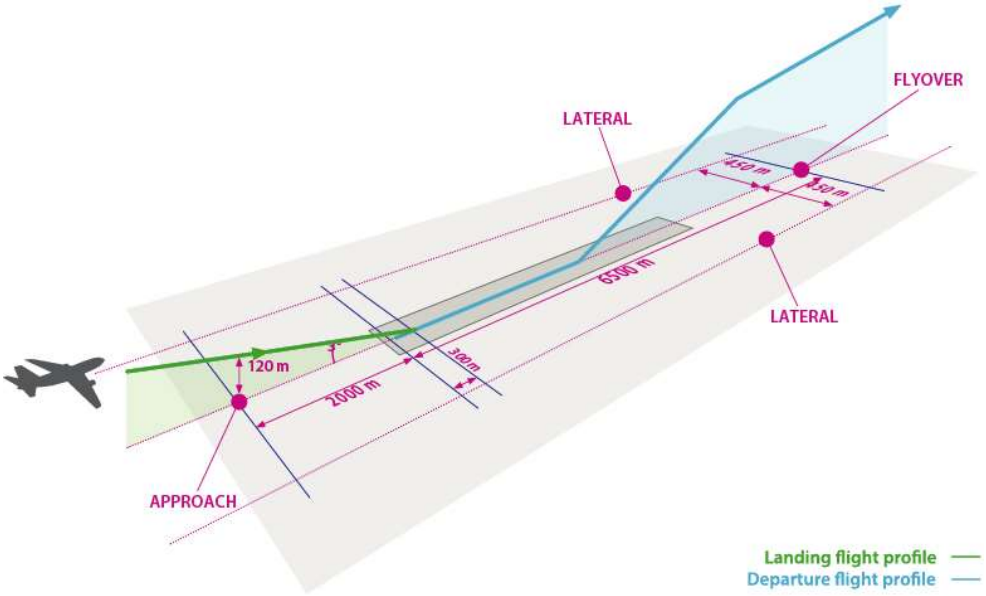

Figure I-1 Noise certification reference points [1]

Figure I-2 shows the certification levels since the issuance of Chapter 2 (effective since 1972) until Chapter 14 (effective for all the new airplanes produced after 2017).

Chapter 4 is aiming to reduce the allowable SPL by 10dB over the limit of Chapter 3, and Chapter 14 is a revision of Chapter 4 in which the limit is reduced by 7dB compared to Chapter 4 and an extra elbow is added to the curve in order to account for the noise of lightweight airplanes, and this adds an extra constraint for lightweight airplane manufacturers.

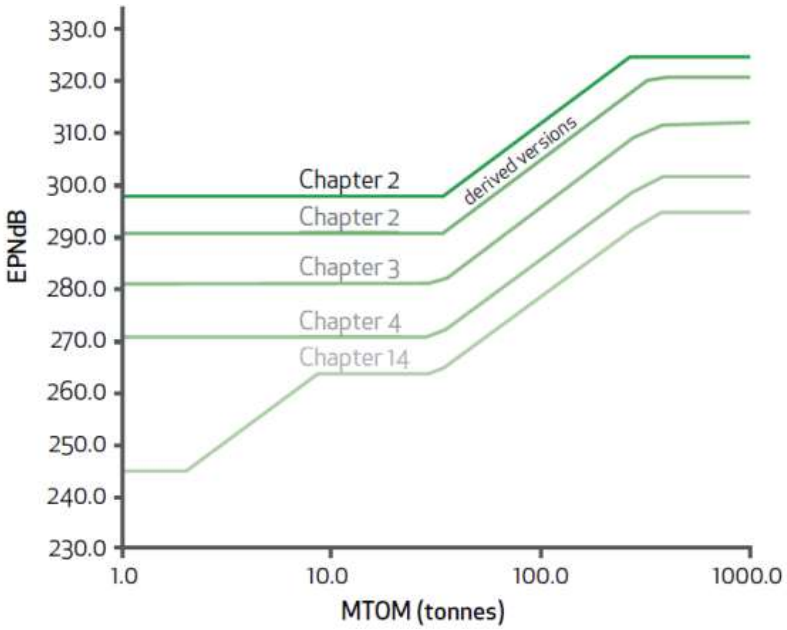

Figure I-2 ICAO noise standards [2]

Such stricter standard has a role to motivate airplane and airplane engine manufacturers to continuously improve the existing noise reduction devices as well as to develop new technologies in order to meet the even stricter standard in the future.

Noise sources

For large passenger airplanes with turbofan engines, noise sources are classified into two, i.e., the primary noise source consist of the engines noise, while the secondary noise source is the airframe noise.

Figure I-3 shows the different sources of noise generated in the turbofan engines. The noise sources are classified into turbomachinery and jet sources.

The turbomachinery sources consist of the fan, compressor, combustor as well as turbine, whereas jet sources consist of the core mixing (mixing between hot-core and the fan-bypass air flows) and bypass mixing (mixing between the fan-bypass and surrounding air flows).

The fan noise consist of a broadband noise in addition to the tone noise. The tone noise is of high sound pressure level (SPL) and caused by the spinning of the fan with a specific frequency. Such that the fundamental frequency of the produced sound is the blade passing frequency BPF and it is calculated as the number of blades N_R of the fan times its rotational speed Ω.

$$BPF = N_R \times \Omega \tag{I.1}$$

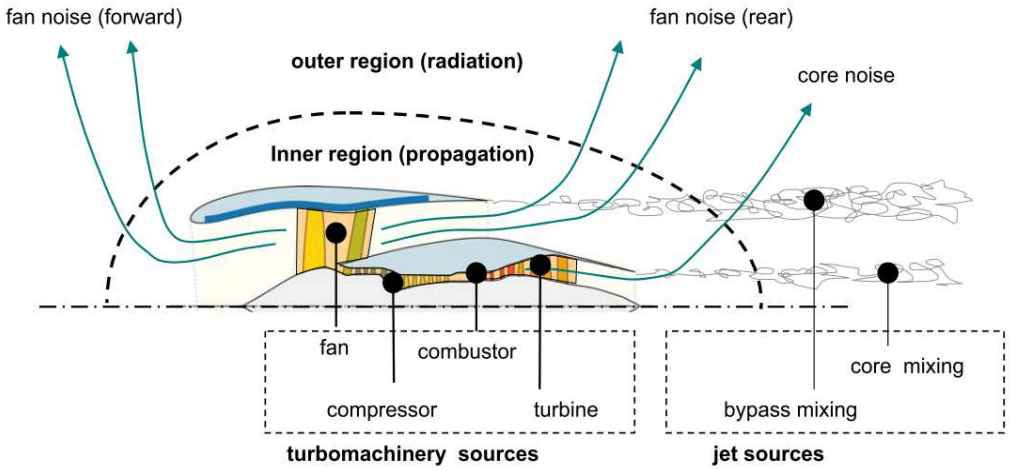

Figure I-3 Turbo fan noise sources [3]

Figure I-4 shows the levels of noise generated by different components of large passenger airplanes during takeoff and landing, and the main source of noise in the current airplanes is produced by the engines during takeoff. In addition to the engines, the airframe also produces a high noise level during landing due to the deployed flaps and landing gears in landing configurations.

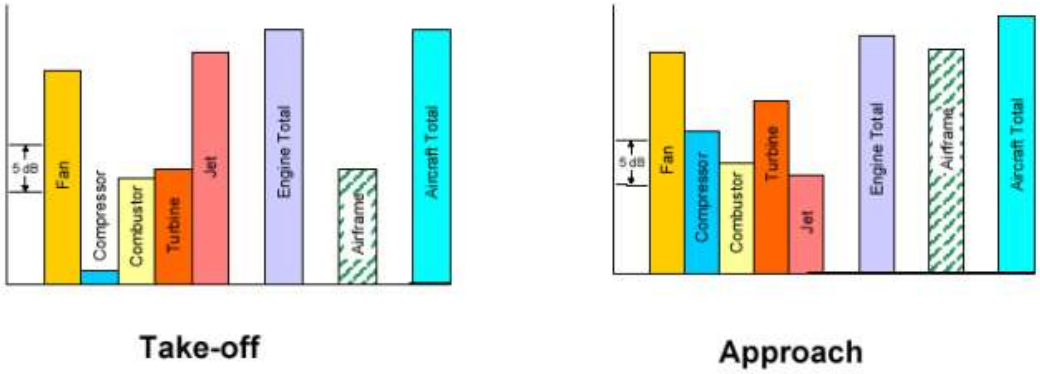

Figure I-4 Airplane noise components [4]

Figure I-4 shows also that the highest noise is produced by the fan in case of approach while in the case of takeoff both jet and fan noises are predominant noise sources.

1.2. Combustion instabilities

In order to reduce exhausted pollutant emissions of Nitrogen oxides NOx out of jet engines, recent combustion chambers use lean premixed combustion technology.

The fuel and air are premixed in advance before entering the combustion chamber. This helps homogenize the mixture leading to more uniform temperature as well as a reduced flame temperature. Such a combustion results in low NOx emission and high combustion efficiency. However, since the lean mixture is already rich in oxygen, contrary to old generation combustors, recent combustion chambers, aimed at low NOx emission and high combustion efficiency, tend to decrease the secondary air flow. This leads to undesirable combustion phenomena such as a lower stability flame and combustion dynamic phenomena giving rise to the vibration in combustion chambers, and one of these dynamic phenomena is the thermo-acoustic instabilities.

Figure I-5 shows a multi-burner assembly damaged by combustion instabilities as a result of lean premixed combustion. And Figure I-6 shows a new multi-burner assembly. These Figures show the irreversible damage that can occur to the combustor if combustor stability is not taken into account by dampening thermos-acoustic instabilities.

Figure I-7 show a schematic of a combustion duct were an unsteady flame results in generation of sound waves. Dynamic oscillations in the combustion chamber is related to conditions where a resonant coupling occurs between perturbations in the heat release and pressure field. In these conditions where the heat release perturbations is in phase with an acoustic wave, the results can be damaging as shown in Figure I-5. The aforementioned

condition is referred to as Rayleigh's criterion. Putnam [5] formulated mathematically this criterion giving the following equation:

$$\frac{1}{T}\int_0^T p'q'dt > 0 \qquad \text{(I.2)}$$

where p' denotes pressure fluctuations, q' denotes heat release oscillations and T is a period of time.

One of the methods to solve this thermo-acoustic instability problem is to dissipate the acoustic waves enough to eliminate the acoustic oscillations. This method is studied further in the present research.

Figure I-5 burner assembly damaged by combustion instability [6]

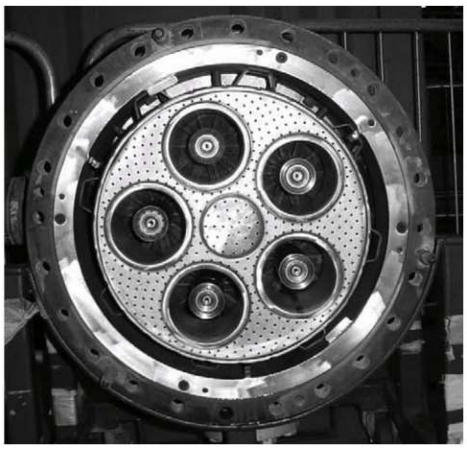

Figure I-6 New burner assembly [6]

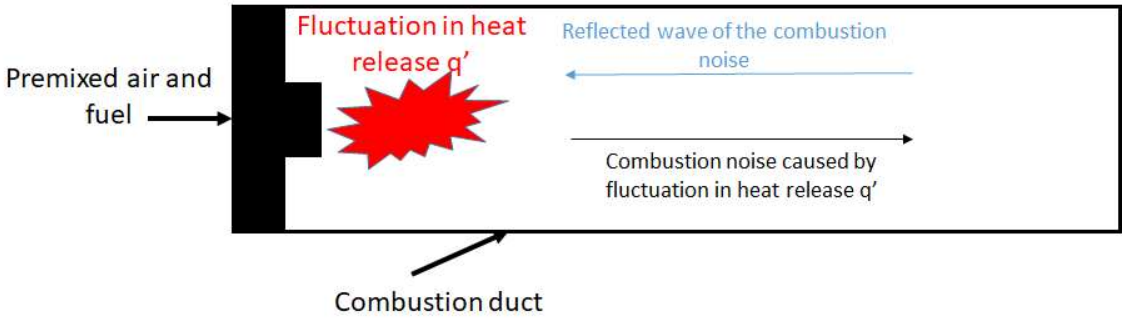

Figure I-7 Schematic of thermo-acoustic coupling in a combustion duct.

1.3. Noise reduction technologies

Different means have been used in order to reduce the noise generated by turbofan engines such as installing chevrons or virtual chevrons [4] dealing with the jet noise, and acoustic liners in order to reduce fan noise [7]. In this study, we will focus on the conventional and active acoustic liners with bias flow.

Acoustic liners are used nowadays on most passenger airplanes because of their simplicity and effectiveness to attenuate fan noise.

Figure I-8 shows the locations where the acoustic liners are installed. For noise reduction, the main location is along the inner wall of the nacelle, and the liners installed in this area are conventional acoustic liners and have the main function of reducing the acoustic noise, however, the acoustic liners are also installed in the combustor in order to reduce combustion instabilities generated by acoustic waves. The liners in the combustor have a bias flow passing through the aperture, where bias flow is caused by the secondary air flow in the combustor.

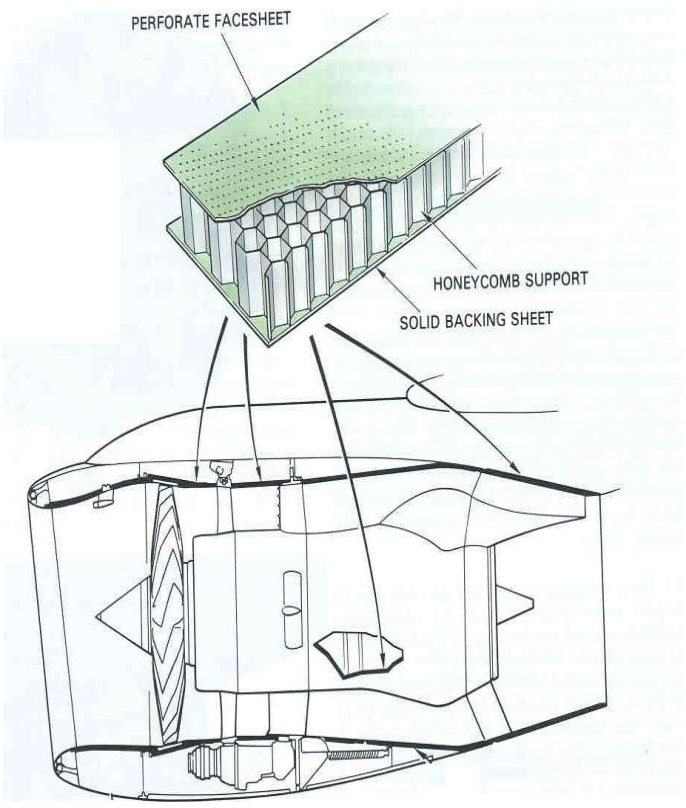

Figure I-8 Location of acoustic liners *[32]*

As shown in Figure I-9, the acoustic liners consist of a perforated plate backed by a hard wall, with honeycomb support used to separate the two plates. They are fixed in the inner walls of the engine nacelle, in order to damp acoustic waves produced by the fan.

Conventional acoustic liners are known to well absorb acoustic energy in the range of frequency close to the resonance frequency. The noise produced by the engine, however, is broad, there comes the need for active acoustic liners, in order to optimally change the impedance of the liner to match the operating conditions of the engine. Various methods are used to technically realize active liners such as controllable piezoelectric [8] or bias flow [9] which is the topic of the present study.

However active acoustic liners are still under investigation, an active method in this research refers to a method which adds mass, momentum or energy into the system, and these active methods are studied and developed to be further improved over the effectiveness of the conventional passive liner. Moreover, recent combustion chambers, aimed at low NOx emission and high combustion efficiency, tend to decrease the secondary air, which leads to increase the vibration in combustion chambers.
This is why understanding how to keep the attenuation or damping performance with little secondary air is important. To realize it, we study the attenuation mechanism of the bias flow type liners.

Figure I-10 shows an active acoustic liner where the blue arrows denote the direction of a bias flow passing through the backed plate.

The reason for which a steady bias flow is chosen can be made clear by considering the formulae of the rate of dissipation of acoustic energy given in the textbook by Howe [10].

$$\prod_{\omega} \approx \rho \int \mathbf{u} \cdot (\boldsymbol{\omega} \times \mathbf{v}) d^3\mathbf{x} \tag{I.3}$$

where ρ is the density, $\mathbf{u}$ is the acoustic particle velocity, $\boldsymbol{\omega}$ is the vorticity, and $\mathbf{v}$ is the velocity.

As demonstrated by Howe, the order of the term $\boldsymbol{\omega} \times \mathbf{v}$ is equal to ε, the measure of the acoustic amplitude. Moreover the acoustic particle velocity $\mathbf{u}$ only have the acoustic part and it is of the order of ε, and as a result, the rate of production of vortical energy $\prod_{\omega}$ is of second order ($\sim O(\varepsilon^2)$). On the other hand, in the case of the acoustic model with no bias flow, both the velocity $\mathbf{v}$ and the vorticity $\boldsymbol{\omega}$ are of the order of ε, thus $\boldsymbol{\omega} \times \mathbf{v}$ is of second order ($\sim O(\varepsilon^2)$), leading to the production of vortical energy $\prod_{\omega}$ of third order($\sim O(\varepsilon^3)$). As a conclusion, the bias flow increases the rate of dissipation of acoustic energy in Eq. (I.3) by an order of magnitude.

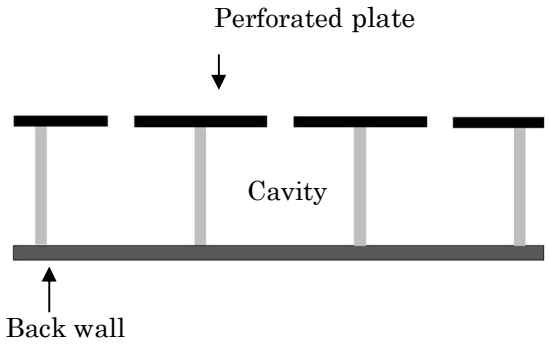

Figure I-9 Layout of acoustic liners.

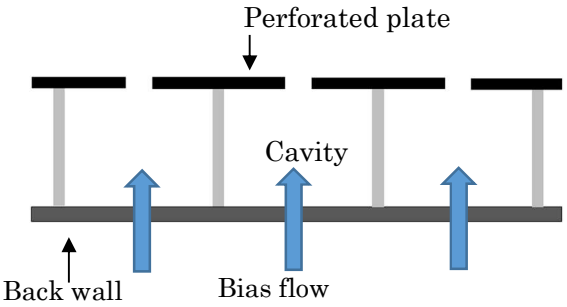

Figure I-10 Acoustic liner with bias flow

2. Literature Survey

Howe [11] theoretically proposed that a low frequency (low Strouhal number) sound wave can be significantly attenuated by a jet flow by converting the acoustical energy into energy of fluctuating vorticity, which is shed from the nozzle edge. Bechert [12] proposed another theory to explain this phenomenon, and this was supported via experimental data. Bechert [12] also proposed a simple theory to predict the optimum Mach number of bias flow to obtain the perfect attenuation. On the other hand, Howe's theory to predict the sound absorption coefficient including the effects of a bias flow is well supported by an experiment by Hughes and Dowling [13]. Hence, this led to the idea that the off-resonant performance of a resonator can be improved if a jet (or a bias flow) is introduced from an aperture of an acoustic liner. Lahiri et al. [14] collected this type of experimental data and showed that the application of a bias flow through the aperture widens the frequency range of dissipation, with the penalty of reduced peak performance near the resonant frequency. Zhao and Li [15] wrote a summary on tunable acoustic liners including a liner with bias flow.

In the field of numerical simulation, Mendez et al. [16] performed a 3D simulation of a perforated plate with a circular aperture using the large eddy simulation (LES), and the results showed that LES can predict the acoustic behavior of resonators, and flow fields around the aperture can give an insight to the dissipation mechanism of acoustic liners. Then Mendez applied a homogeneous model of multi-perforated plates to an actual gas turbine combustor chamber, where the walls contain huge amount of holes. This method represents a fast and practical alternative to include the influence of perforated plates to the simulation.

Ji and Zhao [17] performed a 2D lattice Boltzmann method (LBM) for an aperture with bias flow, and both made a comparison with Howe's theory, obtaining good agreements.

Roche et al. [18] conducted a 3D as well as 2D axisymmetric numerical simulation of cylindrical acoustic liner under a normal incidence acoustic wave for different frequencies as well as sound pressure levels. They used the Direct Numerical Simulation (DNS) and good agreement was obtained between the theoretical model, 2D and 3D models concerning the acoustic properties such as reflection and absorption coefficients for a low SPL of 80dB which is considered within the linear domain. However in the case of high sound pressure level of 150db where non-linearity has large influence, this linear theoretical model is not describing the acoustic behavior properly anymore, but good agreement is obtain between 2D and 3D models, and this shows that by opting for a 2D simulation, calculation time can be reduced enormously without a loss in the accuracy of the results. Also, it is observed that a wider absorption spectra and lower peaks are obtained.

DNS simulations were conducted by Tam et al. [19] for a 2D slit resonator of resonance frequency around 1 kHz for a range of frequencies of sound source from 1 kHz to 6 kHz and sound pressure levels of 130dB and 150dB. The absorption coefficients were obtained by evaluating the absorbed energy as the sum of the rate of viscous dissipation and the rate at which the energy is transferred to shed vortices. These simulations were validated by experiments using an acoustic impedance tube, in the same conditions. Good agreement

was obtained for the absorption coefficients, except for the case of sound source of 2 kHz and 130db where the experimental value is much larger than the simulation.

Tam et al. [19] distinguish two regimes with regard to the mechanisms through which the absorption phenomena occurs in acoustic liners:

- The low sound pressure level regime where the primarily mechanism of absorption is the viscous dissipation caused by the oscillatory boundary layer at the aperture of the perforated plate.

- The high-pressure level regime where vortices develop at the opening of the aperture then they are shed away. The absorption is caused by a conversion of acoustic energy to vortical energy that is dissipated later on by viscous effects.

Tam et al. [19] also conducted a series of experiments and Direct Numerical Simulation (DNS) to slit apertures with a 90° corner (straight aperture) and 45° corner (tapered aperture). The results obtained using the simulation supports the usage of computational aeroacoustics (CAA) as a design tool.

Zhang, Q et al. [20] studied a two-dimensional resonator under normal acoustic wave, using DNS, and he validated his results using experimental data by Tam, et al. [21], where he found that the results of the experiment and the simulation are in good agreement, also he worked on the problem including a grazing flow which models actual conditions in operating engines.

In the experimental field, Wada and Ishii [9] performed experiments for acoustic liners with a bias flow passing through the apertures of a perforated plate (circular straight perforations) and observed that the absorption range of the liner became wider and was not concentrated around the resonant frequency as in the case of the conventional liner. They compared the experimental results with Howe's extended theory proposed by Luong et al. [22], which considered the thickness of the perforated sheet and obtained good agreements.

The macroscopic effect of the design parameters (such as the shape of the aperture and the flow velocity when a bias flow is applied through the aperture) on the impedance of an acoustic resonator was experimentally investigated via an acoustic impedance tube. The results revealed that the fully tapered aperture exhibited a wider absorption frequency range when compared to that of a straight circular aperture. However, little was known about the reason for such a behavior given the difficulty of visualizing the flow around the small apertures in the experimental setup using the impedance tube.

In the present study, the acoustic performance of the liner and the flow field around the perforated plate is numerically solved using the compressible Navier-Stokes equations to understand the acoustic and fluid dynamic behavior of the liner and the effect of the shape of the perforation at a microscopic level.

The aforementioned studies involve a long computational time and computational resources to perform 3D simulations. Thus, in the present study, the simulations are conducted using 2D large eddy simulations. For the 2D assumption to be acceptable, the impedance tube experiment is conducted on slit apertures where slit indicates that each plate has only one aperture with a high aspect ratio of 100. The aperture spans through the center of the plate. Subsequently, numerical simulations are conducted to focus on the

effect of bias flow on the absorption performance of the acoustic liner and flow field around the apertures.

In the next chapter, the details of the numerical code and the models used are explained, then the implementation of the sound source and mass source to generate the acoustic waves and the bias flow are given while in Chapter 3 the methods used for post-processing are explained.

In Chapter 4, the impedance tube experiment is conducted on slit apertures where slit indicates that each plate has only one aperture with a high aspect ratio of 100. The aperture spans through the center of the plate.

In Chapter 5, the numerical simulations conducted for conventional and active acoustic liners are validated with the results obtained from the experimental section. The simulations are conducted using 2D large eddy simulations, and are conducted to focus on the effect of bias flow on the absorption performance of the acoustic liner and flow field around the apertures.

In Chapter 6, the theoretical models are developed by modifying the model by Hughes and Dowling [23] for a screen with slit apertures in order to account for the thickness as well as the cross-section of the aperture of the plate. The results are then compared to the experimental and numerical results from the previous chapters.

Finally, few conclusions of the results obtained during this research are reported in Chapter 7.

Chapter 2

II. Numerical Methods

Nowadays numerical methods are widely used tools in many fields of engineering such as structural analysis, fluid dynamics, electromagnetic…, it is a mathematical field that implements algorithms in the interest of obtaining numerical solutions to problems defined by continuous functions.

The extensive use of these methods is for the reason that complex geometries that wouldn't be solved analytically can be modeled numerically with usually a great accuracy for engineering purposes. In addition, the advent of supercomputers and the immense improvement of the calculation capabilities of computers made it possible to deal with much more complex problems along with a reduction in computational time.

This chapter intends to explain the numerical methods employed in this research. By understanding the physics and models in conjunction with the numerical schemes used, meaningful comparative conclusions can be drawn.

All the simulations in this study are carried out with the large eddy simulation (LES) code upacs-LES developed by Japan Aerospace Exploration Agency (JAXA), which solves the compressible Navier Stokes equations by Finite Volume Method for multi-block structured mesh.

The 6^{th}-order compact scheme with the 10^{th}-order compact filter is used to solve the convective terms of the conservation equations, while the second order central discretization is used for the viscous terms.

The obtained space discretized equations are then integrated in time using the 3rd order Runge-Kutta explicit scheme.

Henceforth the conservation equations of fluid dynamics are derived in order to understand the physics behind Computational Fluid Dynamics and Computational Aeroacoustics. The finite volume method is introduced, then its application to the Navier Stokes equations is demonstrated. The interpolation using high-order compact schemes is made clear and a basic explanation of the large eddy simulation formulation is given next.

1. Conservation Laws governing Fluid Dynamics

In fluid dynamics, flowing fluid is studied to calculate properties such as density, pressure, velocity, temperature …

These properties can be determined using the conservation laws of mass, momentum, and energy. They are stipulated as it follows:

-the conservation of mass states that the rate of change of mass in a control volume is equal to the net change of mass flux over the control surfaces.

-the rate of change of momentum is equal to the sum of forces applied on the fluid element surfaces.

-the rate of change of energy is equal to the sum of the heat added to the fluid element and to the work done into it.

The governing equations can be summarized in vectorial form as in Eqs. (II.1) to (II.5). For convenience, the components of coordinates and velocity are written in their indicial notation as x_i and u_i respectively, with i from 1 to 3.

$$\frac{\partial \boldsymbol{Q}}{\partial t} + \frac{\partial \boldsymbol{F}^{C}{}_{j}}{\partial x_j} + \frac{\partial \boldsymbol{F}^{V}{}_{j}}{\partial x_j} = \boldsymbol{S} \tag{II.1}$$

$$\boldsymbol{Q} = \left[\rho, \rho u_i, E\right]^{\mathrm{T}} \tag{II.2}$$

$$\boldsymbol{F}^{C}{}_{j} = \left[\rho u_j, \rho u_j u_i + p\delta_{ij}, \rho u_j H\right]^{\mathrm{T}} \tag{II.3}$$

$$\boldsymbol{F}_{V_j} = \left[0, -\tau_{ij}, -\tau_{ij} u_i - \kappa \frac{\partial T}{\partial x_j}\right]^{\mathrm{T}} \tag{II.4}$$

$$\boldsymbol{S} = \left[S_1, S_2, S_3, S_4, S_5\right]^{\mathrm{T}} \tag{II.5}$$

Where $\boldsymbol{Q}$ in Eq. (II.2) represents the conservative variables vector composed of density, momentum vector and energy.

Eqs. (II.3) and (II.4) represent consecutively the convective and diffusive terms. While Eq. (II.5) is the source term where S_1 is the mass source, S_2 S_3, S_4 are the momentum sources in three directions and S_5 is the energy source.

In general the source term $\boldsymbol{S}$ is considered to be null, however, in the present formulation and because of the need to create the mass source for the bias flow and the sound source, the

source term $\boldsymbol{S}$ has a finite value in specified regions where sound source and mass source are implemented.

Since the governing equation are for the compressible case, the closer is achieved using the equation of state for perfect gas.

$$p = \rho RT \tag{II.6}$$

The viscous stress in Eq. (II.4) is calculated by Eq. (II.7).

$$\tau_{ij} = 2\mu S_{ij} \tag{II.7}$$

Where viscous strain-rate is defined by Eq. (II.8):

$$S_{ij} = \frac{1}{2}\left(\frac{\partial u_i}{\partial x_j} + \frac{\partial u_j}{\partial x_i} \right) - \frac{1}{3}\frac{\partial u_k}{\partial x_k}\delta_{ij} \tag{II.8}$$

2. Calculation method

2.1. Finite volume method

The finite volume method is used in order to solve partial differential equations, and it is widely used in Computational Fluid Dynamics and Computational Aeroacoustics for certain advantages over the finite difference method.

The first advantage is that the discretization is conservative because it is applied to the integral form of the governing equations to be solved

The second advantage is that it doesn't need coordinate transformation and thus it can be applied to both structured and unstructured grids.

The concept behind the finite volume method begins by introducing the integral form of the Navier Stokes equations (II.1) over a control volume $V(t)$ function of time.

$$\frac{\partial}{\partial t}\int_{V(t)} \boldsymbol{Q} dV + \oint_{S(t)} \boldsymbol{n}\bullet\left(\boldsymbol{F}^{C}{}_{j} + \boldsymbol{F}^{V}{}_{j}\right) dS = \frac{\partial}{\partial t}\int_{V(t)} \boldsymbol{S} dV \qquad \text{(II.9)}$$

Where

$\boldsymbol{Q}$: conserved variables in vector form

$\boldsymbol{F}^{C}{}_{j}$: The convective fluxes of conserved variables

$\boldsymbol{F}^{V}{}_{j}$: The viscous flux of conserved variables

$\boldsymbol{n}$: Unit normal vector directed outward of the surface

$\boldsymbol{S}$: Rate of production of $\boldsymbol{Q}$

The numerical calculation of Eq. (II.9) by the Finite Volume Method require several modeling technics.

The first model is to give the center point of each grid the average value of the property in consideration as in Eq. (II.10) and (II.11).

$$\bar{\boldsymbol{Q}} = \frac{1}{V}\int_{V(t)} \boldsymbol{Q} dV \qquad \text{(II.10)}$$

$$\bar{\boldsymbol{S}} = \frac{1}{V}\int_{V(t)} \boldsymbol{S} dV \tag{II.11}$$

By this model, Eq. (II.9) can be written for a fixed control volume as in Eq. (II.12).

$$V\frac{\partial}{\partial t}\bar{\boldsymbol{Q}} + \oint_{S(t)} \boldsymbol{n}\bullet\left(\boldsymbol{F}^{C}{}_{j} + \boldsymbol{F}^{V}{}_{j}\right) dS = \bar{\boldsymbol{S}} \tag{II.12}$$

The numerical calculations is then performed such that first the conservative variables are calculated at the boundaries of each control volume cell, once their values are known at the center of the cell. By using these values it is possible to calculate at the boundaries the convective flux in Eq. (II.3) as well as the viscous flux in Eq. (II.4).

In section 2.2 the calculation of the viscous fluxes using the second-order central difference scheme is explained while in section 2.3 the calculation of the convective fluxes using the 6th order compact scheme is discussed.

Figure II-1 shows a structured grid, with Cartesian coordinate convention. Eq. (II.13) is the discretized form of Eq. (II.12) that can be numerically solved.

$$\bar{\boldsymbol{Q}}^{n+1} = \bar{\boldsymbol{Q}}^{n} + \frac{\Delta t}{\Delta V}\boldsymbol{F}(Q) \tag{II.13}$$

In Eq. (II.13), $\bar{\boldsymbol{Q}}^{n}$ is the conserved variables at a step time *n while* $\bar{\boldsymbol{Q}}^{n+1}$ is the conserved variables at step time *n+1.*

The calculation of the flux term of the conservative variables $\boldsymbol{F}(Q)$ for the control surface encompassing the control volume represented here by a cell grid as given in Figure II-1. The calculation method is given in Eq. (II.14). Here $\boldsymbol{F}^{C}{}_{i+1/2}$ and $\boldsymbol{F}^{V}{}_{i+1/2}$ are respectively the convective and viscous fluxes at the boundaries of the cell with a cell center coordinates $[i, j, k]^{\mathrm{T}}$. The coordinates at the center of the boundaries in the i direction are at coordinate $[i+1/2, j, k]^{T}$ and $[i-1/2, j, k]^{T}$. The j and k directions are treated in the same manner.

$$
\begin{aligned}
\boldsymbol{F}(\boldsymbol{Q}) = \Big\{ & \Big[\Big(\boldsymbol{F}^{C}{}_{i+1/2} \cdot \boldsymbol{n} dS_{i+1/2} - \boldsymbol{F}^{C}{}_{i-1/2} \cdot \boldsymbol{n} dS_{i-1/2} \Big) \\
& + \Big(\boldsymbol{F}^{C}{}_{j+1/2} \cdot \boldsymbol{n} dS_{j+1/2} - \boldsymbol{F}^{C}{}_{j-1/2} \cdot \boldsymbol{n} dS_{j-1/2} \Big) \\
& + \Big(\boldsymbol{F}^{C}{}_{k+1/2} \cdot \boldsymbol{n} dS_{j+1/2} - \boldsymbol{F}^{C}{}_{k-1/2} \cdot \boldsymbol{n} dS_{j-1/2} \Big) \Big] \\
& + \Big[\Big(\boldsymbol{F}^{V}{}_{i+1/2} \cdot \boldsymbol{n} dS_{i+1/2} - \boldsymbol{F}^{V}{}_{i-1/2} \cdot \boldsymbol{n} dS_{i-1/2} \Big) \\
& + \Big(\boldsymbol{F}^{V}{}_{j+1/2} \cdot \boldsymbol{n} dS_{j+1/2} - \boldsymbol{F}^{V}{}_{j-1/2} \cdot \boldsymbol{n} dS_{j-1/2} \Big) \\
& + \Big(\boldsymbol{F}^{V}{}_{k+1/2} \cdot \boldsymbol{n} dS_{j+1/2} - \boldsymbol{F}^{V}{}_{k-1/2} \cdot \boldsymbol{n} dS_{j-1/2} \Big) \Big] \Big\}
\end{aligned}
\tag{II.14}
$$

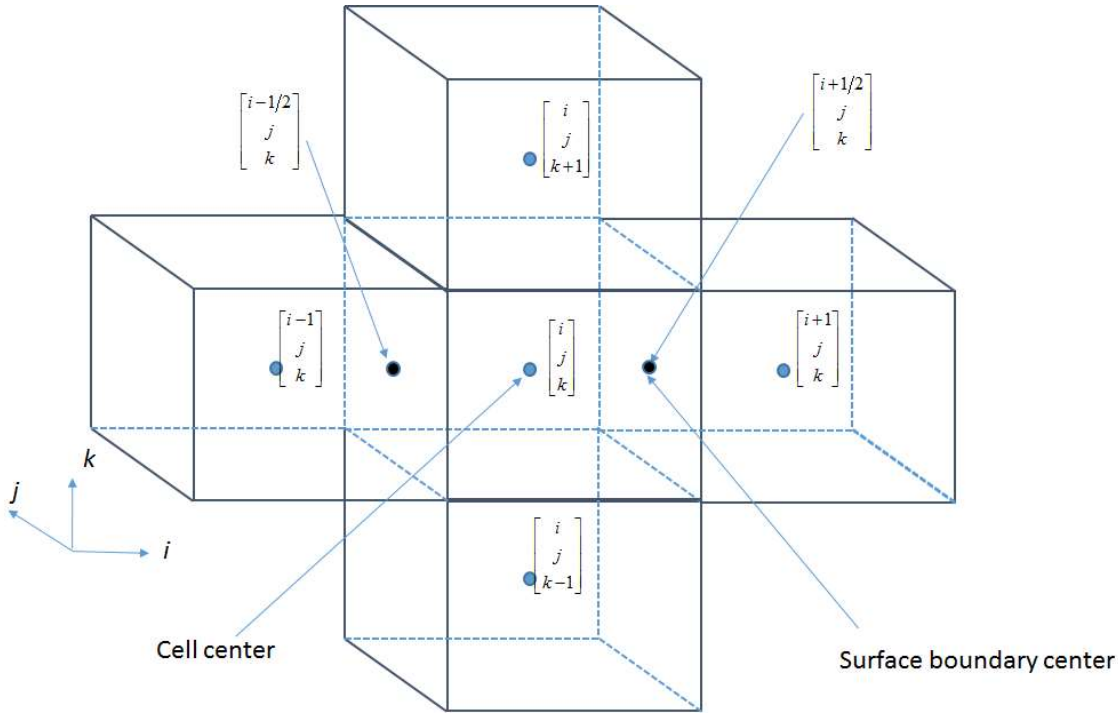

Figure II-1 Coordinates at the center and surface boundaries

2.2. Second order central difference

The accuracy of a numerical scheme, in general depends of the applied approximations. In this research the viscous terms of the governing equations in Eq. (II.4) are discretized using the second order central differentiation scheme.

Let ϕ_j be the physical property at the cell-centered node to be approximated. Let $\bar{\phi}_j$ be the cell average of the chosen physical property and the approximated value of ϕ_j, this is due to the use of the Finite Volume method that is basically applied to integral forms of conservative variables as shown in Eqs. (II.9), (II.10) and (II.11).

By replacing the integrand in Eq. (II.10) using the Taylor series expansion at the center of the cell we can write

$$\bar{\phi}_j \equiv \frac{1}{V}\int_{-\Delta x_1/2}^{\Delta x_1/2}\int_{-\Delta x_2/2}^{\Delta x_2/2}\int_{-\Delta x_3/2}^{\Delta x_3/2}\left[\phi_j + \sum_{l=1}^{3}\zeta_l\left(\frac{\partial\phi}{\partial x_l}\right)_j + \frac{1}{2}\sum_{l,m=1}^{3}\zeta_l\zeta_m\left(\frac{\partial^2\phi}{\partial x_l\partial x_m}\right)_j + \ldots\right]d\zeta_1 d\zeta_2 d\zeta_3 \qquad \text{(II.15)}$$

Where $\boldsymbol{h}=\begin{bmatrix}h_1 & h_2 & h_3\end{bmatrix}^{\mathrm{T}}$ is the local Cartesian coordinate defining every point in the grid cell with its origin in the center and $\Delta x_i/2 \le h_i \le \Delta x_i/2 \quad (i=1,2,3)$ and Δx_i the dimension of the cell in each direction.

The integration of Eq. (II.15) leads to the cancelation of the even order terms and the equation becomes

$$\bar{\phi}_j = \phi_j + \sum_{l=1}^{3}\frac{\Delta x_l{}^3}{48}\left(\frac{\partial^2\phi}{\partial x_l{}^2}\right)_j + \mathrm{O}\left(\|\boldsymbol{h}\|^4\right) \qquad \text{(II.16)}$$

And thus from Eq. (II.16), the difference between the average value of the cell and the cell center value is of second order.

$$\bar{\phi}_j = \phi_j + \mathrm{O}\left(\|\boldsymbol{h}\|^2\right) \qquad \text{(II.17)}$$

Eq. (II.17) explains the order of accuracy to which the estimated values of the viscous term $\boldsymbol{F}^V{}_{i-1/2}$ at the interface between two grid cells are achieved.

In upacs-LES, the viscous stress is calculated by Eq. (II.18) as for a Newtonian fluid.

$$\tau_{lm} = 2\mu S_{lm} \tag{II.18}$$

S_{lm} is the viscous strain-rate and it is defined by Eq. (II.19).

The dummy variables l, m and n take the values of the vectors i, j, k defining the Cartesian base.

$$S_{lm} = \frac{1}{2}\left(\frac{\partial u_l}{\partial x_m} + \frac{\partial u_m}{\partial x_l}\right) - \frac{1}{3}\frac{\partial u_n}{\partial x_n}\delta_{lm} \tag{II.19}$$

For example, the flux in the i direction for the grid cell with center coordinates $[i, j, k]^T$ at the boundary of coordinates $[i+1/2, j, k]^T$ can be calculated as in Eq. (II.20).

$$2\mu\left(\left(\frac{\partial u}{\partial x}\right) - \frac{1}{3}\left(\frac{\partial u}{\partial x} + \frac{\partial v}{\partial y} + \frac{\partial w}{\partial z}\right)\right) + \tau_{ji} + \tau_{ki} \tag{II.20}$$

To calculate Eq. (II.20), it is necessary to estimate the gradient of each velocity components in each direction, this is done by simple central difference using the cell average velocities from the grid cells of coordinates $[i, j, k]^T$ and grid cell of coordinates $[i+1, j, k]^T$.

Eq. (II.21) is an example to estimate the derivative of the velocity u in the i direction using the value of the velocities at the cell centers $\overline{u}_{i+1}$ and $\overline{u}_i$ with Δx_i the distance between the two centers in the i direction.

$$\left(\frac{\partial u}{\partial x}\right)_{i+1/2} \equiv \frac{\overline{u}_{i+1} - \overline{u}_i}{\Delta x_i} \tag{II.21}$$

And similarly all the gradients are estimated following the same method shown here and named second order central difference.

2.3. Compact schemes

In Computational Aeroacoustics, there is a need to use numerical schemes leading to high accuracy results with low diffusion and dispersion errors and leading to good spectral resolution.

Several schemes satisfy these necessary requirements. Some of the widely used schemes by researches in this field are the high order compact schemes.

Kobayashi [24] formulated the high order compact schemes in finite volume method, and examined the stability, accuracy and spectral resolution of these methods.

Compact schemes are based on the Pade approximation of flux at the center of the boundary surfaces of the grid cell using the averaged values at the cell centers.

In this research, the implicit 6th order compact scheme is used for the calculation of the convective flux and only this case is explained hereafter, more details included in Appendix A, where the compact scheme is used to solve burgers equation.

For the implicit 6th order compact scheme, the interpolation of the value of a property ϕ at the interface of two grid cells with the index $i+1/2$ is done by the formula in Eq. (II.22).

In our research ϕ is any of the conservative variables in Eq. (II.2).

The average value at the adjacent grid cells in the line with j and k indexes fixed and i indexed as $i-1, i, i+1$ and $i+2$ are used to interpolate the values at the interface of the cells with indexes $i-1/2, i+1/2$ and $i+3/2$. The notation is shown in Figure II-2.

$$\alpha_{i6}\phi_{i-\frac{1}{2}} + \phi_{i+\frac{1}{2}} + \alpha_{i6}\phi_{i+\frac{3}{2}} = a_{ii6}\left(\overline{\phi}_i + \overline{\phi}_{i+1}\right) + b_{ii6}\left(\overline{\phi}_{i-1} + \overline{\phi}_{i+2}\right) \tag{II.22}$$

The Pade interpolation method consists at finding the coefficients α_{i6}, a_{ii6} and b_{ii6} by expanding the function ϕ with the Taylor series around the point of index $i+1/2$.

For the 6th-order compact scheme, this is achieved with the coefficients as in Eq. (II.23).

$$\alpha_{i6} = \frac{1}{3},\ a_{ii6} = \frac{29}{36},\ b_{ii6} = \frac{1}{36} \tag{II.23}$$

As the Taylors series expansion assumes uniform spacing grid, the coefficients in Eq. (II.23) can only be applied to uniform spacing grids.

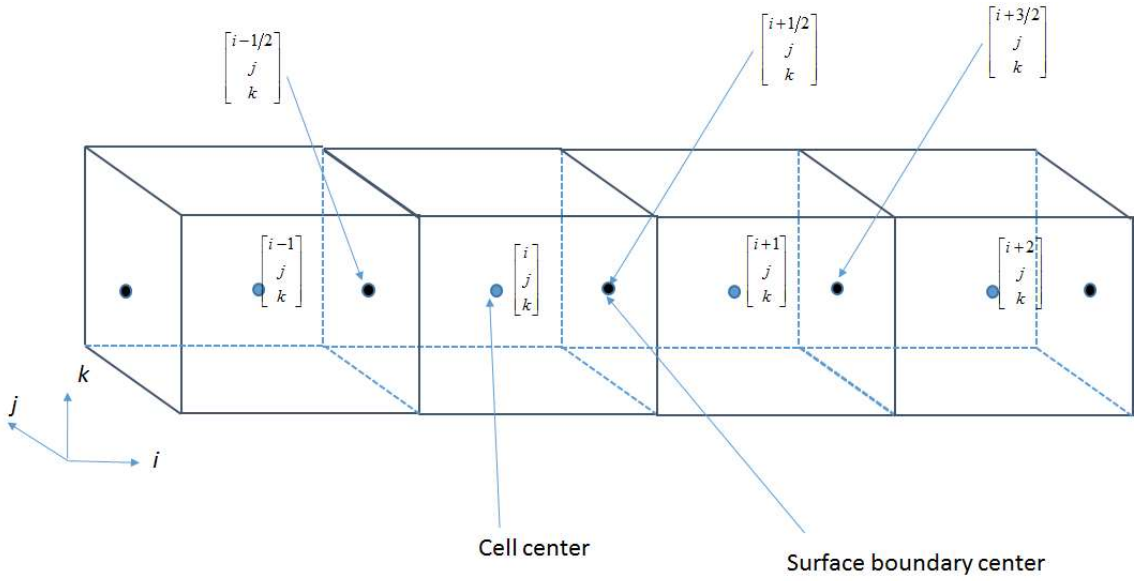

Figure II-2 Example of grid and notation for inner points

Also, a 6th-order explicit compact scheme is applied for the points near the left boundary, which is given by the expression in Eq. (II.24).

$$\phi_{-\frac{1}{2}} = a_{\mathrm{ib6}}\left(\bar{\phi}_{-1} + \bar{\phi}_{0}\right) + b_{\mathrm{ib6}}\left(\bar{\phi}_{-2} + \bar{\phi}_{1}\right) + c_{\mathrm{ib6}}\left(\bar{\phi}_{-3} + \bar{\phi}_{2}\right) \tag{II.24}$$

where the averaged values of the cells in Figure II-3 are used.

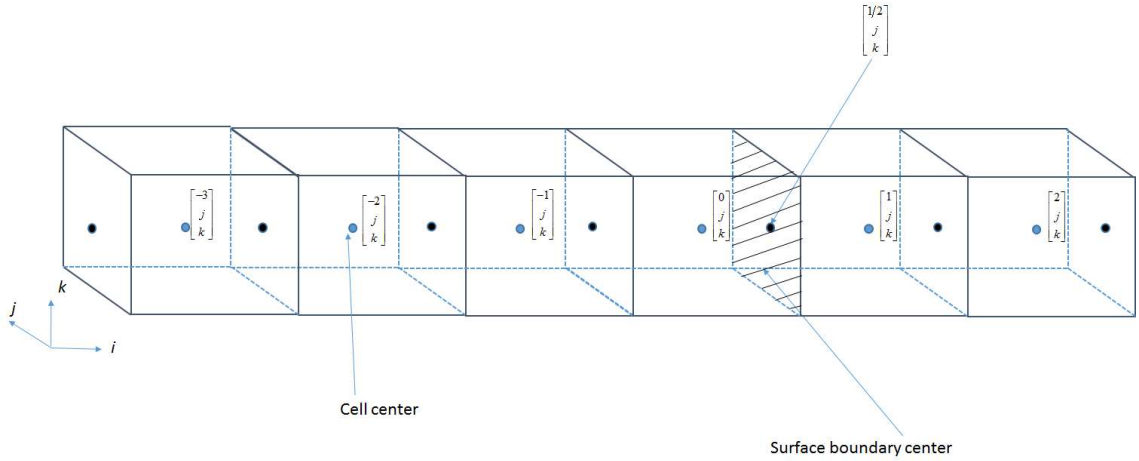

Figure II-3 Example of grid and notation for left boundary

For the right boundary also the 6th-order explicit compact scheme is applied, which is given by the expression in Eq. (II.25).

$$\phi_{N+\frac{1}{2}} = a_{\mathrm{ib6}}\left(\bar{\phi}_N + \bar{\phi}_{N+1}\right) + b_{\mathrm{ib6}}\left(\bar{\phi}_{N-1} + \bar{\phi}_{N+2}\right) + c_{\mathrm{ib6}}\left(\bar{\phi}_{N-2} + \bar{\phi}_{N+3}\right) \tag{II.25}$$

where the average values of the cells in Figure II-4 are used.

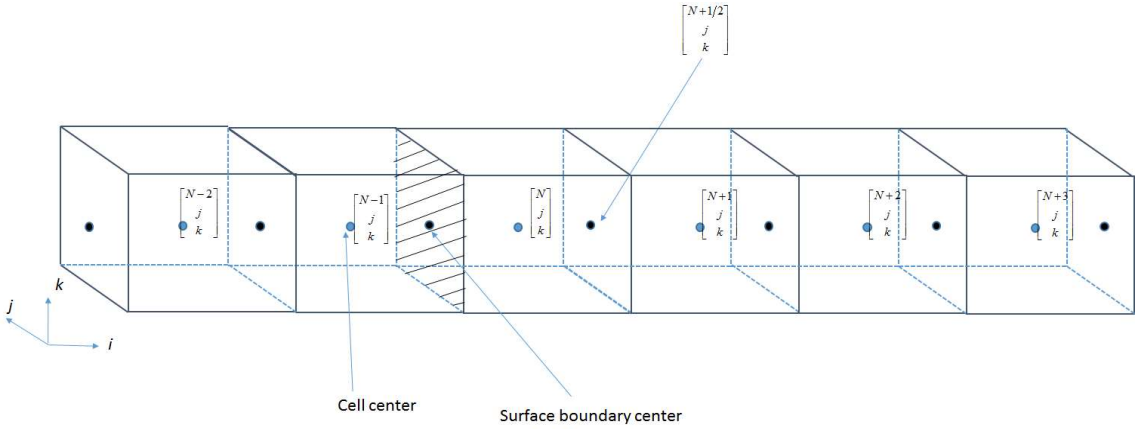

Figure II-4 Example of grid and notation for left boundary

High wavenumber numerical noise may be caused by the mesh non-uniformity as well as the discrete treatment of the boundary conditions. To suppress these unphysical cell-to-cell numerical oscillation, the low-pass filters in the form of Eq. (II.26) are used.

The compact filter is applied to the conservative variables in Eq. (II.2), where $\bar{\phi}$ and $\bar{\phi}^*$ are the unfiltered and filtered cell-center variables, respectively.

The coefficients α_f and a_{fj} are given for different orders of accuracy as shown in Table II-1.

$$\alpha_f \bar{\phi}^*_{i-1} + \bar{\phi}^*_i + \alpha_f \bar{\phi}^*_{i+1} = \sum_{j=0}^{N/2} a_{fj} \frac{\bar{\phi}_{i-j} + \bar{\phi}_{i+j}}{2} \tag{II.26}$$

In Eq. (II.26), N is the maximum order of the filter. However, in upacs-LES the order of the filter is gradually shifted from the maximum order inside the calculation domain to the 2nd order for the ghost cells near the boundary.

Table II-1 Coefficients of the compact Filter

order	a_{f0}	a_{f1}	a_{f2}	a_{f3}	a_{f4}	a_{f5}	a_f
10th	$\frac{193+126\alpha_f}{256}$	$\frac{105+302\alpha_f}{256}$	$\frac{-15+30\alpha_f}{64}$	$\frac{45-90\alpha_f}{512}$	$\frac{-5+10\alpha_f}{256}$	$\frac{1-2\alpha_f}{512}$	0.48
8th	$\frac{93+70\alpha_f}{128}$	$\frac{7+18\alpha_f}{16}$	$\frac{7\left(-1+2\alpha_f\right)}{32}$	$\frac{1-2\alpha_f}{16}$	$\frac{-1+2\alpha_f}{128}$		0.495
6th	$\frac{11+10\alpha_f}{16}$	$\frac{15+34\alpha_f}{32}$	$\frac{3\left(-1+2\alpha_f\right)}{16}$	$\frac{1-2\alpha_f}{32}$			0.4987
4th	$\frac{5+6\alpha_f}{8}$	$\frac{1+2\alpha_f}{2}$	$\frac{-1+2\alpha_f}{8}$				0.4997
2nd	$\frac{1+2\alpha_f}{2}$	$\frac{1+2\alpha_f}{2}$					0.49992

In this research, the 10th-order compact filter is the maximum order chosen. Therefore, in this case, the relationship between the boundary points and filter order is given by Figure II-5 and Figure II-6.

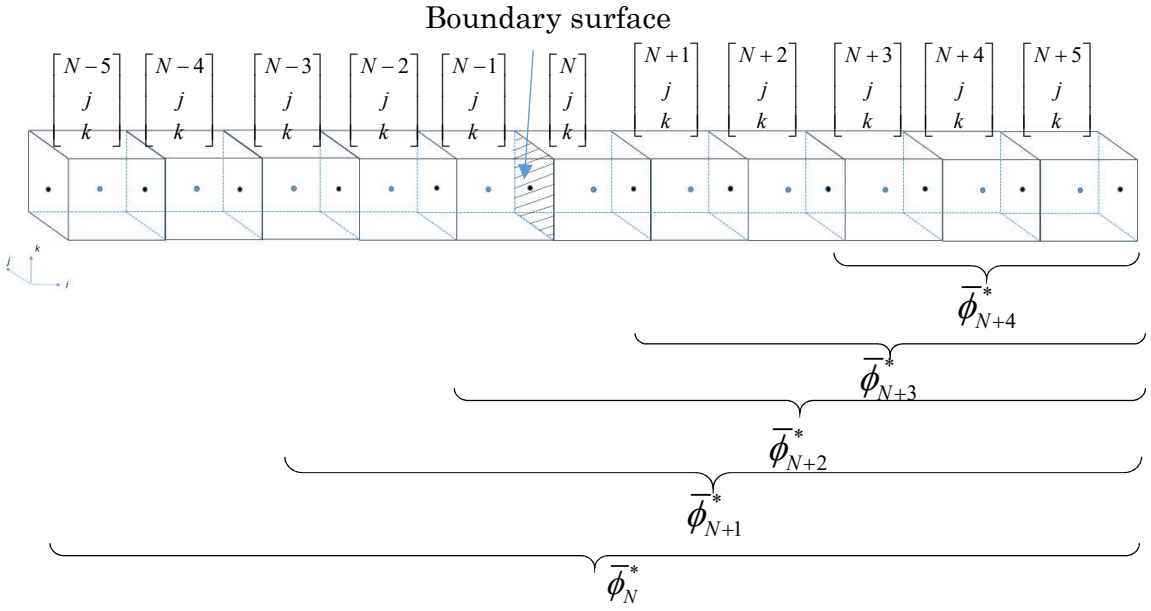

Figure II-5 Grid and notation for right boundary

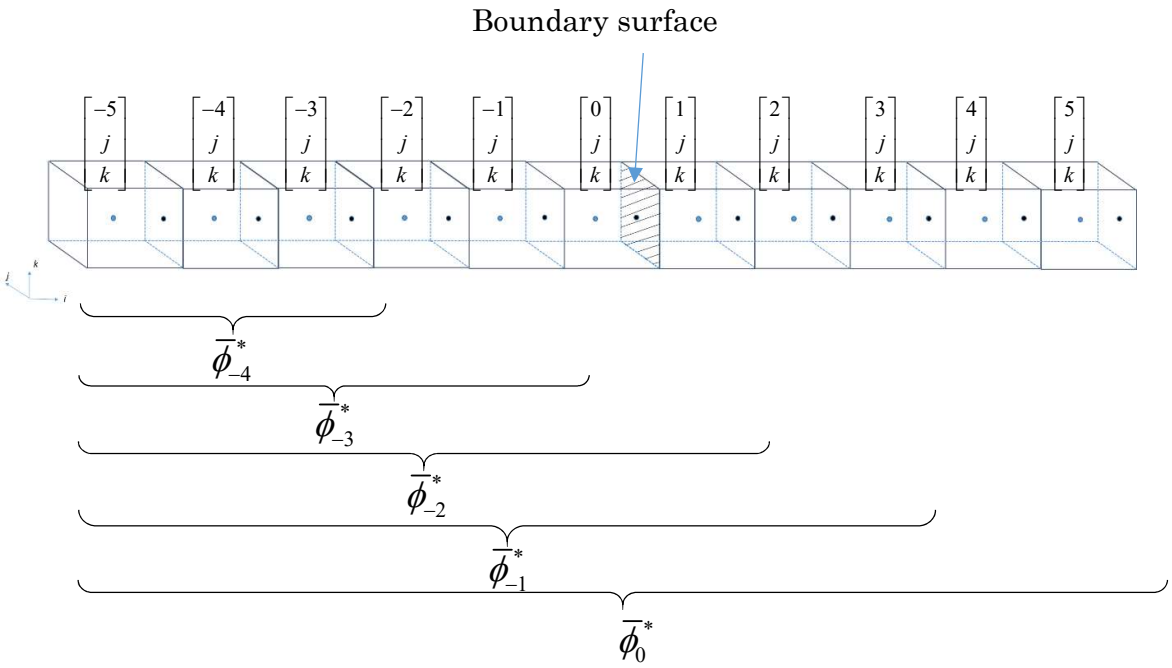

Figure II-6 Grid and notation for left boundary

2.4. Third-order Runge-Kutta time integration

The numerical simulations of turbulent flows with large eddy simulation require accurate and robust time-marching schemes. One of the prospective explicit time integration methods is given by the Runge-Kutta. These are high-order accuracy time integration methods by integration on different time stages. The Runge-Kutta methods are widely used in Computational Aeroacoustics.

The idea behind the Runge-Kutta method is to estimate the right-hand side in Eq. (II.14) on different stages using different value of conservative properties $\bar{\boldsymbol{Q}}$ in an interval of time between $n\Delta t$ and $(n+1)\Delta t$ and to use all these values to estimate the value of $\bar{\boldsymbol{Q}}$ at $(n+1)\Delta t$.

In upacs-LES the third-order Runge-Kutta method is implemented. Such that the flux of conserved variables in Eq. (II.14) are function of $\bar{\boldsymbol{Q}}$ as written in Eq. (II.27).

$$
\begin{aligned}
\bar{\boldsymbol{Q}}_1 &= \bar{\boldsymbol{Q}}^n \\
\bar{\boldsymbol{Q}}_2 &= \bar{\boldsymbol{Q}}^n + \alpha_1 \frac{\Delta t}{\Delta V} \boldsymbol{F}\left(\bar{\boldsymbol{Q}}_1\right) \\
\bar{\boldsymbol{Q}}_3 &= \bar{\boldsymbol{Q}}^n + \alpha_2 \frac{\Delta t}{\Delta V} \boldsymbol{F}\left(\bar{\boldsymbol{Q}}_2\right) \\
\bar{\boldsymbol{Q}}^{n+1} &= \bar{\boldsymbol{Q}}^n + \alpha_3 \frac{\Delta t}{\Delta V} \boldsymbol{F}\left(\bar{\boldsymbol{Q}}_3\right)
\end{aligned}
\qquad \text{(II.27)}
$$

with the coefficient specified as $\alpha_1 = 1/3$, $\alpha_2 = 1/2$ and $\alpha_3 = 1$

3. Large Eddy simulation

Large eddy simulation is a method to calculate turbulent flows with much more accuracy than RANS. The need to employ this method came from the fact that the more accurate Direct Numerical Simulation is too expensive since it resolves all the eddies with no embedded models for turbulence, making DNS beyond the capabilities of nowadays supercomputers for practical problems.

In RANS, on the other hand, it fails to develop a universal turbulence model that can be used to every situation, and this is mainly because large and small eddies are treated in same manner, but physically only the small eddies have an isotropic behavior and modeling these eddies would be a good idea, while the large eddies are anisotropic and dependent on the geometry of the domain simulated, thus turbulence models don't capture them accurately.

A better way of action would be to compute the large eddies directly for every problem while the small eddies can be modeled. This methodology constitute what is referred to as the Large Eddy Simulation.

3.1. Spatial Filtering in LES

In the conventional Large Eddy simulation method the properties are filtered in space into large eddies, and small scale eddies, using the filtering operation in Eq. (II.28). The influence of small eddies is then supplemented by the use of a sub-grid scale models.

$$\bar{\phi}(\vec{x},t) \equiv \iiint G(\vec{x},\vec{x}',\Delta)\phi(\vec{x}',t)\,dx'_1\,dx'_2\,dx'_3 \tag{II.28}$$

where $\vec{x}$ is the location of the filtered quantity in space and $\vec{x}'$ is a position vector. The function G is a low pass filter kernel that permits to eliminate the higher wavenumbers. The quantity to be filtered is denoted by ϕ while the filtered quantity is denoted by $\bar{\phi}$, where the overbar in this case representing the filtered quantities and not a mathematical averaging operation.

One of the examples of the function G is known as the Top-hat filter [25] and is given by Eq. (II.29) as it follows:

$$G(\vec{x},\vec{x}',\Delta) = \begin{cases} 1/\Delta^3 \rightarrow \left|x_i - x_i'\right| \le \Delta/2 \\ 0 \quad \rightarrow \left|x_i - x_i'\right| > \Delta/2 \end{cases} \tag{II.29}$$

Δ is the called the filter cutoff width, and it is a measure of the size of the eddies to be retained in the calculation. Since in a discretized domain only the data at one point per cell is kept,

there is no need to have a filter cutoff width smaller than the grid size, that's why in CFD, the cutoff width is of the same size as the grid size or equal to $\sqrt[3]{\Delta x \Delta y \Delta z}$ for a non-uniform three-dimensional grid.

Eq. (II.28) is reported in all theoretical textbooks and papers explaining large eddy simulation, and this is called explicit filtering however this is rarely implemented in the CFD algorithms. The reason for this is that when the conservation equations are solved using the finite volume method, the equations are integrated over control volumes. These integrated equations take the form of a convolution with a top-hat filter as shown previously in Eqs (II.10), (II.11) and (II.12).

3.2. Explicit and implicit sub-grid scale models

In the large eddy simulation, eddies that are smaller than the grid size cannot be resolved accurately, however their effect is of great importance and a key to accurate numerical simulations.

Sub-grid scale modeling accounts for the impact of these unresolved small scale eddies on the resolved Large eddies.

Hickel et al. [26] explains the basics of implicit large eddy simulation, and Grinstein et al. [27] dedicated a whole textbook to treat the problem in much more details.

By considering a nonlinear transport equation of a scalar ϕ with the following general equation, with $F(\phi)$ a nonlinear flux function of the variable ϕ.

$$\frac{d\phi}{dt} + \nabla . F(\phi) = 0 \tag{II.30}$$

The application of the spatial filtering operation shown in Eq. (II.28) to the generic nonlinear transport in Eq. (II.28), the filtered form can be written as in Eq. (II.31).

$$\frac{d\bar{\phi}}{dt} + G * \left(\nabla . F(\phi)\right) = 0 \tag{II.31}$$

We note the discretized function $\bar{\phi}_N$, which is used in the numerical simulation and it represents the filtered function projected over the grid points $x_N = \{x_j\}$

Such that

$$\bar{\phi}_N = \left\{\bar{\phi}(x_j)\right\}, j \in \mathbb{Z} \tag{II.32}$$

Eq. (II.31) can be rewritten in a discretized form as in Eq. (II.33).

$$\frac{\partial \bar{\phi}_N}{\partial t} + G * \left(\nabla . F_N(\phi_N)\right) = -G * \left(\nabla . \varsigma_{SGS}\right) \tag{II.33}$$

where ς_{SGS} is equal to the error introduced by the discretization and it is equal to the difference between the continuous and discrete flux

$$\varsigma_{SGS} = F(\phi) - F_N(\phi_N) \tag{II.34}$$

In the explicit SGS models try to give an approximation to the right-hand side of Eq. (II.33) such as Smagorinsky [28] or Vreman [29] eddy viscosity models.

However since the explicit sub-grid scale models are just approximations, a modeling error ς_M is introduced to the Eq. (II.33) such that this error is equal to the difference in Eq. (II.35). M_{SGS} is the explicit sub-grid scale model.

$$\varsigma_M = G*(\nabla.\varsigma_{SGS}) - G*(\nabla.M_{SGS}) \tag{II.35}$$

When these equations are implemented for computer calculations, an extra error called truncation error appears. It is the result of numerical approximations to the analytical functions and mathematical operations of the numerical schemes. These approximations are indicated with an upper arc in Eq. (II.36).

$$\varsigma_N = G*(\nabla.F_N(\phi_N)) - \breve{G}*\left(\breve{\nabla}.\breve{F}_N\left(\breve{\phi}_N\right)\right) + G*(\nabla.M_{SGS}) - \breve{G}*\left(\breve{\nabla}.\breve{M}_{SGS}\right) \tag{II.36}$$

Finally, we end up with a modified differential equation of the form

$$\frac{\partial \bar{\phi}_N}{\partial t} + G*(\nabla.F_N(\phi_N)) = \varsigma_N + \varsigma_M - G*(\nabla.\varsigma_{SGS}) \tag{II.37}$$

In this research, we use what is called an implicit large eddy simulation (ILES) method, contrary to the conventional LES where an explicit sub-grid scale model M_{SGS} is added. In ILES the numerical scheme errors and the sub-grid scale model are coupled.

If the truncation error approximates the sub-grid scale stress, then it would be equivalent to an implicit sub-grid scale model.

$$\varsigma_N \approx -G*(\nabla.\varsigma_{SGS}) \tag{II.38}$$

3.3. Filtered Navier Stokes equations in upacs-LES

In upacs-LES the governing equations are based on the formulation given by Vreman et al [29] and implemented by Enomoto et al [30].

The Favre average operation of a physical property is used such that $\overline{\rho\phi} = \bar{\rho}\tilde{\phi}$.

Where $\tilde{\phi} = \dfrac{\overline{\rho\phi}}{\bar{\rho}}$ is a mass-weighted filtered physical property like velocity and temperature…

This operation is only a change of variable and doesn't inherit the properties of the filtering operation with the convolution operator.

From the application of the filtering operator in Eq. (II.28) to the governing equations of fluid flow in Eq. (II.1) we get the filtered continuity equation.

$$\frac{\partial \bar{\rho}}{\partial t} + \frac{\partial \bar{\rho}\tilde{u}_i}{\partial x_i} = 0 \tag{II.39}$$

Repeating the process to momentum equations in Eq. (II.1).

$$\frac{\partial \bar{\rho}\tilde{u}_i}{\partial t} + \frac{\partial \bar{\rho}\tilde{u}_i\tilde{u}_j}{\partial x_j} + \frac{\partial \bar{p}}{\partial x_i} - \frac{\partial\left(\sigma_{ij} + \hat{\tau}_{ij}\right)}{\partial x_j} = 0 \tag{II.40}$$

Eq. (II.40) have the same form as the Navier Stokes equations. However, for solving the filtered velocity field an extra term appears due to the filtering operation and it is called the sub-grid scale stress $\sigma_{ij} = -\bar{\rho}\left(\widetilde{u_i u_j} - \tilde{u}_i\tilde{u}_j\right)$.

The viscous stress tensor included in Eq. (II.40) is calculated using the filtered properties. The hat symbol $\hat{\cdot}$ is used to refer to quantities calculated with filtered properties.

$$\hat{\tau}_{ij} = 2\tilde{\mu}\left(\tilde{S}_{ij} - \frac{1}{3}\tilde{S}_{kk}\delta_{ij}\right) \tag{II.41}$$

With the strain tensor calculated as $\tilde{S}_{ij} = \frac{1}{2}\left(\frac{\partial \tilde{u}_i}{\partial x_j} + \frac{\partial \tilde{u}_j}{\partial x_i}\right)$ and a viscosity function of the temperature $\tilde{\mu} \equiv \mu\left(\tilde{T}\right)$ with the use of Sutherland's law.

σ_{ij} is the sub-grid scale stress approximated with same form as the viscous stress tensor, except that instead of the molecular viscosity, eddy viscosity is used.

$$\sigma_{ij} = -\bar{\rho}\left(\widetilde{u_i u_j} - \tilde{u}_i\tilde{u}_j\right) = 2\bar{\rho}\nu_t\left(\tilde{S}_{ij} - \frac{1}{3}\tilde{S}_{kk}\delta_{ij}\right) \tag{II.42}$$

The filtered energy equation is obtained by application of the filtering operator to Eq. (II.1). The total energy $\widehat{\rho E}$ is also calculated with filtered variable as $\widehat{\rho E} = \frac{\bar{p}}{\gamma - 1} + \frac{1}{2}\bar{\rho}\tilde{u}_i\tilde{u}_i$

$$\frac{\partial \widehat{\rho E}}{\partial t} + \frac{\partial\left(\widehat{\rho E} + \bar{p}\right)\tilde{u}_j}{\partial x_j} - \frac{\partial}{\partial x_j}\left(\left(\hat{\sigma}_{ij} + \tau_{ij}\right)\tilde{u}_i\right) + \frac{\partial\left(\hat{q}_j + Q_j\right)}{\partial x_j} = 0 \tag{II.43}$$

$\hat{q}_j$ is the heat flux vector calculated as a function of the filtered variables with Eq. (II.44).

$$\hat{q}_j = -\frac{C_p\tilde{\mu}}{P_r}\frac{\partial \tilde{T}}{\partial x_j} \tag{II.44}$$

And the effect of the dissipation by sub-grid scale on the large eddies is included as in Eq. (II.45). It is a function of the eddy viscosity ν_t.

$$\frac{\partial Q_j}{\partial x_j} = \frac{\partial}{\partial x_j}\left(-\frac{C_p\bar{\rho}\nu_t}{P_{rt}}\frac{\partial \tilde{T}}{\partial x_j}\right) \tag{II.45}$$

Since the governing equation are for the compressible case, the closer is achieved using the filtered equation of state.

$$\bar{p} = \bar{\rho}R\tilde{T} \tag{II.46}$$

Many sub-grid scale models are implemented in upacs-LES. Three of these models (Smagorinsky model,Vreman Model, and MILES) are introduced hereinafter.

Smagorinsky model

Smagorinsky et al. [28], developed a sub-grid scale model named after his name. In this model Smagorinsky generalized the turbulence viscosity introduced by Boussinesq to the large eddy simulation.

In the Smagorinsky model, the effect of the small scale eddies on the large resolved eddies is model with an eddy viscosity of the form of Eq. (II.47).

$$\nu_t = \left(C_s \Delta\right)^2 \left|\tilde{S}\right| \tag{II.47}$$

$\tilde{S}_{ij}$ is the strain tensor and $\left|\tilde{S}\right| = \left(\tilde{S}_{ij}\tilde{S}_{ij}\right)^{\frac{1}{2}}$ is its magnitude.

To complete the closure the Smagorinsky constant C_s needs to be specified, and its value is known to vary with applications. In the literature we can find different used value, for example, Deardoff [31] recommends a value of $C_s = 0.1$ for a turbulent channel flow, even though the theoretical calculated coefficient is equal to $C_s = 0.18$. This value may be reduced in order to reduce the excessive dissipation of this model.

Vreman model

Vreman [29] proposed a sub-grid scale model which corrects some of the drawback of the Smagorinsky model. The sub-grid dissipation vanishes for laminar shear flow near the wall boundaries due to the flow function B_β.

The proposed eddy viscosity is of the form

$$\nu_t = V_c \sqrt{\frac{B_\beta}{\gamma_{ij}\gamma_{ij}}} \tag{II.48}$$

with $B_\beta = \beta_{11}\beta_{22} - \beta_{12}^2 + \beta_{11}\beta_{33} - \beta_{13}^2 + \beta_{22}\beta_{33} - \beta_{23}^2$, the second invariant of the tensor, and $\gamma_{ij} = \frac{\partial \tilde{u}_j}{\partial x_i}$ are the first-order derivatives of the filtered velocity field.

The constant V_c is related to the constant of Smagorinsky C_s by the relation $V_c = 2.5C_s^2$, and this value is often equal to $V_c = 0.025$ for turbulent flows.

MILES

The Monotonic Integrated Large Eddy Simulation (MILES) is a large eddy simulation approach. In MILES the implicit sub-grid scale models are built such that the discretization errors are coupled to the resolvable scales as shown in Eq. (II.38) where the truncation errors approximates the sub grid scale stress.

In upacs-LES, this is simply obtained by having zero turbulence viscosity

$$\nu_t = 0$$

4. Implementation of the sources

This research simulates numerically using CFD conditions similar to the ones encountered in an impedance tube experiment [21]. The generation of the sound wave in the experiment using a loud speaker is simulated.

4.1. Sound source model used in section V.1.

The sound source used in this research is implemented in a specified region of the calculation domain. This is realized by the addition of the source term $\boldsymbol{S}$ in Eq. (II.5) to the flux term in Eq. (II.14) throughout time integration procedure.

In the case of the sound source, the source term vector becomes

$$\boldsymbol{S} = [S_1, S_2, 0, 0, S_5]^{\mathrm{T}} \tag{II.49}$$

The first term S_1 in Eq. (II.49) denotes the oscillations in the mass caused by the desired sound wave. S_1 is given by Eq. (II.50) as follows:

$$S_1 = \frac{\rho A u_{ac}(t)}{V_{ss}} \tag{II.50}$$

where V_{ss} is the volume of the sound source region and u_{ac} is the acoustic particle velocity changing sinusoidally in time as given in Eq. (II.51).

$$u_{ac}(t) = u_a \sin(\omega t) \tag{II.51}$$

Here ω denotes the angular frequency and u_a denotes the amplitude of the acoustic particle velocity that leads to the amplitude of the specified acoustic pressure wave p_a.

The amplitude of the acoustic particle velocity is calculated as $u_a = p_a / Z_0$, where $Z_0 = \rho c$ denotes the characteristic impedance of the air.

The second term S_2 in Eq. (II.49) denotes the oscillations in the momentum caused by the desired sound source. S_2 is given by Eq.(II.52) as follows:

$$S_2 = S_1 \times u_{ac}(t) \tag{II.52}$$

The fifth term S_5 in Eq. (II.49) denotes the relationship of the internal energy and the desired sound wave pressure amplitude. S_5 is given by Eq. (II.53) as follows:

$$S_5 = S_1\left(C_v T_0 + \frac{1}{2}(u_{ac}(t))^2\right) \tag{II.53}$$

where

C_v : Specific heat at constant volume

T_0 : Temperature

In order to avoid any undesired oscillations caused by the introduction of the sound source, a time ramping function is introduced.

$$f(t) = \min\left(1.0, \left(\frac{t}{t_0}\right)^3\right) \tag{II.54}$$

The function defined in Eq. (II.54) is then multiplied into the terms in Eq. (II.49) to give

$$S_{t_0} = f(t) \times S \tag{II.55}$$

By doing so, the sound source is introduced gradually until the time t of the solution reaches a certain chosen ramping time t_0.

The desired sound amplitude pressure p_a in Pascal is calculated from the sound pressure level SPL of the sound wave using Eq. (II.56).

$$p_a = p_{ref} 10^{\left(\frac{SPL}{20}\right)} \tag{II.56}$$

where p_{ref} is an international reference sound pressure considered as the threshold of human hearing [32] and it is equal to

$$p_{ref} = 2 \times 10^{-5}\,[\text{Pa}] \tag{II.57}$$

4.2. Sound source model used in section V.2.

The sound source used in this research is implemented in a specified region of the calculation domain. This is realized by the addition of the source term $\boldsymbol{S}$ in Eq. (II.5) to the flux term in Eq. (II.14) throughout time integration procedure.

The sound source is implemented in the solver as an energy source that changes sinusoidally in time as shown in Eq. (II.58) as follows:

$$S_5 = e_i \sin(\omega t) = \frac{p_a}{\gamma - 1} \sin(\omega t) \tag{II.58}$$

Here ω denotes the angular frequency and e_i denotes the amplitude of the internal energy that leads to the amplitude of the specified acoustic pressure wave p_a.In Eq. (II.58) γ is the specific heat ratio

4.3. Mass source

In order to add a bias flow exiting the cavity of the resonator in the direction of the acoustic tube and at the same time to simulate the reflection of the sound wave from the back wall of the cavity, a mass source is implemented to the solver code in the region near the back plate.

To realize this, we add a source term to the Navier-Stokes equations.

In order to successfully generate a bias flow through the aperture, in addition to defining the mass source, it is necessary to add momentum and energy source terms in addition to the mass.

In our situation, we add a mass source S_1 , the momentum source in the i direction S_2 and energy source S_5 .

The source term vector becomes as follows:

$$\boldsymbol{S} = \left[S_1, S_2, 0, 0, S_5\right]^{\mathrm{T}} \tag{II.59}$$

The following quantities are needed for the formulation of the source:

ρ : Density

u_{jet} : Velocity at the aperture

A_{jet} : Aperture area

V_{total} : Volume of the mass source region

Then the mass source S_1 can be calculated as

$$S_1 = \frac{\dot{m}_{\text{total}}}{V_{\text{total}}} \tag{II.60}$$

where $\dot{m}_{\text{total}}$ is the required mass flow at the aperture and it is calculated by Eq. (II.61).

$$\dot{m}_{\text{total}} = \rho u_{\text{jet}} A_{\text{jet}} \left[\text{kg/s}\right] \tag{II.61}$$

And the momentum source in the i direction S_2 is defined by Eq. (II.62).

$$S_2 = \frac{\dot{m}_{\text{total}} u_{\text{jet}}}{V_{\text{total}}} \tag{II.62}$$

And the energy source S_5 is calculated as the sum of internal energy of the added mass plus its kinetic energy given by Eq. (II.63).

$$S_5 = \dot{m}_{\text{total}} \left(C_v T_0 + \frac{1}{2}\left(u_{\text{jet}}\right)^2 \right) \frac{1}{V_{\text{total}}} \tag{II.63}$$

In this chapter, the general calculation procedure to Computational Fluid Dynamics is discussed. The derivation of the governing equations of fluid dynamics, and the numerical schemes used in this research are explained. A basic introduction to large eddy simulation method is given. At last the implementation method of the sound source, as well as the mass source in the CFD code, is presented.

In the next chapter, we explain the post-processing tools used in this research. First, the two-microphone method used to estimate the absorption coefficient is presented, then a different method to estimate the absorption coefficient based on viscous dissipation is introduced.

Chapter 3

III. Post-Processing Methods

One of the important steps when dealing with Computational Fluid Dynamics is the post-processing of the results obtained by the calculation. In this research, in addition to the conventional commercial tools to get fluid flow contours, the methods to calculate acoustic properties such as the absorption coefficient are used.

1. Transfer Function Method

The transfer function method [33] is a procedure to measure acoustic impedance. In this study, this method is used in both the experiments as well as the numerical simulations. This method is also called the two microphone method. The two microphone method gives accurate acoustic properties over a wide frequency range by using broadband excitation such as white noise. Moreover performing the transfer function method in the experiment is very fast compared to the standing wave method. Also in CFD, the benefit of the two microphone method over the standing wave method is that the impedance tube can be shorter which reduces the calculation time. In this section, the derivation of the transfer function method to obtain to necessary acoustic properties is given.

To be accurate, the normal impedance tube deals with plane waves traveling in the duct. Such an assumption is only valid for sound waves for which wavelengths are longer than the tube diameter. The standard ISO 10534-2:1998[34] specifies the applicable frequency range as follows:

$$f_l < f < f_u \tag{III.1}$$

Here, f_l is the lower limit frequency, which is stipulated by the accuracy of signal processing. f_u is the upper limit frequency beyond which non plane wave modes exist inside the tube. f is the excitation frequency from the sound source.

The upper-frequency limit f_u in the case of a circular pipe is obtained as follows:

$$f_u = 0.58\frac{c}{d} \tag{III.2}$$

where d is the inner diameter and c is the speed of sound.

The upper-frequency limit f_u is also limited by the distance s between the two microphones used in order to ensure a certain phase difference. The standard ISO 10534-2:1998[34] requires around a half wave length difference:

$$f_u = 0.45\frac{c}{s} \tag{III.3}$$

The lower limit frequency depends on the microphone spacing and the accuracy of the analysis system. As a general guideline, when the microphone spacing is increased, the measurement accuracy is improved.

The microphone spacing needs to exceed 5% of the wavelength of the measurement lower limit frequency as follows:

$$f_l = 0.05\frac{c}{s} \tag{III.4}$$

Figure III-1 shows a normal incidence acoustic impedance tube setup using two microphones. The sound pressure at the location of microphone 1 is the sum of the incident pressure acoustic wave $p_I(x_1) = \hat{p}_I e^{jkx_1}$ at location of microphone 1 and the reflected acoustic wave $p_R(x_1) = \hat{p}_R e^{-jkx_1}$ at the same location.

$$p_1 = p_I(x_1) + p_R(x_1) \tag{III.5}$$

while the sound pressure at the location of microphone 2 is the sum of the incident acoustic wave $p_I(x_2) = \hat{p}_I e^{jkx_2}$ and the reflected acoustic waves $p_R(x_2) = \hat{p}_R e^{-jkx_2}$. Here $\hat{p}_I$ and $\hat{p}_R$ are the complex amplitudes at the surface of the tested sample where $x = 0$;

$$p_2 = p_I(x_2) + p_R(x_2) \tag{III.6}$$

H_{12} is the transfer function of the resulting standing sound wave, and it is calculated as the ratio of the pressure at location 2 and pressure at location 1.

$$H_{12} = \frac{p_2}{p_1} \tag{III.7}$$

Substituting Eqs. (III.5) and (III.6) into Eq. (III.7) and dividing both the numerator and the denominator by $\hat{p}_I$ we get

$$H_{12} = \frac{e^{jkx_2} + Re^{-jkx_2}}{e^{jkx_1} + Re^{-jkx_1}} \tag{III.8}$$

where we define the reflection coefficient as $R = \hat{p}_R/\hat{p}_I$.

By solving Eq. (III.8) for the reflection coefficient R we get Eq. (III.9).

$$R = \frac{H_{12}e^{jkx_1} - e^{jkx_2}}{e^{-jkx_2} - H_{12}e^{-jkx_1}} \tag{III.9}$$

By dividing the numerator by e^{jkx_1} and the denominator by e^{-jkx_1} of Eq. (III.9) and defining the distance between the two microphones as s = $x_1 - x_2$ we get Eq. (III.10) as follows:

$$R = \frac{H_{12} - e^{-jks}}{e^{jks} - H_{12}} e^{2jkx_1} \tag{III.10}$$

We define the transfer function of the incident wave as the ratio of the pressure of the incident acoustic wave at the location of microphone 2 to the location of microphone 1, and it is given by Eq. (III.11).

$$H_I = \frac{p_I(x_2)}{p_I(x_1)} = \frac{\hat{p}_I e^{jkx_2}}{\hat{p}_I e^{jkx_1}} = e^{jk(x_2 - x_1)} = e^{-jks} \tag{III.11}$$

In the same manner, the transfer function of the reflected wave is defined as the ratio of the pressure of the reflected acoustic wave at the location of microphone 2 to the location of microphone 1, and it is given by Eq. (III.12).

$$H_R = \frac{p_R(x_2)}{p_R(x_1)} = \frac{\hat{p}_R e^{-jkx_2}}{\hat{p}_R e^{-jkx_1}} = e^{jks} \tag{III.12}$$

By replacing Eqs. (III.11) and (III.12) into Eq. (III.10) we get the following equation which determines the reflection coefficient at the surface of the sample we desire to measure.

$$R = \frac{H_{12} - H_I}{H_R - H_{12}} e^{2jkx_1} \tag{III.13}$$

It is to be noted that the reflection coefficient at the location $\boldsymbol{x_1}$ of the microphone 1 is given by Eq. (III.14).

$$R_{\boldsymbol{x_1}} = \frac{H_{12} - H_I}{H_R - H_{12}} \tag{III.14}$$

The surface impedance of the liner is obtained by using the reflection coefficient as given in Eq. (III.15) as it follows:

$$\frac{Z}{Z_0} = \frac{1 + \mathrm{R}}{1 - \mathrm{R}} \tag{III.15}$$

with $Z_0 = \rho c$ is the characteristic acoustic impedance of air.

On the other hand, the absorption coefficient α of the liner is expressed as the ratio of sound intensity absorbed I_{abs} and the incident sound intensity I_{inc}.

$$\alpha = \frac{I_{abs}}{I_{inc}} \tag{III.16}$$

The sound intensity is defined as the sound power per unit area. It can be calculated as the multiplication of sound pressure p and acoustic particle velocity v.

$$I = pv = \frac{p^2}{Z_0} \tag{III.17}$$

By writing the absorbed intensity I_{abs} as the difference between the incident intensity I_{inc} and reflected intensity I_{ref}, Eq. (III.16) becomes

$$\alpha = \frac{I_{inc} - I_{ref}}{I_{inc}} = 1 - \frac{I_{ref}}{I_{inc}} \tag{III.18}$$

By substituting Eq. (III.17) in Eq. (III.18), the absorption coefficient can be written as a function of the reflection coefficient as it follows:

$$\alpha = 1 - R^2 \tag{III.19}$$

The method described in this section is implemented in the commercial numerical computing environment MATLAB. This software allows to perform matrix manipulations, function plotting, and algorithm implementation.

The discrete data obtained by the microphones in the acoustic impedance tube in both the experiments as well as the CFD calculations in this research are in the time domain. Consequently, the use of the fast Fourier transform procedure in MATLAB is necessary in order to obtain the discrete Fourier transform. The implementation code using Matlab is given in the Appendix C.

Details on the use of the fast Fourier transform can be found in the textbook by Steven T. Karris [1]. As a result, we can write the pressure waves and the transfer functions in the complex frequency domain as defined in this section.

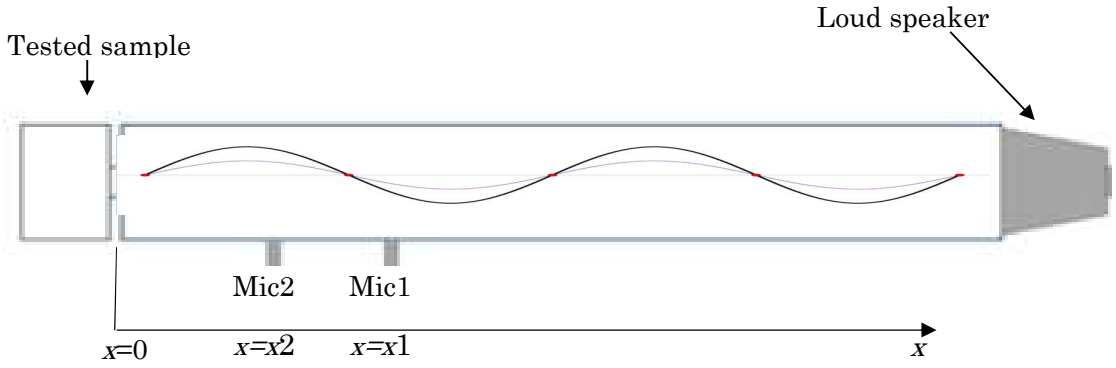

Figure III-1 Sound impedance tube with Transfer Function Method

2. Viscous dissipation method

Different from the previous method based on the pressure signals saved by the two microphones in CFD, in this method the calculation of the absorption coefficient is based on the evaluation of the viscous dissipation rate in CFD.

The absorption coefficient in this evaluation is determined as the ratio of the absorbed acoustic power carried by the wave passing through the aperture to the total acoustic power traveling in the impedance acoustic tube.

Viscous effects cause the absorption of acoustic waves in perforated plates (Tam et al. [25] and Zhang et al. [12]). Thus, it is important to calculate the energy rate at which acoustic energy is converted to viscous dissipation as given in Eq. (III.20).

$$E^{\mathrm{v}}_{\mathrm{viscous}} = \iiint_V \bar{D}(x,y,z)\,dxdydz \tag{III.20}$$

Eq. (III.20) is the integration of the time-averaged dissipation rate $\bar{D}(x,y,z)$ given in Eq. (III.21) over the volume V. This volume is assumed to be large enough to include the dissipation caused by the shed vortices as shown in Figure III-2.

$$\bar{D}(x,y,z) = \frac{1}{T}\int_0^T \Phi\, dt \tag{III.21}$$

In Eq. (III.22), Φ is called the viscous dissipation function, and it denotes the rate of conversion of the viscous force work to internal energy. The viscous dissipation function is expressed for a Newtonian fluid as specified by Greitzer et al. [26].

$$\begin{aligned}\Phi = \tau_{ij}\frac{\partial u_i}{\partial x_j} = \underbrace{2\mu\left[\left(\frac{\partial u}{\partial x}\right)^2 + \left(\frac{\partial v}{\partial y}\right)^2 + \left(\frac{\partial w}{\partial z}\right)^2\right]}_{\Phi_1} \\ \underbrace{+2\mu\left[-\frac{1}{3}\left(\frac{\partial u}{\partial x}+\frac{\partial v}{\partial y}+\frac{\partial w}{\partial z}\right)^2\right]}_{\Phi_2} \\ \underbrace{+\mu\left[\left[\frac{\partial v}{\partial x}+\frac{\partial u}{\partial y}\right]^2 + \left[\frac{\partial w}{\partial y}+\frac{\partial v}{\partial z}\right]^2 + \left[\frac{\partial u}{\partial z}+\frac{\partial w}{\partial x}\right]^2\right]}_{\Phi_3}\end{aligned} \tag{III.22}$$

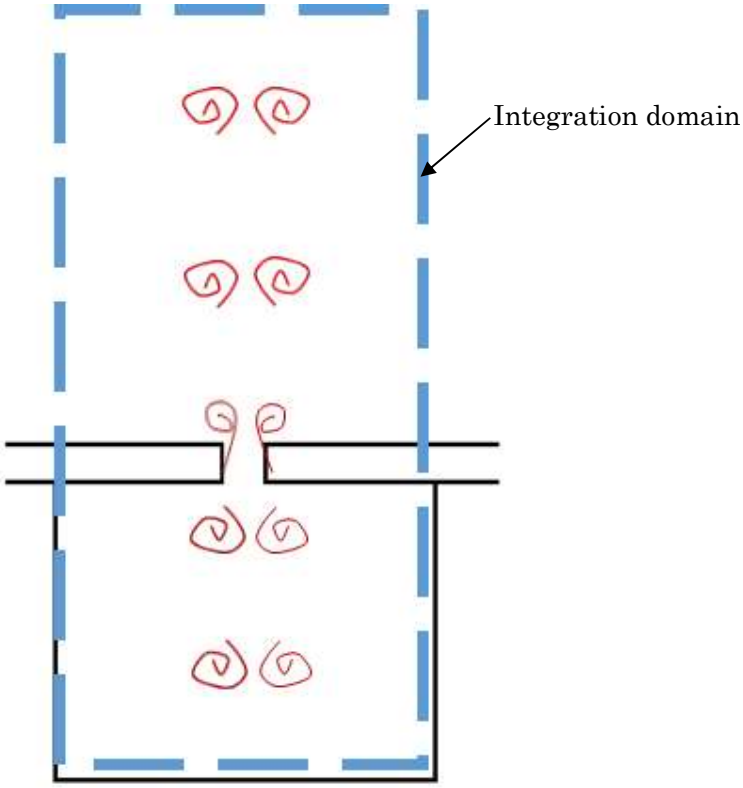

Figure III-2 Integration domain

The viscosity of air μ is calculated via Sutherland's law. Eq. (III.22) corresponds to the sum of three terms. Φ_1 denotes the dissipation caused by the normal deformation of the fluid element. Φ_2 is the dissipation caused by the dilatation of the fluid element. And finally, Φ_3 accounts for the dissipation caused by angular deformation when the considered fluid element undergoes shear deformation.

The acoustic intensity of the incident sound wave is defined as $\overline{p_I^2}/\rho_0 a_0$ where p_I is the incident sound pressure. Thus the acoustic power through the aperture can be written as in Eq. (III.23), where A_s is the aperture area.

$$E^s_{incident} = \frac{\overline{p_I^2} A_s}{\rho_0 a_0} \tag{III.23}$$

And the acoustic power through the impedance acoustic tube can be written as in Eq. (III.24), where A_t is the tubes area.

$$E^t_{incident} = \frac{\overline{p_I^2} A_t}{\rho_0 a_0} \tag{III.24}$$

The term $\left(E^v_{viscous} / E^s_{incident}\right) \times \left(\overline{p_i^2} / \rho_\infty a_\infty\right) A_s$ denotes the rate at which acoustic energy is absorbed by the acoustic liner as a results of viscous dissipation.

Finally, the absorption coefficient can be calculated by Eq. (III.25).

$$\alpha = \frac{\left(E^V_{viscous} / E^s_{incident}\right) \times \left(\overline{p_I^2} / \rho_0 a_0\right) A_s}{\left(\overline{p_I^2} / \rho_0 a_0\right) A_t} = \frac{E^V_{viscous}}{E^s_{incident}} \times \frac{A_s}{A_t} \tag{III.25}$$

3. Tecplot

A commercial software called Tecplot 360 EX 2015 was used to visualize and analyze the flow field and to calculate common fluid properties such as vorticity, velocity, pressure,.., from the conserved variables (density, momentum, and energy) obtained as a results of the numerical calculation using upacs-LES.

With Tecplot, it is possible to draw contours, vectors, and streamlines colored with different fluid properties, and to perform animations for unsteady calculations.

As it is not possible to calculate the viscous dissipation rate described in section III.2 using the Calculate Variables tool in Tecplot, the Tecplot macro function provided in the software was used.

Macro commands are a set of instructions which enable to perform multiple actions in Tecplot. The instructions are written in a similar way as language programming. This also permits to perform actions such as looping and conditional commands. More details are in the scripting guide of Tecplot 360[35].

Chapter 4

IV. Impedance tube Experiment

In order to obtain the acoustic properties of the resonators considered in this study, the acoustic impedance tube experiment is first conducted for validation purposes of the numerical simulations conducted in Chapter V as well as the validation of the theoretical models in Chapter VI.

First, the experimental rig is described, then the acoustic resonators used in the experiment and their dimensions are given. Finally, the absorption coefficient results and the impedance of each resonator are shown.

1. Experimental configuration

In this section, the experimental configuration used in this experiment is described. The impedance tube experimental rig is shown in Figure IV-1 and the schematic representation of the experimental rig is given in Figure IV-2.

All experiments conducted in this study are based on the two-microphone method described in Chapter III.

A tube made of plastic is used as a duct for the sound waves. The internal diameter of the tube is 100 mm and it has a length of 2 m.

A full-range speaker (FF85WK, FOSTEX) shown in Figure IV-4 has a frequency range up to 28 kHz and a resonance frequency about 115 Hz. Because of this resonance frequency, the results for frequencies lower than 200Hz are ignored in our experiments. The loudspeaker is attached at one end of the tube to generate sound waves. At the other end of the tube, the resonator specimen under test is attached. The cavity of the resonator has a depth of 52 mm and it has an internal diameter of 100 mm. The diameter makes it possible to examine low-frequency acoustic resonators since it exhibits a cut-off frequency of approximately 2000 Hz. Two different perforated plates made of aluminum with a thickness of 3 mm with different aperture geometry are installed between the cavity and tube sections. Such thick plates are selected to stiffen the plates to reduce the absorption caused by the vibration of the plates.

In order to produce a bias flow through the perforated plate, two air supply holes are created on the cavity side wall and are connected to compressed air by using flexible pipes. A mass flow controller (KOFLOC 8550) is used to regulate the desired flow rate. The complete configuration in the case of bias flow resonator is as shown in Figure IV-6.

The flow outlet is made by 30 mm × 1.0 mm slit in the flange where the loudspeaker is attached as shown in Figure IV-3.

The white noise is generated by the computer and fed to an amplifier (INTEGRATED AMPLIFIER PM4200, Marantz) before it is finally fed to the loudspeaker.

Chapter IV: Impedance tube experiment

Two free-field array microphones (GRAS 40PH) are attached to the impedance tube as shown in Figure IV-5 and they measure the pressure composed of the incident and reflected waves inside the tube. These microphones have a wide useful frequency range reaching up to 20 kHz and a large dynamic range topping at around 135 dB. The two microphones are attached at distances corresponding to 148 mm and 218 mm from the face of the perforated plate of the resonator. Both microphones are attached to an AD recorder (TEAC LX-110) and the recorded data is stored in a computer. For each case, ten samples with a data length of 600000 and sampling rate of 12 kHz are recorded.

The experiment is conducted at atmospheric conditions, with a temperature of approximately 13 °C and a sea-level atmospheric pressure of 101.3 kPa.

Figure IV-1 Acoustic impedance tube

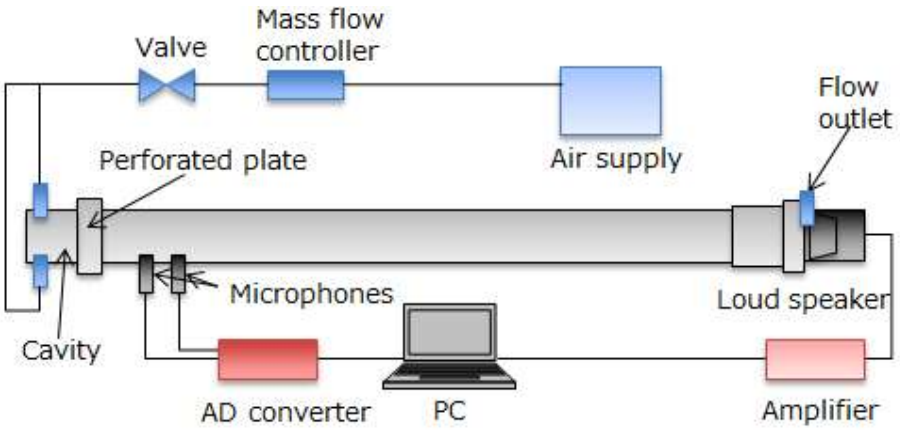

Figure IV-2 Schematic of the experimental setup

Figure IV-3 Slit on the flange for outflow of jet

Figure IV-4 Loud speaker

Figure IV-5 Installation of microphones

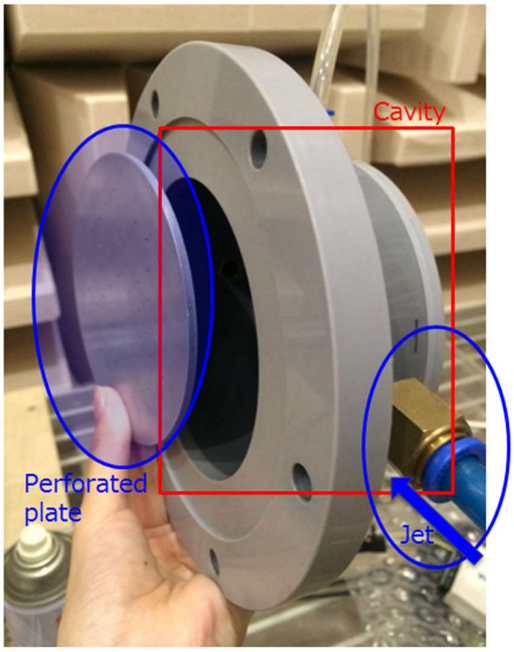

Figure IV-6 Model of active acoustic liner

2. Perforated plates

Figure IV-7 and Figure IV-8 show the geometry of the two plates with the slit apertures used. The diameter of the plates corresponds to 110 mm with a thickness of $h = 3$ mm. Each plate has only one slit aperture spanning through the center. The straight aperture in Figure IV-7 exhibits a cuboid with a width of $D = 1$ mm and length of 100 mm. The tapered aperture in Figure IV-8 exhibits a trapezoidal shape with a width of 7 mm at the base and 1 mm at the top. Both plates have an open area ratio of P = 1.27%. The open area ratio is defined as the ratio of the area of the aperture to area of the impedance tube. The dimensions of the straight and tapered plates are summarized respectively in Table IV-1 and Table IV-2.

The resonant frequency of a resonator is related to its aperture thickness h, cavity depth l, and open area ratio P and is given by Eq. (IV.1) as follows:

$$f_0 = \frac{c}{2\pi}\sqrt{\frac{P}{l(h+\delta)}} \tag{IV.1}$$

where δ denotes the end correction and c denotes the speed of sound.

For a straight slit resonator, the end correction is estimated by Eq. (IV.2) as follows:

$$\delta = KD\ ;\ K = -\frac{2}{\pi}\ln\left[\sin\left(\frac{\pi}{2}\right)\right] \tag{IV.2}$$

Subsequently, the estimated resonant frequency of the straight slit aperture is 365 Hz.

The results of the experiments discussed in a later section indicate that the resonant frequency for the straight aperture corresponds to approximately 340 Hz while the resonant frequency for the tapered aperture corresponds to approximately 460 Hz.

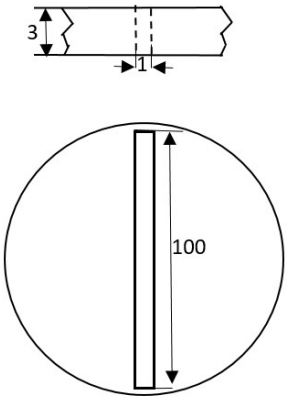

Figure IV-7 Straight aperture, unit: [mm]

Table IV-1 dimensions of the straight slit aperture

Width of the slit	1.0 mm
Length of the slit	100 mm
Open area ratio	1.27 %
Tapering angle	0 deg.
Number of apertures	1
Plate diameter	110 mm
Plate thickness	3.0 mm
Material	Aluminum

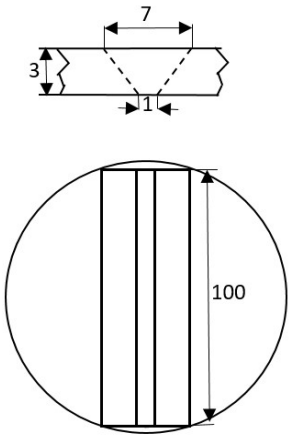

Figure IV-8 Tapered aperture, unit: [mm]

Table IV-2 dimensions of the tapered slit aperture

Width of the slit at the exit	1.0 mm
Length of the slit	100 mm
Open area ratio	1.27 %
Tapering angle	45 deg.
Number of apertures	1
Plate diameter	110 mm
Plate thickness	3.0 mm
Material	Aluminum

3. Conduction of the experiment

Here, the procedure for measuring the sound absorption coefficient in this experiment is explained.

Installation of the perforated plate

The active resonator shown in Figure IV-6 is fixed to the acoustic tube by bolts and nuts. Different perforated plates can be placed between the cavity section and the acoustic tube section. After installing the perforated plate, the bolts and nuts are uniformly tightened to fix the perforated plate resulting in an active resonator.

Measurement of acoustic data

First, white noise is output from audio signal generation software (Wave Gene [23]) from the computer, and the sound source is generated by the loudspeaker through an amplifier. Next, the mass flow controller is used to adjust the jet flow rate. After that, using TEAC LX-110, we record the acoustic data while paying attention so that the signal is not saturated. At this time, the measurement voltage is 1.0 V. For each case, ten samples with a data length of 0.6 million and sampling rate of 12 kHz are recorded.

Calculation of the sound absorption coefficient and impedance

From the acoustic data acquired, the sound absorption coefficient and impedance (resistance and reactance) are calculated based on the theory of the two-microphone method presented in Chapter III.

In this experiment, the above calculation was performed by the MATLAB program which is found in the Appendix C.

During this experiment, the frequency to be evaluated is from 200 Hz to 750 Hz, taking into consideration the cut-off frequency as well as the resonance frequency of the loudspeaker and the structural resonance frequency of the perforated plates.

4. Results of the experiment

Figure IV-9 and Figure IV-10 show the experimental absorption coefficient results for the straight and tapered slit resonators, respectively, for lower and higher sound pressure levels generated via the loudspeaker.

In the case without bias flow, the tapered aperture exhibits a resonant frequency of approximately 460 Hz. Conversely, the straight aperture exhibits a resonant frequency of approximately 340 Hz. The higher resonant frequency obtained for the tapered aperture agrees with the theoretical prediction model developed by Tang [36] for circular apertures, which predicts a higher resonant frequency for the tapered circular aperture when compared to that of a circular straight aperture.

In both apertures, the resonant frequency is shifted higher when the bias flow increases.

In the no-bias flow case, with a sound pressure level of 100 dB, the straight aperture exhibits a narrow frequency range of acoustic energy absorption located around the resonant frequency with a high peak. Conversely, the tapered aperture exhibits a wider absorption frequency range with a reduced peak and an overall poor acoustic energy absorption. When the sound pressure level increases to 115 dB, the straight aperture absorption still exhibits a narrow frequency range although an overall improvement of the absorption coefficient is obtained with a higher peak. The absorption coefficient of the tapered aperture when an SPL of 115 dB is applied also improves with a wider absorption range.

Introduction of the bias flow exhibits a tendency to widen the absorption range in the straight and tapered apertures, with a peak value reaching a maximum when the bias flow increases. A Further increase in the bias flow results in a reduced peak value. This behavior is similar to the results obtained by Wada and Ishii [37] and Tanaka et al. [38] for a liner with straight circular apertures.

As shown in Figure IV-9 and Figure IV-10, when the bias flow is applied, the sound pressure level has almost no effect on the absorption performance such that the curves for 100 dB and 115 dB exhibit almost identical values.

The peak value of the absorption coefficient for the straight aperture is when a bias flow Mach number of approximately 4.85×10^{-3} is applied. For the tapered aperture, the peak value of the absorption coefficient is at its maximum when a bias flow Mach number of approximately 9.71×10^{-3} is applied.

To better understand the sound absorption phenomenon of the active acoustic liners. The impedance of the tested resonators is also obtained and analyzed here.

It is to be noted that the absorption coefficient α can also be expressed in terms of the resistance r and reactance X of the impedance [15] as in Eq. (IV.3).

$$\alpha = \frac{4r}{(1+r)^2 + X^2} \tag{IV.3}$$

From Eq. (IV.3) it can be determined that the peak sound absorption effect is always observed at the resonance frequency which means a zero reactance $X = 0$. In that case ,the highest absorption coefficient $\alpha = 1$ is obtained at resistance $r = 1$.

Figure IV-11 and Figure IV-12 show the resistive part of the impedance for the straight and tapered apertures for different bias flow velocities. The resistance for both apertures is found to change linearly as a function of frequency with a small negative slope. The resistance also increases when the bias flow is increased.

In the case without bias flow, the difference in the resistance is large between the case of a sound pressure level of 100 dB and 115dB. With a higher resistance in the case of 115 dB sound source with the resistance at resonance going from 0.44 for the 100 dB case to 0.69 for the 115dB case. This increase of the resistance results in a higher absorption coefficient as shown in Figure IV-9 and Figure IV-10 since and increase toward the optimum resistance value of $r = 1$ leads to higher absorption coefficient.

However, in the case with bias flow, the difference in the resistance is barely noticeable between the case of a sound pressure level of 100 dB and 115dB. This leads to almost the same absorption coefficients.

In the case without bias flow, the resistance of the straight aperture is higher than the resistance of the tapered aperture.

Figure IV-13 and Figure IV-14 show the reactive part of the impedance for the straight and tapered apertures for different bias flow velocities.

In the case without bias flow, the reactance of the tapered aperture is much lower at high frequencies compared with straight aperture. From Eq. (IV.3), it can be deduced that the main reason of the higher absorption obtained with the tapered aperture at higher frequencies is due to the lower value of the reactance.

In the case of bias flow, the reactance just decreases slightly as the bias flow velocity is increased. However, the resistance increases significantly as the bias flow is increased. The reason of the broadening of the absorption frequency range when bias flow is introduced is due mainly to the increase in resistance. Near the resonance frequency, the resistance is almost equal to $r = 1$ when the bias flow Mach number is approximately 4.85×10^{-3} for the straight aperture. Also, the resistance is almost equal to one when a bias flow Mach number of approximately 9.71×10^{-3} is applied in the case of the tapered aperture.

When the bias flow is increased further, we can see that the resistance at the resonance frequency becomes higher than the optimum value of $r = 1$. This leads to lower peak absorption coefficient. However, this also increases the absorption coefficient at off-resonance frequencies.

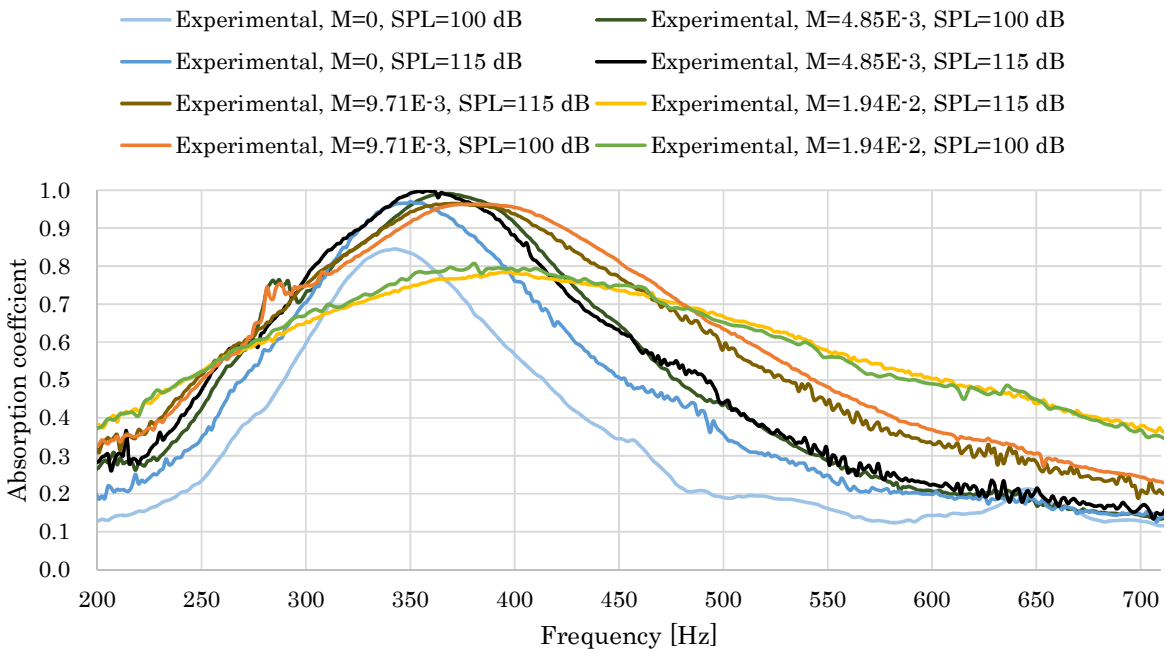

Figure IV-9 Absorption coefficient for the straight aperture

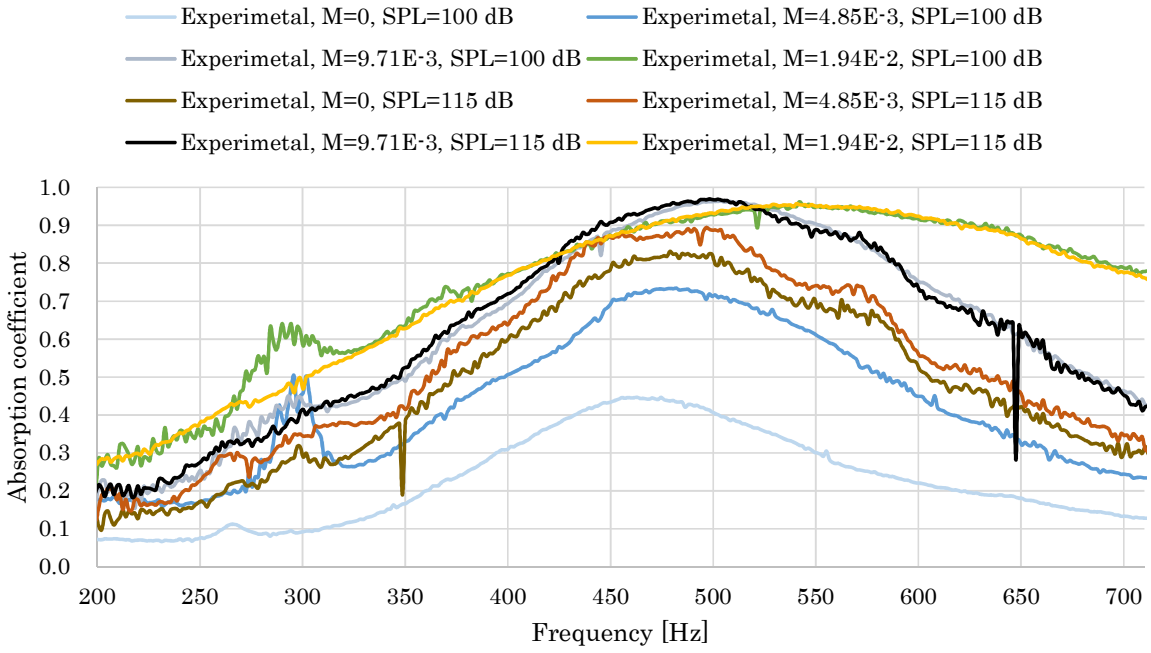

Figure IV-10 Absorption coefficient for the tapered aperture

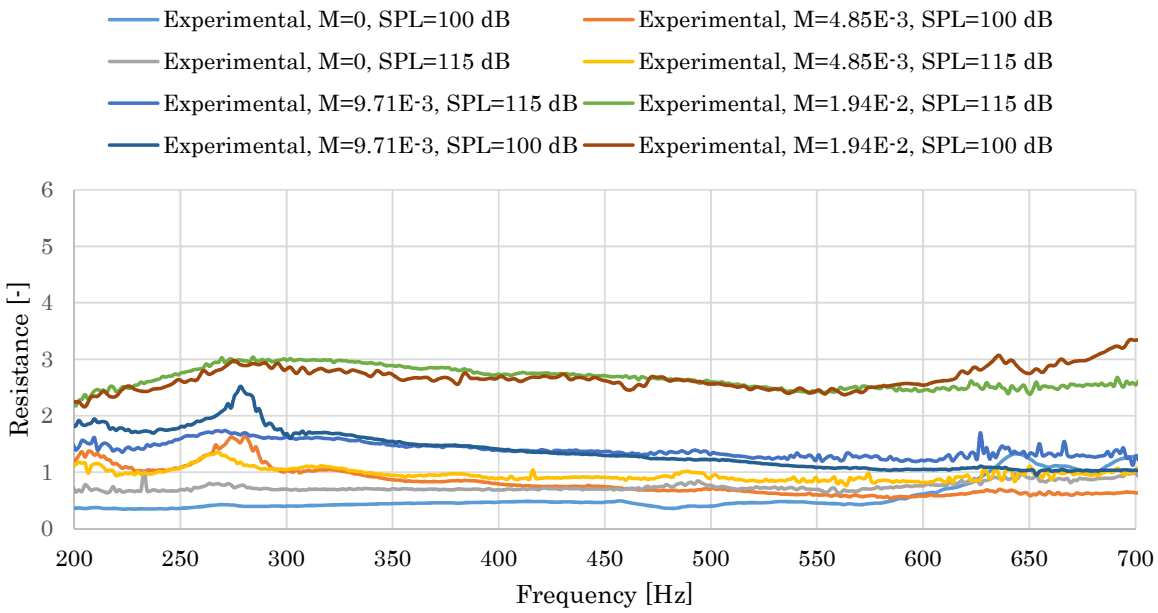

Figure IV-11 Resistance of the straight aperture

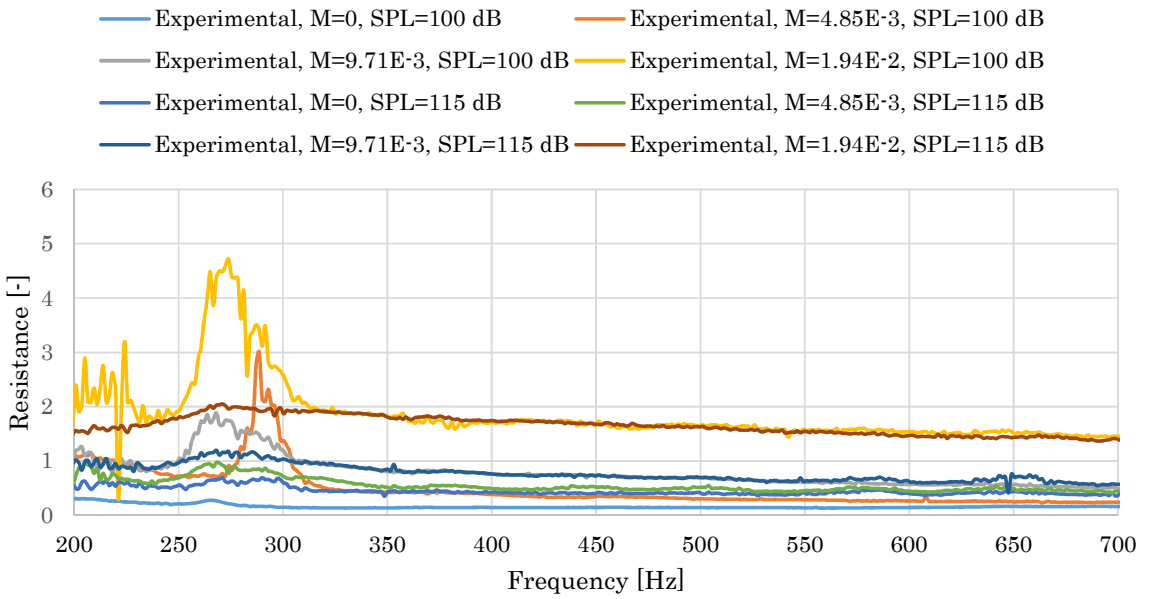

Figure IV-12 Resistance of the tapered aperture

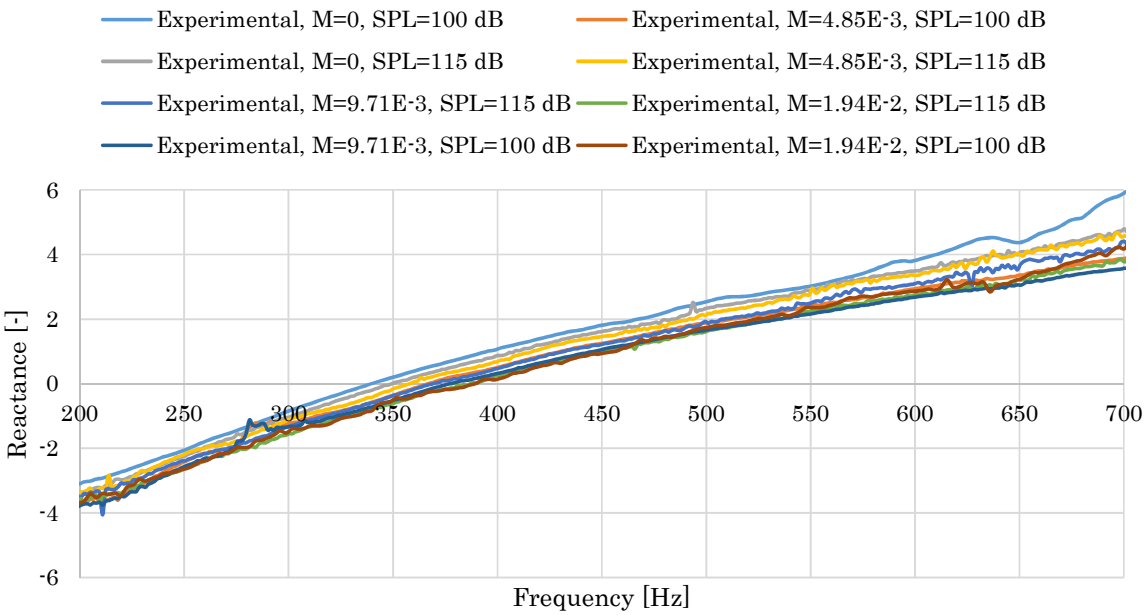

Figure IV-13 Reactance of the straight aperture

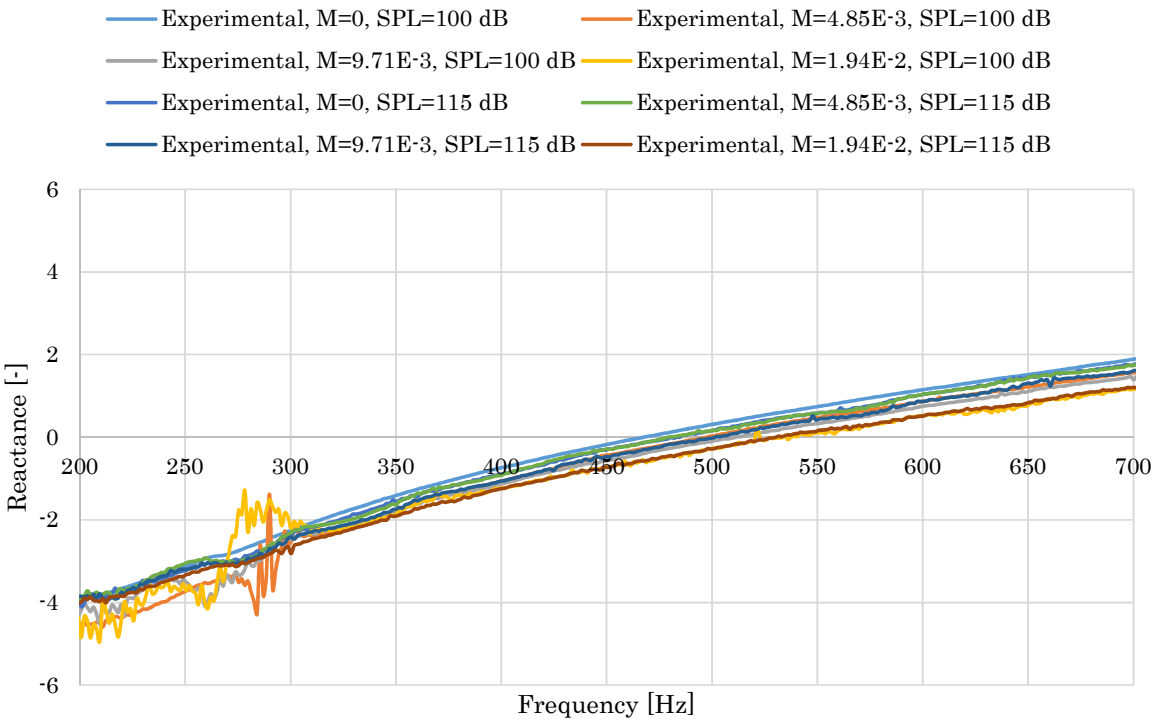

Figure IV-14 Reactance of the tapered aperture

Chapter 5

V. 2D Numerical Simulations

In this chapter, the acoustic performance of the liner and the flow field around the perforated plate is numerically solved using the compressible Navier-Stokes equations to understand the acoustic and fluid dynamic behavior of the liner and the effect of the shape of the perforation at a microscopic level.

Two different studies are conducted on different acoustic resonators dimensions and shapes. First, the numerical study of the resonators studies experimentally in Chapter IV are conducted with and without bias flow in the linear regime with a sound pressure level of the sound source of 100 dB, and also at 115dB where the regime is not perfectly linear. Then the numerical study of a resonator previously study by Tam et al. [21] is conducted at high sound pressure levels of 130 dB and 150 dB.

1. Numerical Simulation of 2D acoustic liner based on our experiments

In this section, the simulations are conducted using 2D large eddy simulations. For the 2D assumption to be acceptable, the impedance tube experiment is conducted on slit apertures where slit indicates that each plate has only one aperture with a high aspect ratio of 100. The aperture spans through the center of the plate.

Subsequently, numerical simulations are conducted and validated with the experimental results. Moreover, the effect of bias flow on the absorption performance of the acoustic liner and flow field around the apertures are discussed.

1.1. Models and grid

Figure V-1 shows the geometry and dimensions of the slit resonator analyzed. The length of the impedance tube is set to $500D$. The width of the aperture is $D = 1$ mm and the thickness of the perforated plate is $h = 3D$ and it contains slits of dimensions shown in Figure V-2 and Figure V-3. The cavity has a depth of $l = 52D$ and a width of $W = 78.5D$.

The non-dimensionalized time t, coordinate variables x_i, velocities u_i, pressure p, and vorticity Ω are calculated as follows:

$$t = \frac{t^*}{D/c} \quad , \quad x_i = \frac{x_i{}^*}{D} \quad , \quad u_i = \frac{u^*}{c} \quad , \quad p = \frac{p^*}{\rho c^2} \; , \; \Omega = \frac{\Omega^*}{c/D} \tag{V.1}$$

The calculation domain consists of 36 blocks with a higher resolution in the blocks close to the aperture. The resolution is lower for the blocks away from it. This is because the length scale at a distance from the aperture is in the range of the wavelength. However, near the aperture, an oscillatory viscous wall layer called the Stokes layer is formed, and it should be captured. The Stokes layer exhibits a length scale that is extremely low when compared to the wavelength.

The Stokes layer wavelength is calculated using Eq.(V.2) [39].

$$\lambda_{stokes} = \left(\frac{4\pi\nu}{f}\right)^{1/2} \tag{V.2}$$

where

λ_{stokes} : The Stokes layer wave length

f : Frequency of oscillation

ν : Kinematic viscosity

The Stokes layer should be resolved for the maximum frequency simulated within a minimum of eight grid points $\lambda_{stokes}/8$.

The grid spacing in the aperture used in this study corresponds to $D/79$ in the y direction and $h/79$ in the x direction. This resolution can resolve the Stokes layer and the viscous sublayer of the boundary layer with a dimensionless wall distance (y^+) that corresponds to 1.

The number of cells in the z direction corresponds to one with the symmetric boundary condition applied on both sides.

The non-dimensional time step is selected as $\Delta t = 3.15 \times 10^{-3}$, and leads to a CFL number lower than 1.

Room temperature of 293.15 K and atmospheric pressure of 101.3 kPa are given as initial conditions for the numerical simulations. Given these conditions, density is $\rho = 1.2$ kg/m^3 and speed of sound is $c = 343.2$ m/s. The absorption coefficient for each case is calculated with data length equivalent to 10 incident waves such that each wave is captured by 20 data points.

The 6th-order compact scheme with the 10th-order compact filter is used to solve the convective terms of the conservation equations, while the 2nd-order central discretization is used for the viscous terms.

The obtained space discretized equations are then integrated in time via the 3rd-order Runge-Kutta explicit scheme.

The model analyzed in this section is shown in Figure V-4 and represents the case of the perforated plate backed by a cavity with a mass source region that can be activated to introduce a bias flow passing through the aperture.

The geometry of the model and applied boundary conditions are shown in Figure V-4. It contains an outlet with a far-field boundary condition, which corresponds to a non-reflective boundary condition using the characteristic waves and the inner points to determine the boundary conditions. The cavity is backed by a non-slip wall boundary condition. Symmetric boundary conditions are applied to the sides, and non-slip walls are applied to the perforated plate. Additionally, a sound source is applied at a distance of 400D from the aperture. The details of the boundary conditions implementation is explained in details in Appendix B.

When simulating the bias flow case, first, the bias flow jet is fully developed. The simulation is run for 72 hours and it requires about 1.5 million iterations. The convergence is verified by checking the convergence of the residuals and also by verifying the value of the bias flow at the aperture which should be equal to the desired bias flow. Then, the sound wave source is enabled. The time required for three waves to propagate is found to be enough for all the frequencies simulated before starting the sampling process.

The simulations are conducted for frequencies from 200 Hz to 700 Hz for both tested plates and with sound pressure level (SPL) values corresponding to 100 dB and 115 dB for both plates.

The results indicated that the SPL significantly affects the absorption performance for both the experiment and simulation. Therefore, we tested two different SPLs of 100 dB and 115 dB. The reason for the dependency on SPL is discussed in the subsequent sections.

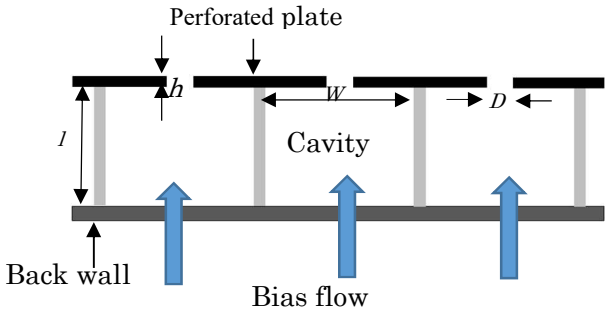

Figure V-1 Layout of acoustic liners

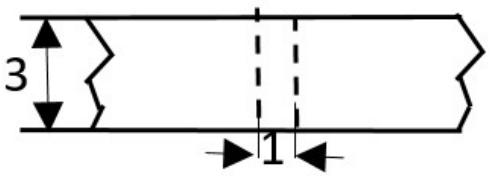

Figure V-2 Straight aperture

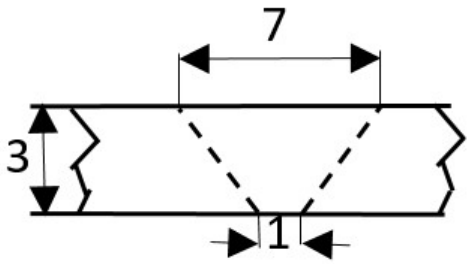

Figure V-3 Tapered aperture

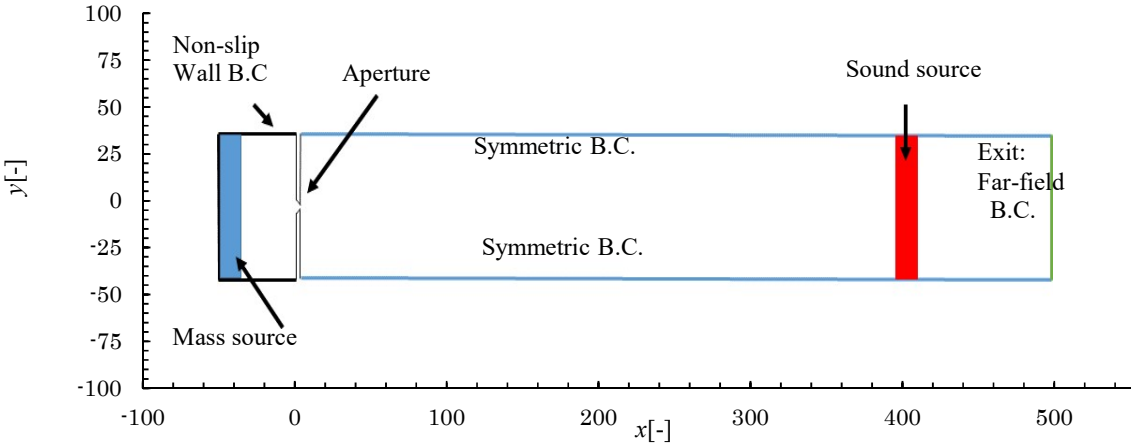

Figure V-4 Sources locations and boundary conditions

1.2. Numerical results and discussion

1.2.1. Absorption coefficient.

Figure V-5 compares results of the absorption coefficients obtained experimentally and numerically for the straight slit aperture. Incident sound pressure levels of approximately 100 dB and 115 dB are considered. In the case without bias flow, at 100 dB SPL, the numerically and experimentally obtained results are in good agreement. At 350 Hz, a 10% difference is observed.

The numerical results also indicate that the absorption performance is affected by the sound pressure level of the sound source. A higher absorption coefficient at 115 dB is obtained when compared to the 100 dB case for frequencies equal to and lower than the resonant frequency. However, the results obtained at higher frequencies do not capture this improvement in the absorption performance.

When the bias flow of Mach number $M = 9.71 \times 10^{-3}$ is applied, the numerical results are in good agreement with the experimental results.

Figure V-6 shows a comparison of the absorption coefficients between results obtained experimentally and the results obtained via numerical simulations for the tapered slit aperture resonator. Incident sound pressure levels approximately corresponding to 100 dB and 115 dB are considered. In the case without bias flow, at 100 dB SPL, the numerically and experimentally obtained results are in good agreement.

The absorption coefficient results numerically obtained for the resonator are largely affected by the applied sound pressure level with a higher performance for the 115 dB sound pressure level source when compared to that of the 100 dB case. Additionally, the numerical and experimental results are in good agreement.

In the case of $M = 9.71 \times 10^{-3}$ bias flow, the numerically obtained values are in good agreement with the experimental results for the frequencies around the resonant frequency. For frequencies away from the resonant frequency, the numerical results are overestimated compared to the experimental results although the trend is still well captured.

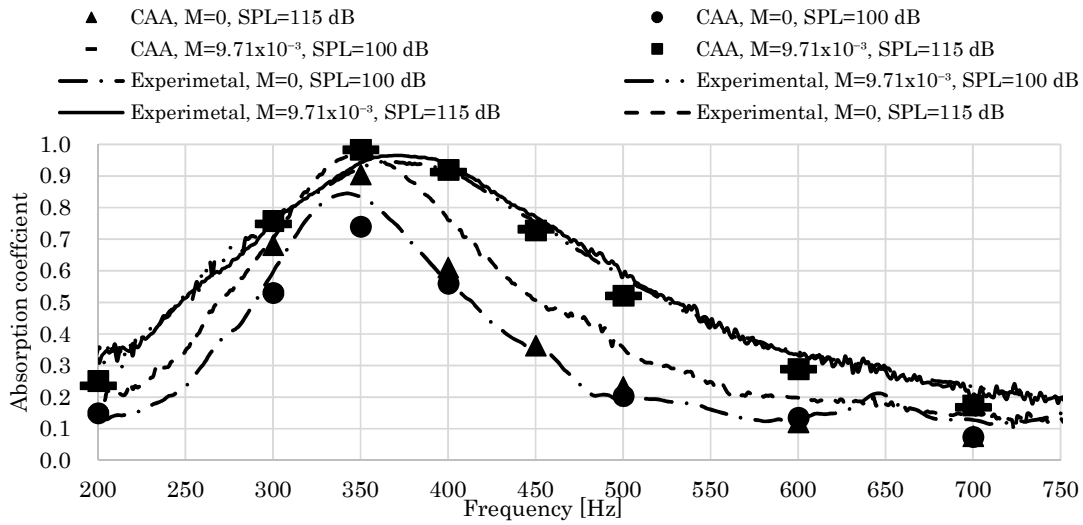

Figure V-5 Absorption coefficients for the straight slit aperture

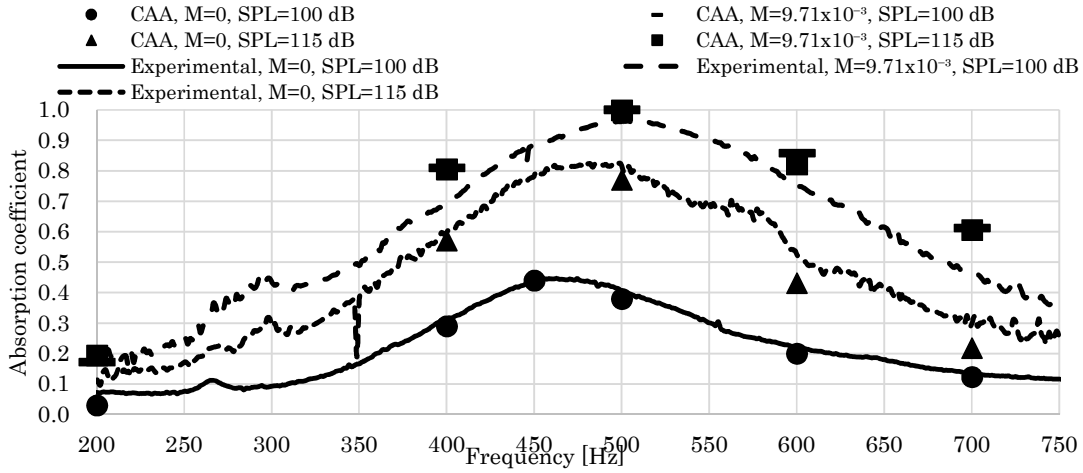

Figure V-6 Absorption coefficients for the tapered slit aperture

1.2.2. Flow field.

All the flow field snapshots are obtained with respect to the instant where the area average velocity oscillation at the inlet of the aperture corresponds to a maximum. It should be noted that each period T of the acoustic wave is divided into 20 steps.

Figure V-7 and Figure V-8 show snapshots of the unsteady vorticity contour around the straight aperture in the case of sound pressure levels corresponding to 100 dB and 115 dB, respectively. Both cases occur at an excitation frequency of 350 Hz which is close to the resonant frequency. For the 100 dB case, a shear layer is generated near the wall, although shed vortices are absent. Conversely, for the 115 dB case, in addition to the shear layer, larger vortices are created at the extremities of the aperture with higher vorticity magnitude. The existence of the vortices is the reason for the improvement of the calculated absorption coefficient when compared with the 100 dB case. Such improvement is due to the conversion of acoustic energy to vortical kinetic energy, which is subsequently dissipated via viscous dissipation.

Figure V-9 and Figure V-10 show snapshots of the unsteady vorticity contour around the straight aperture in the case of sound pressure levels corresponding to 100 dB and 115 dB, respectively. Both cases occur at an excitation frequency of 350 Hz, with an applied bias flow of Mach number $M=9.71\times 10^{-3}$. At 100 dB, weak vortices embedded in the vorticity sheet are observed. At 115 dB, stronger vortices are shed on the right side of the aperture. The absorption coefficient is not affected despite the clear difference in the flow field between the two cases. This shows that the bias flow forces the resonator response to the linear regime.

Figure V-11 and Figure V-12 show snapshots of the unsteady vorticity contour around the tapered aperture in the case of sound pressure levels corresponding to 100 dB and 115 dB. Both cases occur at an excitation frequency of 500 Hz. With respect to the 100 dB case, a shear layer is generated near the wall with weak vorticity magnitude. The absence of vortices is the reason as to why the weak absorption coefficient is obtained in the experiment and in numerical simulation. With respect to the 115dB case, in addition to the shear layer in the tapered aperture, the shear layer rolls up at the tip of the aperture creating vortices that are shed away. The shed vortices are the reason for the improvement in the absorption coefficient when compared to that in the 100 dB case. The sharp edge of the tapered aperture appears to aid in increasing the instability of the generated vortices, thereby resulting in their detachment from the aperture walls.

Figure V-13 and Figure V-14 show snapshots of the unsteady vorticity contour around the tapered aperture in the case of sound pressure levels corresponding to 100 dB and 115 dB, respectively. Both cases occur at an excitation frequency of 500 Hz, with an applied bias flow of $M = 9.71\times 10^{-3}$. With respect to the 100 dB case, a vorticity sheet is observed on the right side of the aperture. A jet is formed and accompanied by a shear layer that is formed near the walls of the aperture, and the shear layer rolls up to create a continuous vorticity sheet. However, at 115 dB, the shear layer creates discrete vortices of higher magnitude that are shed away. The absorption coefficient is not affected despite the clear difference in the flow field between the two cases.

Figure V-15 and Figure V-16 show the time-averaged viscous dissipation (Eq. (III.21)) for an acoustic wave with instantaneous streamlines around the straight and tapered apertures, respectively. The cases of a sound source of 115 dB and relatively high frequency of

700 Hz are chosen. The frequency is selected to understand the reason for the wider absorption frequency range obtained for the tapered aperture.

With respect to the straight aperture, viscous dissipation is caused by friction near the walls of the aperture with small vortices attached to the corners. With respect to the tapered aperture, in addition to the friction of walls, a large area of viscous dissipation is caused at the sharp edges of the aperture where vortices are generated. These vortices hold the converted acoustic energy that is absorbed via viscous dissipation.

Time-averaged viscous dissipation integrated over the calculation domain (Eq. (III.20)) in Figure V-15 and Figure V-16, for the tapered aperture is approximately 2.8 times that for the straight aperture. The absorption coefficient for the tapered aperture is also approximately 2.8 times that of the straight aperture.

With respect to the 115dB SPL case for the straight aperture, the underestimation of the absorption coefficient at higher frequencies in the numerical simulation when compared to the experimental results is potentially attributed to the existence of vortices around the aperture in the experiment, thereby leading to the nonlinear response of the resonator. As shown in Figure V-16, vortices are absent in the simulation and thus the resonator response is in the linear regime.

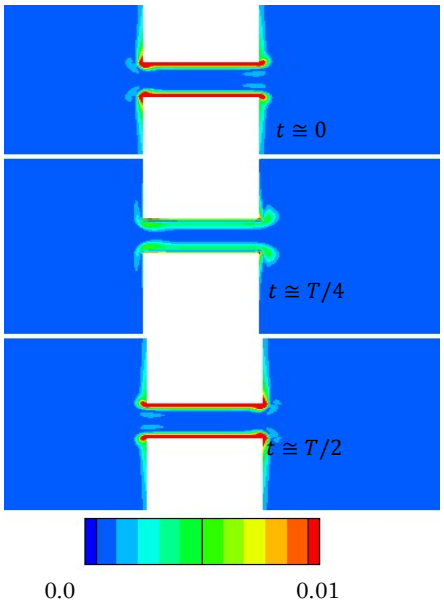

Figure V-7 Non-dimensional vorticity magnitude, straight aperture, 350 Hz and 100 dB without bias flow

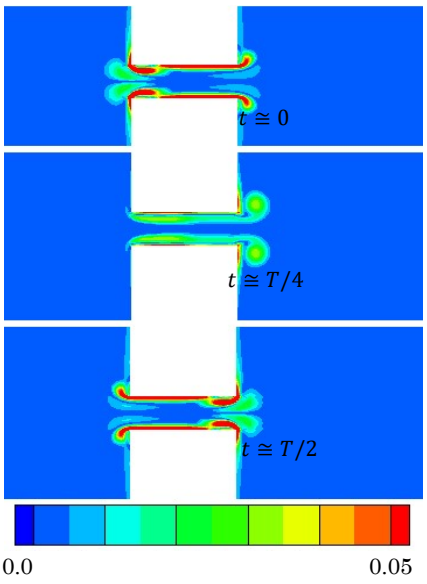

Figure V-8 Non-dimensional vorticity magnitude, straight aperture, 350 Hz and 115 dB without bias flow

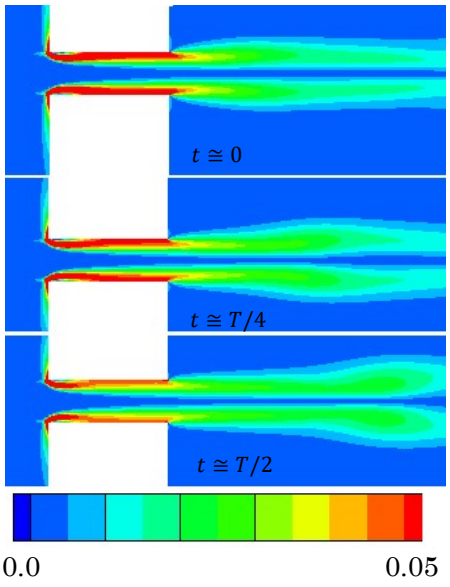

Figure V-9 Non-dimensional vorticity magnitude, straight aperture, M=9.71× $\mathbf{10^{-3}}$, 350 Hz and 100 dB

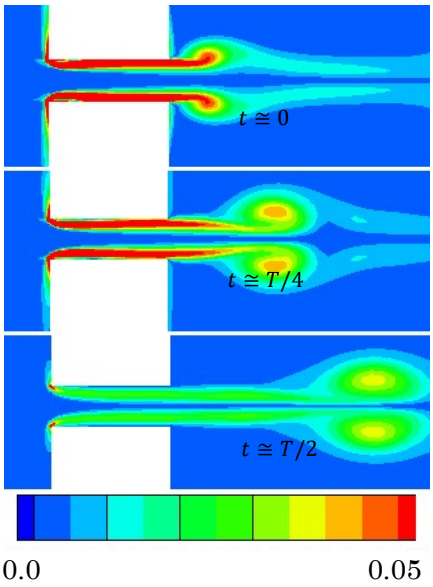

Figure V-10 Non-dimensional vorticity magnitude, straight aperture, M=9.71× $\mathbf{10^{-3}}$, 350 Hz and 115 dB

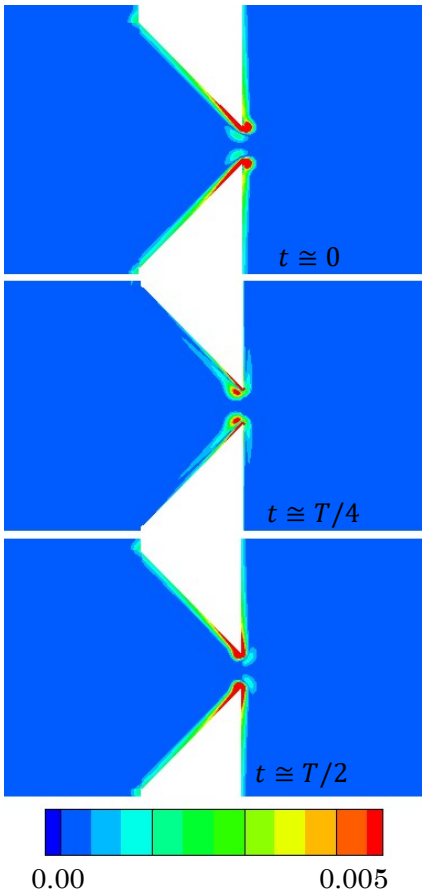

Figure V-11 Non-dimensional vorticity, tapered aperture, 500 Hz and 100 dB without bias flow

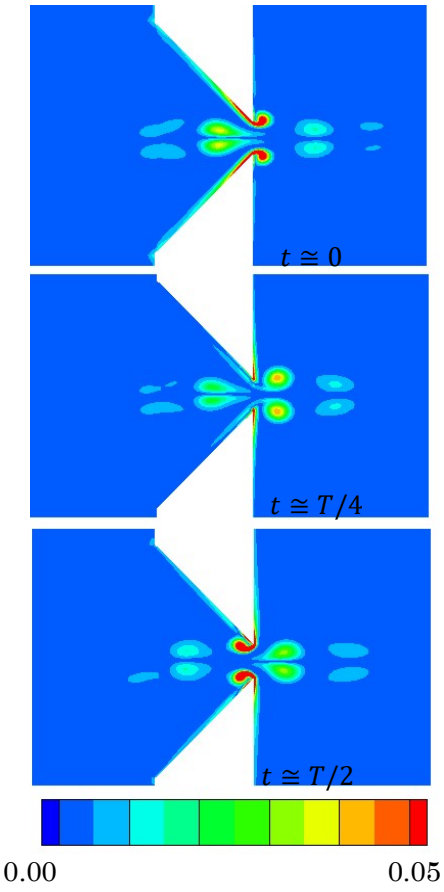

Figure V-12 Non-dimensional vorticity, tapered aperture, 500 Hz and 115 dB without bias flow

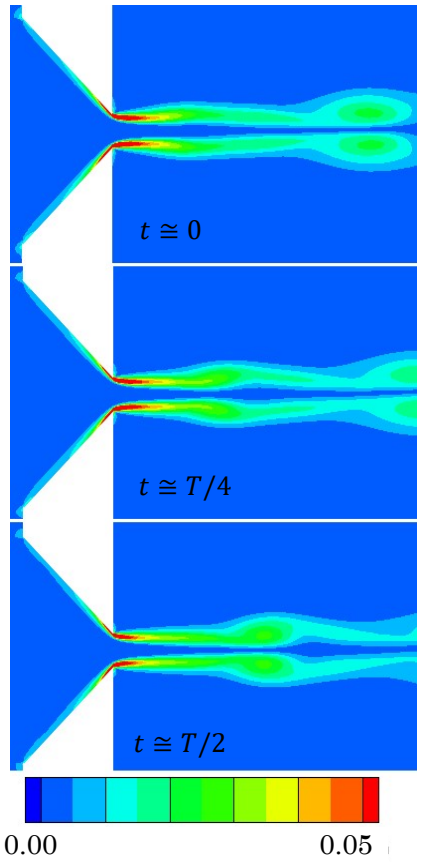

Figure V-13 Non-dimensional vorticity magnitude, tapered aperture, M=9.71× $\mathbf{10^{-3}}$, 500 Hz and 100 dB

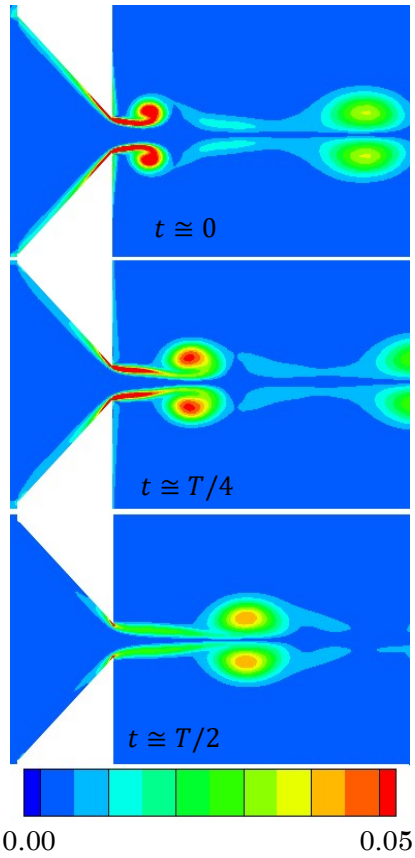

Figure V-14 Non-dimensional vorticity magnitude, tapered aperture, M=9.71× $\mathbf{10^{-3}}$, 500 Hz and 115 dB

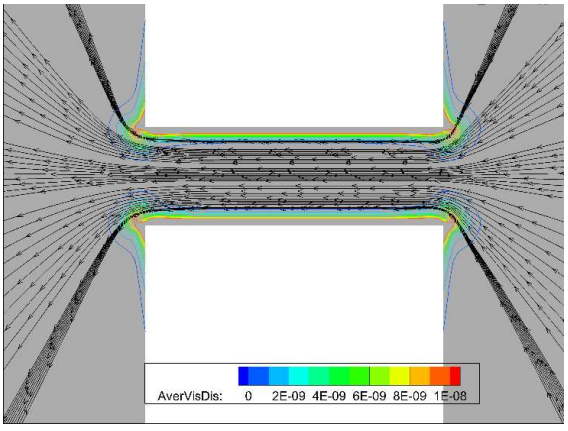

Figure V-15 Time-averaged viscous dissipation, straight aperture, without bias flow 700 Hz, 115 dB t≅T/2

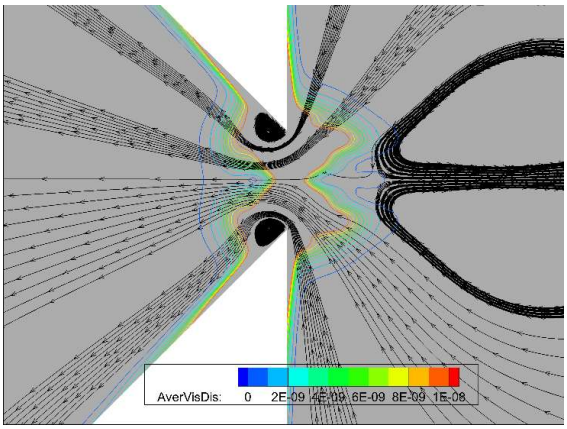

Figure V-16 Time-averaged viscous dissipation, tapered aperture, without bias flow 700 Hz, 115 dB, $t \cong T/2$

2. Numerical Simulation of 2D acoustic liner based on Tam's experiments

In a previous study, Tam et al. [21] conducted the Direct Numerical Simulations (DNS) for a 2D slit resonator of resonance frequency around 1 kHz for a range of frequencies of the sound source from 1 kHz to 6 kHz and sound pressure levels of 130 dB and 150 dB. The absorption coefficients were obtained by evaluating the absorbed energy as the sum of the rate of viscous dissipation and the rate at which the energy is transferred to shed vortices. These simulations were validated by experiments using an acoustic impedance tube, in the same conditions. Good agreement was obtained for the absorption coefficients, except for the case of the sound source of 2 kHz and 130 dB where the experimental sound absorption coefficient is much larger than the simulated one.

In this research, the large eddy simulations of a 2D slit liner are conducted, and the results of these simulations are validated using DNS and experimental results obtained by Tam et al. [1]. Then the acoustic performance of the liner is investigated when a bias flow is introduced through the aperture. The aim is to understand how the bias flow influences the absorption capabilities of the 2D slit liner, and how to take account of these changes qualitatively and quantitatively.

2.1. Models and grid

Figure V-1 shows the geometry and dimensions of the slit resonator analyzed in this study. The chosen liner was previously studied by Tam et al. [21] experimentally and using Direct Numerical Simulation (DNS) for the case of a conventional acoustic liner under normal sound wave incidence. The perforated plate of thickness $h = 0.8$ mm contains slits of width $D = h$. The cavity has a depth equal to $l = 36D$ and a width of $W = 28D$, where D is the aperture width.

The estimated resonance frequency for this geometry is calculated using the formulae for infinite length slit given in Eqs. (IV.1) and (IV.2). The resonance frequency is estimated to $f_0 = 1257$ Hz.

The results obtained by Tam et al. [21] serves for the validation of the results obtained in the present research. Moreover, in this study, the focus is on the numerical simulation of the influence of bias flow on the absorption performance of a slit liner using LES.

The models analyzed in this section are shown in Figure V-17 and Figure V-18. They both represent the case of the perforated plated backed by a cavity with and without bias flow passing through the aperture with the difference that the model in Figure V-17 is reduced to only one-half of the model in Figure V-18 in order to reduce the calculation cost and to verify the symmetry of the problem.

The room temperature of 288.15 K and the atmospheric pressure of 101.3 kPa are given as initial conditions of the simulation.

The geometry of the model and the applied boundary conditions are shown in Figure V-17. It contains one outlet with a far-field boundary condition, while the cavity is backed by a non-slip wall boundary condition, symmetric boundary conditions are applied to the sides to satisfy the condition of non-interaction between the apertures, and non-slip walls are applied to the perforated plate. The details of the boundary conditions implementation is explained in details in Appendix B.

In addition, a sound source is applied at a distance of 160.5D from the aperture with the properties presented in Table V-1.

The relation between the acoustic pressure of the sound source wave and sound pressure level is calculated using Eq. (V.3).

$$p_a = 2\times10^{\left(\frac{SPL}{20}-5\right)} = \begin{cases} 63 \text{ Pa for } SPL = 130 \text{ dB} \\ 632 \text{ Pa for } SPL = 150 \text{ dB} \end{cases} \tag{V.3}$$

where

p_a : Acoustic pressure

SPL : Sound pressure level in decibel

On the other hand, the acoustic particle velocity is calculated as the ratio of the acoustic pressure and the characteristic impedance.

$$u_a = \frac{p_a}{Z_0} = \begin{cases} 0.15\,\text{m/s} \text{ for } SPL = 130\text{dB} \\ 1.53\,\text{m/s} \text{ for } SPL = 150\text{dB} \end{cases} \tag{V.4}$$

where

u_a : Acoustic particle velocity

Z_0 : Characteristic acoustic impedance of air $Z_0 = \rho c$, the density of the air is $\rho = 1.22\ \text{kg/m}^3$ and the speed of sound is $c = 340.3\ \text{m/s}$

The calculation domain is made of eight blocks with a higher resolution in the blocks close to the aperture. While the resolution is lower for the blocks away from it. This is because the length scale far from the aperture is in the range of the wavelength, however near the aperture, an oscillatory viscous wall layer called the Stokes layer is formed and it should be captured. The Stokes layer has a length scale that is very small compared to the wavelength.

The grid spacing in the aperture is of 0.025 mm ($0.0308D$) necessary to resolve the Stokes layer within eight grid points $\lambda_{stokes}/8$. This value is calculated for a maximum frequency of 6 kHz.

The number of cells in the z direction is equal to one, with symmetric boundary conditions applied from both sides.

The non-dimensional time step is chosen to be $\Delta t = 1.05 \times 10^{-2}$ leading to a CFL number lower than 1.

Table V-1 Sound source conditions.

130 dB	150 dB
1 kHz	1 kHz
1.1kHz	-
2 kHz	2 kHz
3 kHz	3 kHz
4 kHz	4 kHz
6 kHz	6 kHz

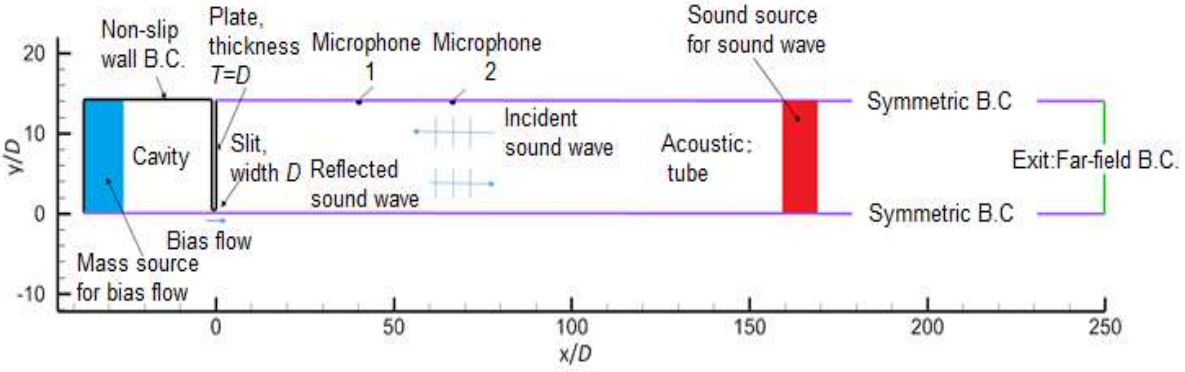

Figure V-17 Boundary conditions of half resonator with symmetry assumption

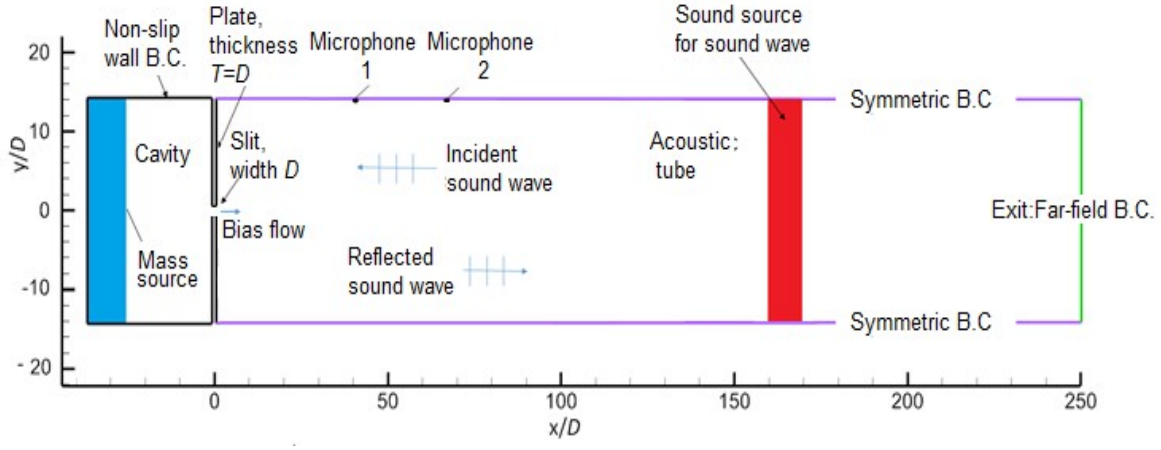

Figure V-18 Boundary conditions of full Resonator

2.2. Numerical results and discussion

2.2.1. Symmetry assumption verification

In this section, the validity of the symmetry assumption of the model in Figure V-17 is investigated. A comparison of the flow field and the absorption coefficients using the two-microphone method is given for both models shown in Figure V-17 and Figure V-18 under normal sound pressure levels of 130 dB and 150 dB in the cases with and without bias flow.

Figure V-19 and Figure V-20 show the flow field for a conventional acoustic liner with sound pressure level of 130 dB and 150 dB, respectively. The flow is found to behave in a symmetrical way.

Table V-2 compares the absorption coefficients in the case of the application of 1 kHz sound wave of 130 dB and 150 dB sound pressure levels, for the full domain and half-domain simulations.

Table V-2 Absorption coefficients for resonator without bias flow

150 dB		130 dB	
Full domain	Half domain	Full domain	Half domain
0.81	0.85	0.62	0.60

Considering the agreement of the results of the full domain and half-domain simulations, only the half-domain model will be considered in the following section concerning the results for the conventional acoustic liner. Roche et al. [18] also considered the 2D axisymmetric and compared it to the full three-dimensional resonator and good agreement was obtained for the case of the conventional acoustic liner.

On the contrary, Figure V-21 and Figure V-22 show the flow field for a bias flow active acoustic liner with sound pressure levels of 130 dB and 150 dB, respectively.

The symmetry assumption in the bias flow case is not convenient anymore.

Table V-3 compares the absorption coefficients in the case of the application of 1 kHz sound wave of 130 dB and 150 dB sound pressure levels, for the full domain and half-domain simulations when a bias flow is introduced.

It can be seen that even though the flow field is different, the calculated absorption coefficients still agrees between full and half-domain cases. The full domain case will be considered in the next section and compared to the half-domain case.

Table V-4 summarizes the conditions where the symmetry assumption is correct.

Table V-3 Absorption coefficients for resonator with bias flow

150 dB		130 dB	
Full domain	Half domain	Full domain	Half domain
0.86	0.85	0.76	0.75

Table V-4 Symmetry

	130 dB	150 dB
Without bias flow	symmetric	symmetric
With bias flow	Not symmetric	Not symmetric

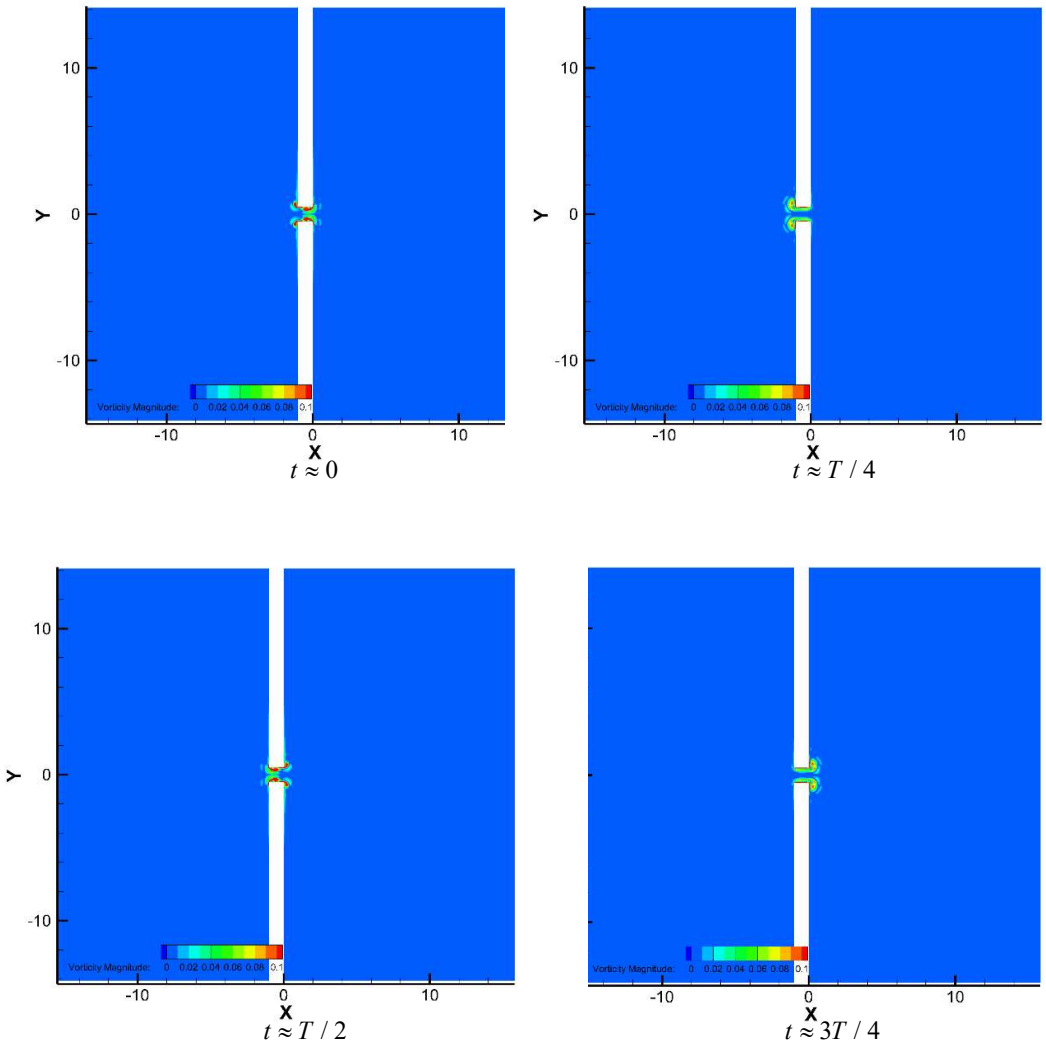

Figure V-19 Snapshots of the unsteady flow at the aperture: Vorticity contours-130 dB 1 kHz without bias flow

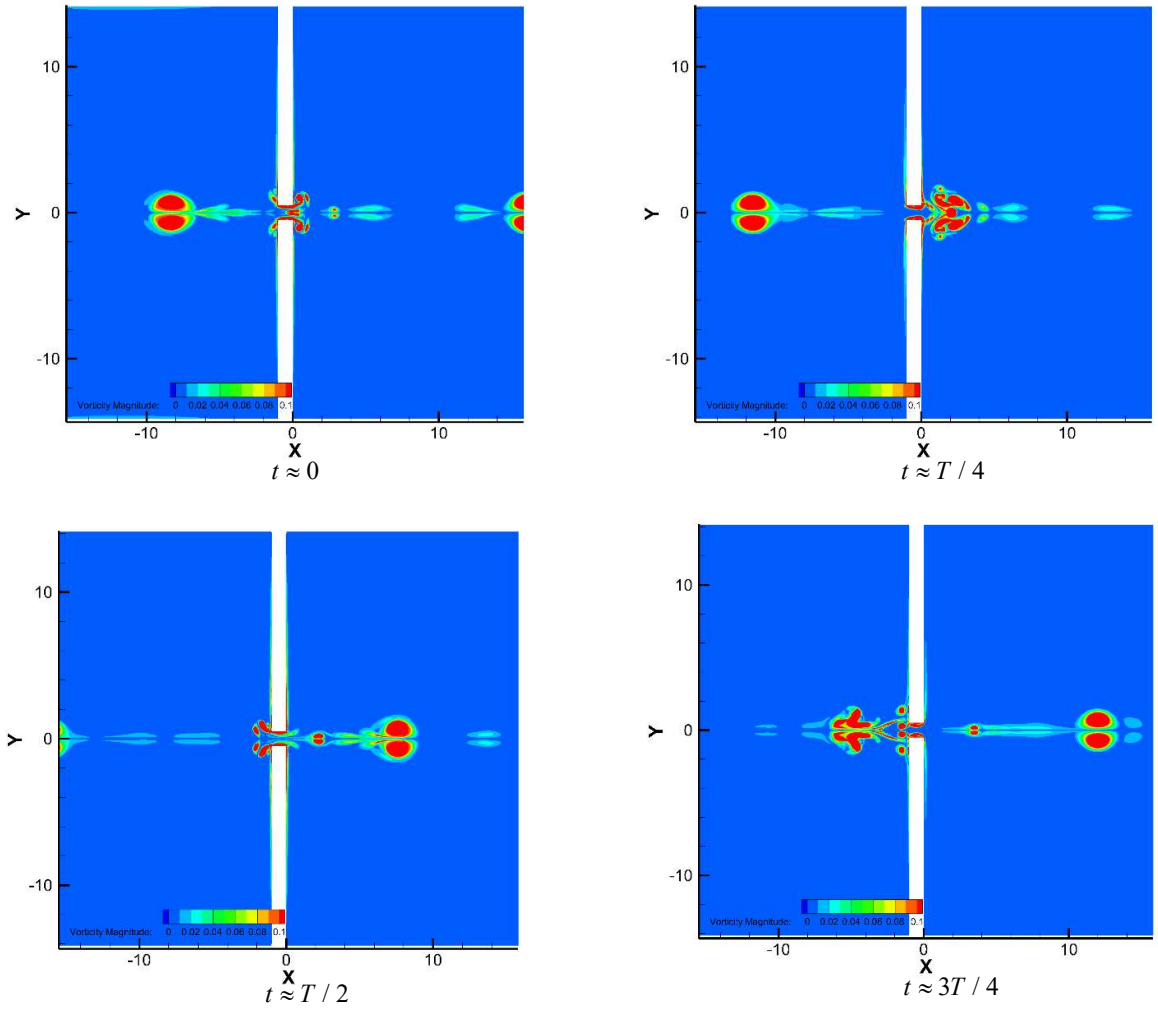

Figure V-20 Snapshots of the unsteady flow at the aperture: Vorticity contours-150 dB 1 kHz without bias flow

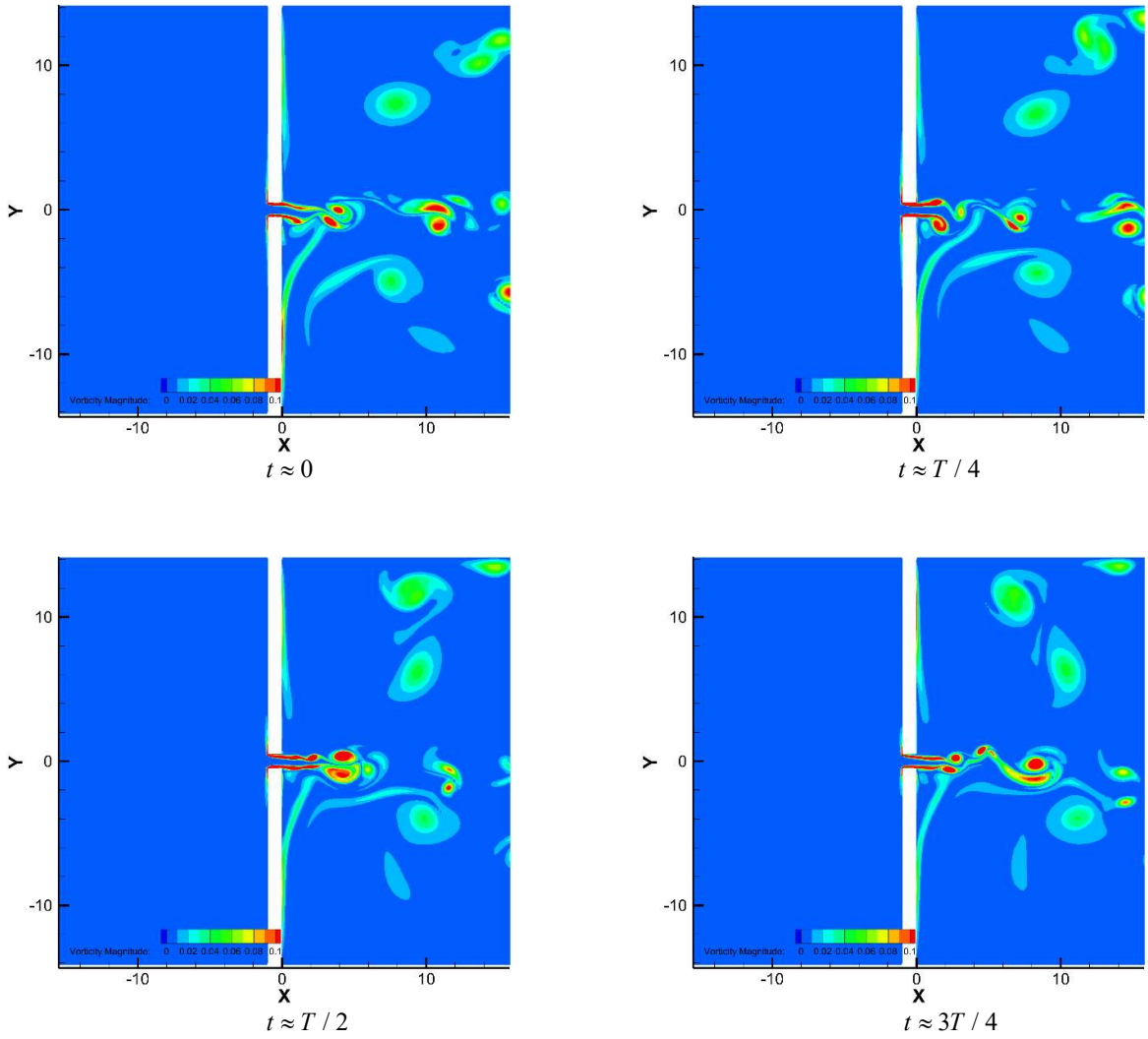

Figure V-21 Snapshots of the unsteady flow at the aperture: Vorticity contours-130 dB 1 kHz with bias flow

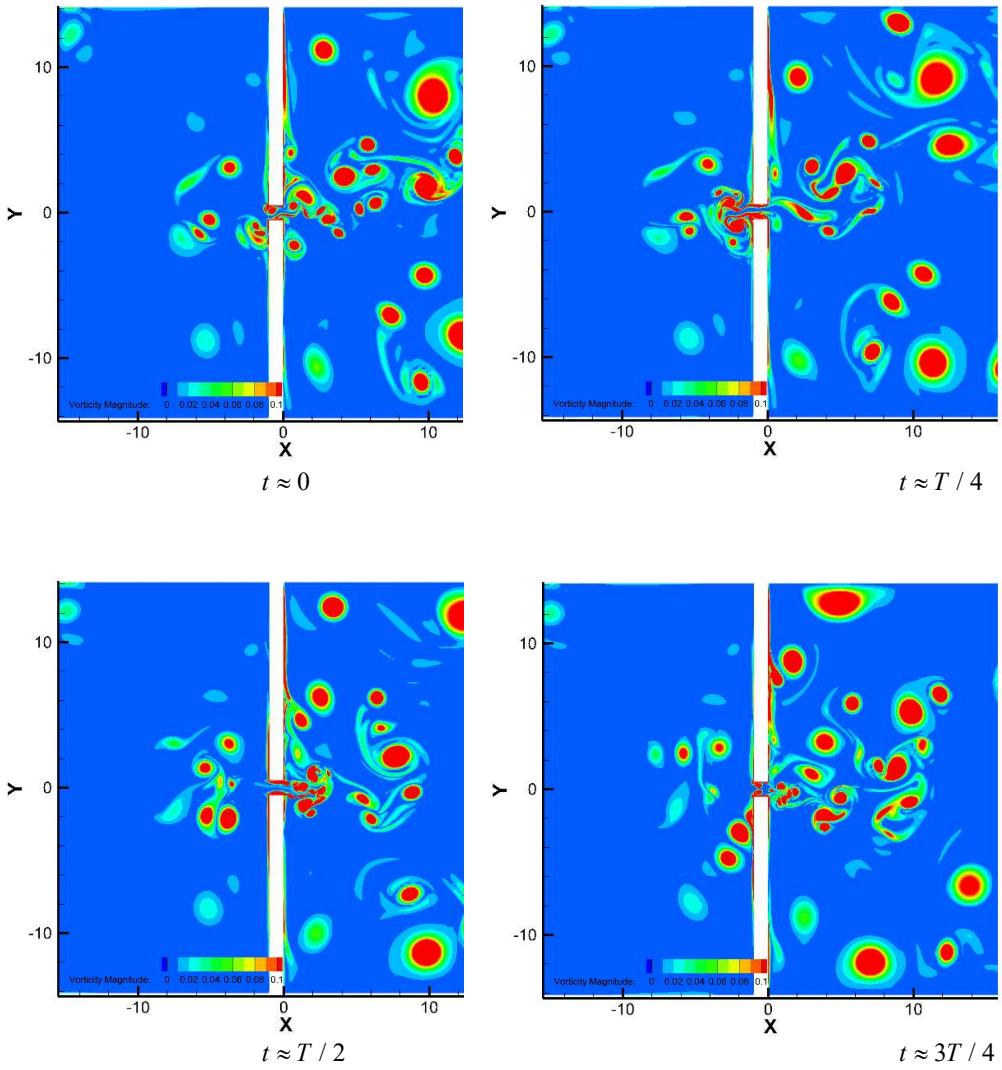

Figure V-22 Snapshots of the unsteady flow at the aperture: Vorticity contours-150 dB 1 kHz with bias flow

2.2.2. Absorption coefficient

Two different methods are used to calculate the absorption coefficient in the CAA simulation of the resonator. The first method is the transfer function method, and it simulates the acoustic impedance tube used in the experiment. The second method is the viscous dissipation method, and it evaluates the acoustic power converted in viscous dissipation. The two different methods were explained in Chapter. III.

2.2.2.1. Numerical Simulation of 2D Conventional Acoustic Liner

Figure V-23 shows a comparison of the absorption coefficient for an incident sound pressure level equal to 130 dB, between results obtained experimentally in a normal incident impedance tube (EXP-130) and the direct numerical simulations (DNS-130) conducted by Tam et al. [21] and the results obtained in this study using LES.

The results of the absorption coefficients calculated using the transfer function method (two-microphone method) TMM-130 and the viscous dissipation method VD-130 for frequencies equal or higher than 2 kHz in this study agree well with results obtained in the simulations using DNS by Tam et al [1], and in good agreement with the experiments by Tam et al [21] for frequencies equal or higher than 3 kHz.

In DNS for a frequency of 2 kHz, a difference with the experimental value is observed with respect to the absorption coefficient. Similarly, the result obtained by the present LES agrees with DNS. Tam et al. [21] speculated that the reason for a very low absorption coefficient is caused by the absence of vortex shedding at this frequency in the DNS and maybe vortex shedding exists in the experiment. However, this speculation has not been verified. In the present LES simulation, there is no vortex shedding as shown in Figure V-19.

For 1 kHz case, the results obtained using LES are different from the values obtained by Tam et al. [21]. For the case of 1.1 kHz, the absorption coefficient is at its maximum in our LES. The value obtained at 1.1 kHz using the viscous dissipation method is almost equal to the value obtained by Tam et al. [21] for the case of a sound source frequency of 1 kHz. However, for the case measured using the two-microphone method, the value still lower.

Figure V-24 shows the absorption coefficient for a sound pressure level equal to 150 dB.

The results obtained using the viscous dissipation method (VD-150) in this study are in good agreement with the results obtained in the experiments and in the simulation using DNS by Tam et al. [21].

On the other hand, the results obtained using the transfer function method (TMM-150) gives a higher value than the experimental value in the case of a sound source frequency of 1 and 2 kHz. The value of the absorption coefficient is lower than the experimental result in the case of 3 kHz sound source frequency.

2.2.2.2. Numerical Simulation of 2D Active Acoustic Liner with a Bias Flow

In this case, the model shown in Figure V-18 is simulated with a bias flow as a result of the mass source included in the solver and explained in Sec. II.4.2, and the mass source value is calculated so that the Mach number M=0.029 (9.86 m/s) is attained at the aperture. This value of the bias mass flow Mach number is chosen in a way to have a bias flow velocity higher than the acoustic particle velocity of the acoustic wave.

Even though the two microphone method is originally developed for stationary flow field, the absorption coefficients for the resonator with bias flow are measured using this method since the flow in the duct is considered to be very small.

At the exit of the tube, a far-field boundary condition is applied, the Mach number at the exit is set in accordance with the required bias flow velocity.

Figure V-23 and Figure V-24 show the results obtained in this case and are compared with the results of the case with no bias flow.

We notice in the case of a sound pressure level equal to 150 dB, that the value of the absorption coefficient at 1 kHz and 2 kHz, which is close the resonance frequency is of same values obtained by the transfer function method (two-microphone method) for the case with no bias flow. However, when compared with the values obtained using the viscous dissipation method as well as DNS and experiment by Tam et al. [21], a significant improvement is observed.

When the sound source frequency is equal to 3 kHz, the absorption coefficient reduces considerably compared to the case with no bias flow.

The behavior is different from what was obtained in our experimental results in the case of low sound pressure level sound source (linear regime) presented in Chapter IV.

In the case of a sound pressure level equal to 130 dB, the absorption coefficient near the resonance frequencies of 1 kHz and 1.1 kHz is reduced and it is increased for higher frequencies when compared to the case with no bias flow. Similar behavior was obtained our experimental results in the case of low sound pressure level sound source (linear regime) presented in Chapter IV.

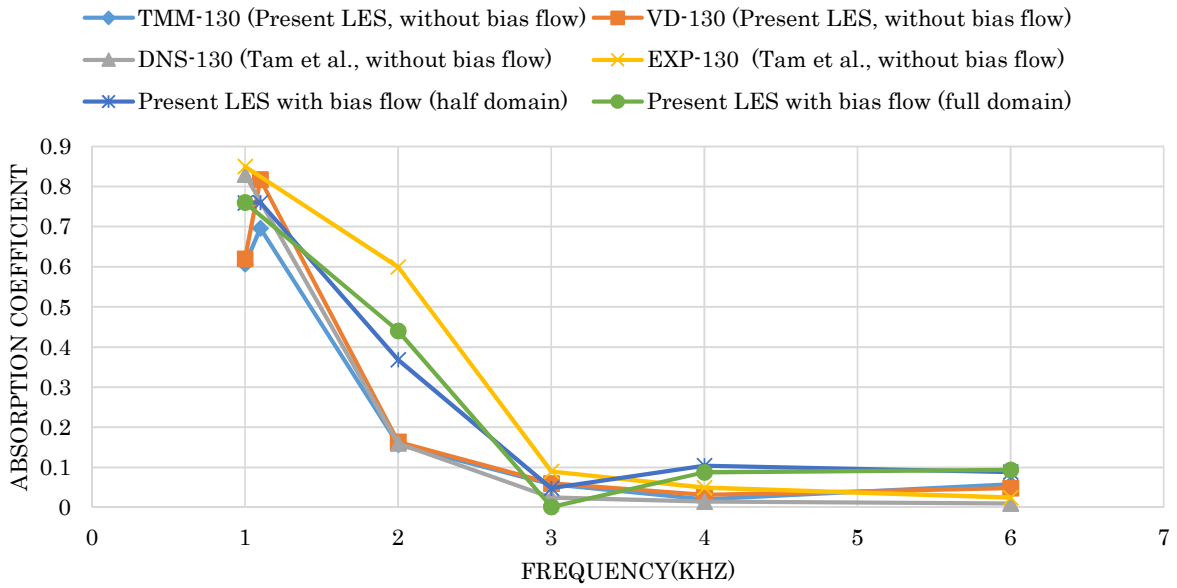

Figure V-23 Absorption coefficient: 130 dB

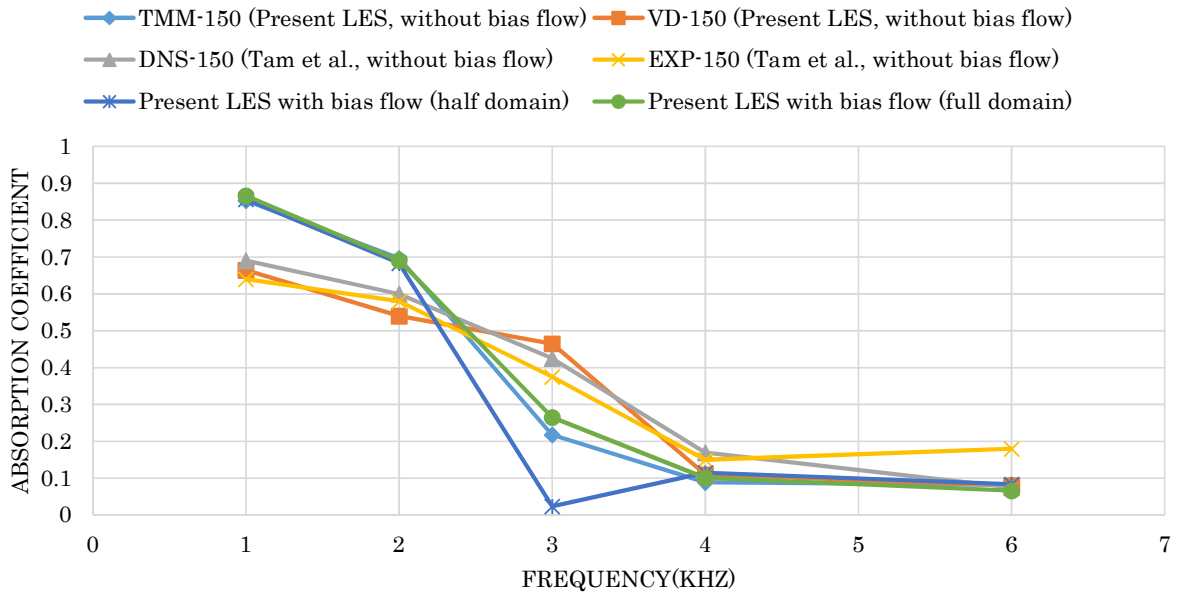

Figure V-24 Absorption coefficient: 150 dB

2.2.3. Flow field

First, the flow field is described for the case without bias, then, the effect of the introduction of a bias flow passing through the aperture of the resonator is investigated and a comparison of the flow behavior at the aperture with a conventional liner is highlighted.

As described in the textbook by Greitzer et al. [40], the incoming flow to the aperture comes from all directions and the outgoing flow goes out mainly to the axial direction, and the flow separates at the inlet. The incoming sound waves induce sinusoidal jet flows in the aperture.

2.2.3.1. Flow-field of the Conventional Acoustic Liner

Figure V-20 shows snapshots of the unsteady vorticity contour around the aperture for the case of sound pressure level of 150 dB and frequency of 1 kHz.

The flow is symmetrical with the aperture, and the vortices are generated at each side of the aperture periodically every half an acoustic wave generated in the tube. Next, these vortices are shed away from the aperture in different directions

The shed vortices take away the kinetic energy of the sound wave, and the generation of the vortex plays an important role in the sound attenuation in this high SPL incoming sound wave.

Figure V-25 shows the values of the average viscous dissipation rate $\overline{D}(x,y)$ on different blocks of the calculation domain. The highest value is obtained inside the cavity where the vortices are retained within. The viscous dissipation at the aperture is very low and thus we can confirm that most the sound absorption is attributed to the shed vortices.

Figure V-19 shows snapshots of the unsteady vorticity contour around the aperture for the case of a sound pressure level of 130 dB and a frequency of 1 kHz.

In this case, the pumping by the incoming sound wave is smaller than that for the 150 dB incoming sound wave case, and the vortex generated at the aperture remains around the aperture and the vortices are not convected further upstream or downstream, and thus no vortex shedding is observed.

The viscous dissipation of the vortex plays an important role in the sound attenuation in this low SPL incoming sound waves.

However, Tam et al. [21] obtained a flow with vortices for this case, this may explain the lower value of the absorption coefficient obtained for this case.

Figure V-26 shows the percentage of the absorption coefficient attributable to each term of the viscous dissipation function. vd1, vd2, and vd3 are the percentages for the terms Φ_1, Φ_2 and Φ_3.

For the evaluated cases shown in Figure V-26, most of the absorption is caused by the shear deformation vd3 accounting for more than 60% of the total absorption.

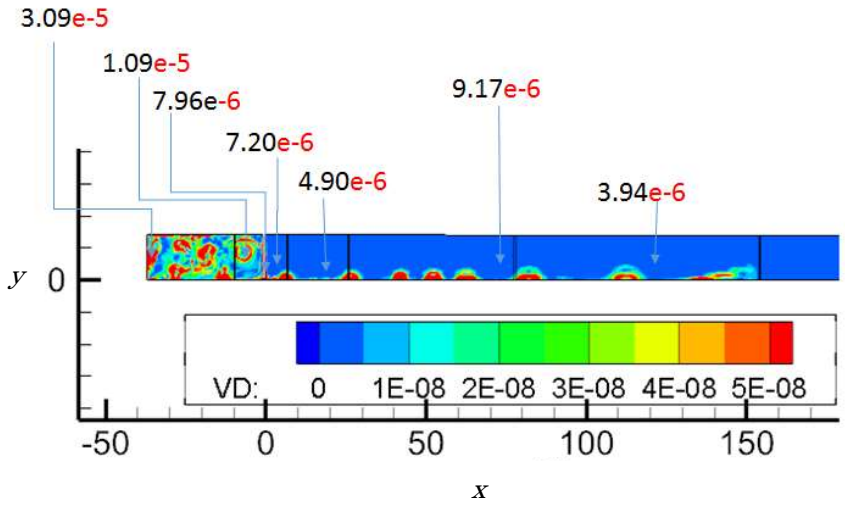

Figure V-25 Instantaneous non-dimensional viscous dissipation rate (VD): 150 dB, 1 kHz without bias flow

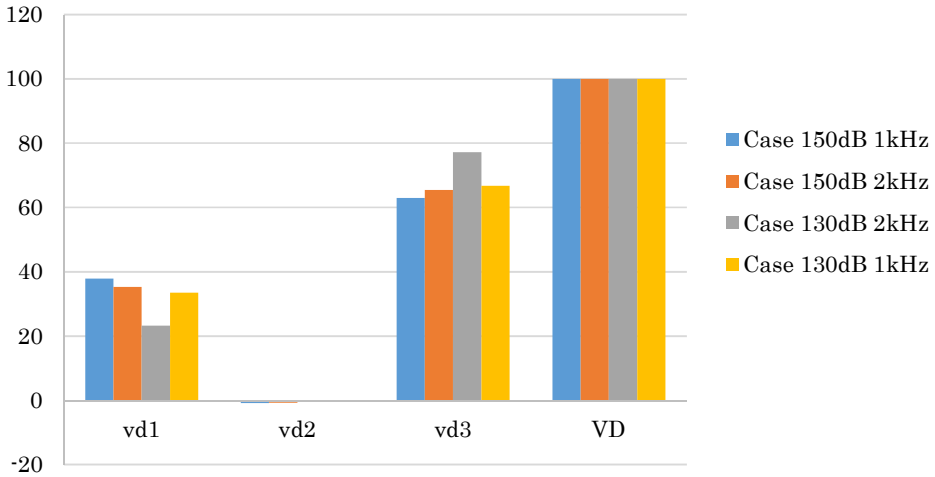

Figure V-26 Percentage of the absorption caused by each term of the viscous dissipation term, cases without bias flow

2.2.3.2. Flow-field of the Active Acoustic Liner with a Bias Flow

When the bias flow is introduced, the flow around the aperture is no longer symmetrical with respect to the $y = 0$ surface, thus only the full domain calculation is considered here.

Figure V-22 shows snapshots of the unsteady vorticity contour around the aperture for the case of a sound pressure level of 150 dB and a frequency of 1 kHz.

Fewer vortices are generated to the left side of the aperture, while, more intensive and extensive vortices are generated to the downstream direction which may take away larger energies from the incoming sound wave, compared with non-bias flow case.

The vortices on the right side of the aperture are shed with a higher velocity. This makes sense since these vortices are shed with the bias flow velocity, however, the vortex shed to the left side is shed in the inverse direction of the bias flow.

Because of the non-symmetrical behavior of the flow, the vortices are not always traveling downstream, but they stay concentrated near the aperture moving in a circular manner.

Figure V-21 shows snapshots of the unsteady vorticity contour around the aperture for the case of a sound pressure level of 130 dB and a frequency of 1 kHz with an applied bias flow.

In this case, a vortex shedding is observed from the right side of the aperture every acoustic wave generated in the tube, while no vortices are generated on the left side of the aperture.

The generated vortices due to the incoming sound wave are small and the unsteady vortex is considered to be canceled out and/or be dissipated, so that a small number of vortices are visible in the downstream of the bias flow but the dissipated vortices are visible in the wake.

Chapter 6

VI. Theoretical study of acoustic liners

1. Derivation of the wave equation and Webster's horn equation

The wave equation is based on fluid dynamics governing equations and it describes the behavior of pressure or velocity while it propagates in time and space. The wave equation is generally a 3-dimensional equation. However, it can be reduced to a 1-dimensional equation. Such a reduced equation can describe properly the sound field in the case of a duct of constant cross-sections. For duct with a variable cross-section, the 1-dimensional wave equation is inappropriate and the 3-dimensional wave equation should be used instead, this increases the complexity of the problem.

The Webster horn equation is a one-dimensional wave equation for sound waves in a rigid duct with variable cross-sections. Webster [41] presented a simplification of the 3 dimensionality problem encountered in the wave equation and reduced it to a one-dimensional problem. Fluid motion in a variable cross-section duct cannot be one dimensional, however, if the area change is varying gradually, the transverse movement of the acoustic wave can be small enough to be ignored leading to an approximate equation known as the Webster's horn equation. In this section, a review of the derivation of the Webster equation is given.

1.1. Continuity equation

The conservation of mass states that the rate of change of mass in a control volume is equal to the net change of mass flux over the control surfaces. In this section, the conservation of mass is applied in the case of variable cross-section duct as shown in Figure VI-1. This leads to Eq. (VI.1).

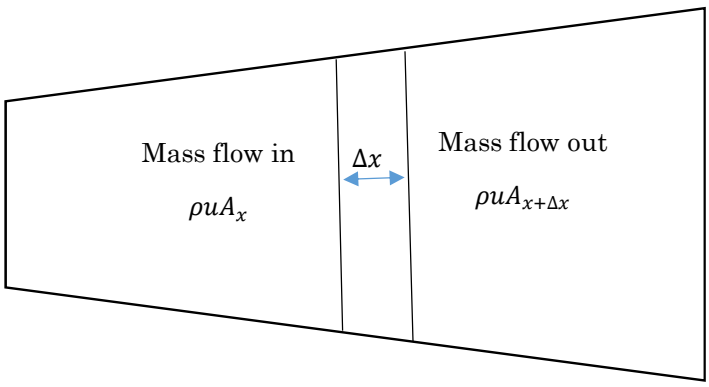

Figure VI-1 Mass flux

$$\frac{\partial}{\partial t}(\rho A \Delta x) = \rho u A|_x - \rho u A|_{x+\Delta x} \tag{VI.1}$$

Where $\frac{\partial}{\partial t}(\rho A \Delta x)$ is the rate of increase of mass inside the control volume in Figure VI-1. $\rho u A|_x$ and $\rho u A|_{x+\Delta x}$ are respectively mass flow in and mass flow out of the control volume.

Rearranging and taking the limit as $\Delta x \to 0$ results in Eq. (VI.2) which might be also rewritten as in Eq. (VI.3).

$$\frac{\partial}{\partial t}(\rho A) = \lim_{\Delta x \to 0} \frac{\rho u A|_x - \rho u A|_{x+\Delta x}}{\Delta x} = -\frac{\partial}{\partial x}(\rho u A) \tag{VI.2}$$

$$\frac{\partial}{\partial t}(\rho) + \frac{\partial}{\partial x}(\rho u) + \frac{\rho u}{A}\frac{\partial}{\partial x}(A) = 0 \tag{VI.3}$$

It is to be noted that in the case of a duct of constant cross-section the term $\frac{\rho u}{A}\frac{\partial}{\partial x}(A)$ reduces to zero leading to the well-known one dimensional continuity equation given in Eq. (VI.4).

$$\frac{\partial}{\partial t}(\rho) + \frac{\partial}{\partial x}(\rho u) = 0 \tag{VI.4}$$

1.2. Momentum equation

In this section, the momentum equations are derived in the case of variable cross-section duct as shown in Figure VI-2.

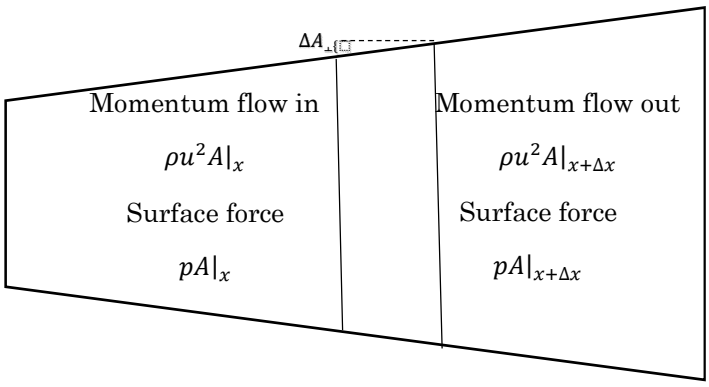

Figure VI-2 Momentum flux

The conservation of momentum states that the rate of change of momentum is equal to the sum of forces applied on the fluid element surfaces. This results in Eq. (VI.5) where

$$\frac{\partial}{\partial t}(\rho u A \Delta x) = \rho u^2 A|_x - \rho u^2 A|_{x+\Delta x} + pA|_x - pA|_{x+\Delta x} + p\Delta A_\perp|_{x+\Delta x/2} \tag{VI.5}$$

Equation (VI.5) then can be rearranged as it follows:

$$A\frac{\partial}{\partial t}(\rho u) = \frac{\rho u^2 A|_x - \rho u^2 A|_{x+\Delta x}}{\Delta x} + \frac{pA|_x - pA|_{x+\Delta x}}{\Delta x} + \frac{1}{2}\Delta A_\perp p' \tag{VI.6}$$

taking the limit as $\Delta x \to 0$ results in Eq. (VI.7)

$$A\frac{\partial}{\partial t}(\rho u) = -\frac{\partial}{\partial x}(\rho u^2 A) - A\frac{\partial}{\partial x}(p) \tag{VI.7}$$

By expanding Eq.(VI.7) and replacing $\frac{\partial}{\partial t}(\rho)$ with Eq. (VI.3), the momentum equation can be written as it follows:

$$\rho\frac{\partial}{\partial t}(u) + \mathrm{u}\frac{\partial}{\partial x}(u) + \frac{\partial}{\partial x}(p) = 0 \tag{VI.8}$$

It is to be noted that the momentum equation in the case of a duct of constant cross-section is written in the same way as in Eq. (VI.8).

1.3. Webster horn equation

To get the Webster wave equation, first, the continuity equation (Eq. (VI.3)) and momentum equation (Eq. (VI.7)) need to be linearized giving the following equations

$$\frac{\partial}{\partial t}(\rho) + \rho_0\frac{\partial}{\partial x}(u) + \frac{\rho_0 u}{A}\frac{\partial}{\partial x}(A) = 0 \tag{VI.9}$$

$$\rho_0\frac{\partial}{\partial t}(u) + \frac{\partial}{\partial x}(p) = 0 \tag{VI.10}$$

And using, in addition, the state equation

$$p = c^2 \delta\rho \tag{VI.11}$$

The linearized continuity equation written in Eq. (VI.4) when differentiated with respect to time becomes

$$\frac{1}{c_0^2}\frac{\partial^2}{\partial t^2}(p) + \rho_0 \frac{\partial^2}{\partial x \partial t}(u) + \frac{\partial}{\partial t}\left(\frac{\rho_0 u}{A}\frac{\partial}{\partial x}(A)\right) = 0 \tag{VI.12}$$

And using the linearized momentum equation, Eq. (VI.12) becomes

$$\frac{1}{c_0^2}\frac{\partial^2}{\partial t^2}(p) - \frac{\partial}{\partial x}\left(\frac{\partial}{\partial x}(p)\right) - \frac{\partial}{\partial x}(p)\frac{1}{A}\frac{\partial}{\partial x}(A) = 0 \tag{VI.13}$$

Equation (VI.13) is called Webster's horn equation and can also be written in the form of Eq. (VI.14).

$$\frac{1}{c_0^2}\frac{\partial^2 p}{\partial t^2} - \frac{1}{A}\frac{\partial}{\partial x}\left(A\frac{\partial p}{\partial x}\right) = 0 \tag{VI.14}$$

1.4. Wave equation

When the cross-section area A is assumed to be constant, Webster's horn equation reduces to the one dimensional wave equation given in Eq. (VI.15) as it follows:

$$\frac{\partial^2 p}{\partial x^2} - \frac{1}{c^2}\frac{\partial^2 p}{\partial t^2} = 0 \tag{VI.15}$$

Assuming a harmonic sound wave

$$p(x,t) = p(x)e^{i\omega t} \tag{VI.16}$$

By substituting the harmonic function into the wave equation.

$$\frac{\partial^2 p(x)}{\partial x^2}e^{i\omega t} + \frac{\omega^2}{c^2}p(x)e^{i\omega t} = 0 \tag{VI.17}$$

where $k = \frac{\omega}{c}$ is the wave number.

Dividing equation (VI.17) by $e^{i\omega t}$ gives the Helmholtz equation as follows:

$$\frac{\partial^2 p}{\partial x^2} + k^2 p = 0 \tag{VI.18}$$

1.5. Helmholtz-like equation for Webster's horn equation

Assuming a harmonic sound wave

$$p(x,t) = p(x)e^{i\omega t} \tag{VI.19}$$

By substituting this harmonic function into Webster's equation (VI.14) we get Eq. (VI.20) .

$$\frac{1}{A}\frac{\partial}{\partial x}\left(A\frac{\partial p(x)}{\partial x}\right)e^{i\omega t} + \frac{\omega^2}{c^2}p(x)e^{i\omega t} = 0 \tag{VI.20}$$

Dividing equation (VI.25) by $e^{j\omega t}$ gives the Helmholtz like equation for Webster's horn as follows:

$$\frac{1}{A}\frac{\partial}{\partial x}\left(A\frac{\partial p}{\partial x}\right) + k^2 p = 0 \tag{VI.21}$$

2. Helmholtz resonator

A Helmholtz resonator impedance is decomposed into two components, namely the impedance of the aperture and impedance of the cavity.

The total impedance of the resonator is then given by Eq. (VI.22) as follows:

$$Z_{\mathrm{t}} = Z_{\mathrm{cavity}} + Z_{\mathrm{aperture}} \tag{VI.22}$$

where the impedance of the cavity is given by Eq. (VI.23) as a function of the wave number k and the cavity depth l as follows:

$$Z_{\mathrm{cavity}} = -i\cot(kl) \tag{VI.23}$$

The impedance of the aperture is given by Eq. (VI.24) as follows:

$$Z_{\text{aperture}} = r + iX \tag{VI.24}$$

where r and X are the resistance and the reactance of the aperture, respectively.

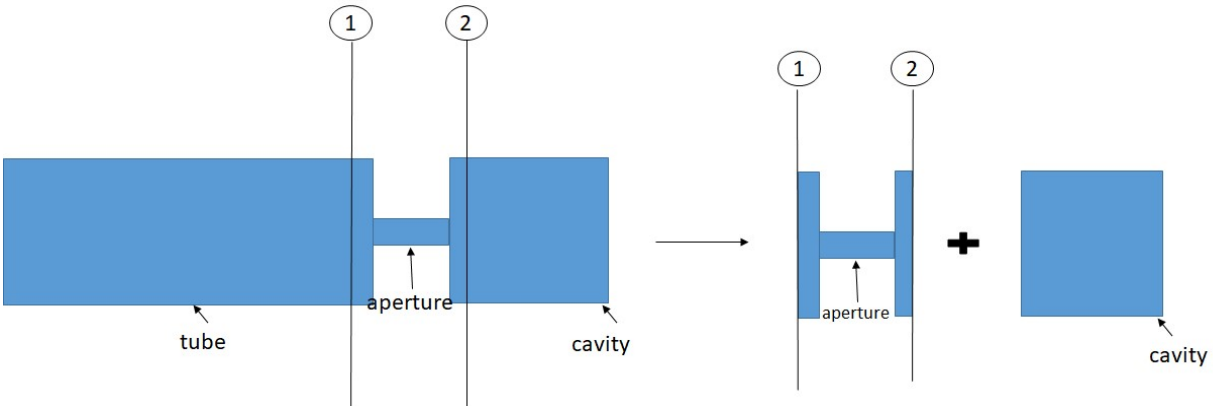

Figure VI-3 Impedance decomposition of Helmholtz resonator

3. Conventional slit resonator model

Ulf and Tor [42] proposed a theoretical model for straight slit apertures in the linear regime. The resistance of the aperture is given by Eq. (VI.25).

$$r = \frac{1}{2\rho c}\sqrt{2\mu\rho\omega}\left(4 + \frac{2h}{D}\right) \tag{VI.25}$$

where ρ denotes density, μ denotes the viscosity of air, ω denotes angular frequency, h denotes the thickness of the plate, and D denotes the width of the aperture.

Additionally, the reactance of the aperture is given by Eq. (VI.26) where δ denotes the end correction.

$$X = k(h + \delta) \tag{VI.26}$$

For a straight slit resonator, the end correction is estimated by Eq. (VI.27) as follows:

$$\delta = KD\ ;\ K = -\frac{2}{\pi}\ln\left[\sin\left(\frac{\pi}{2}\right)\right] \tag{VI.27}$$

4. Absorption of sound by a perforated screen with a backing cavity

Hughes and Dowling [23] investigated a plate with parallel slits, through which a bias flow was introduced. As a result, a theoretical model was obtained. In this section, a brief explanation of the model is given.

The theoretical model assumes an infinitely thin screen with infinitely long slits spaced regularly at a distance d and having an open area ratio ν.

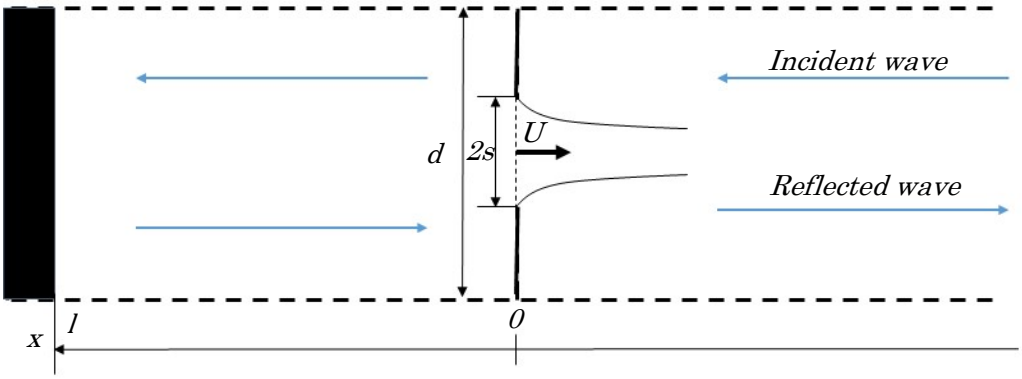

Figure VI-4 Perforated plate with bias flow and backed by a cavity

Figure VI-4 shows the resonator in the case when a bias flow is introduced through the aperture and perturbed by an acoustic field. Assuming an incident planar harmonic waves of amplitude 1.

The acoustic field inside the cavity can be formulated as it follows:

$$\tilde{p}_1(x) = Ae^{-ikx} + Be^{ikx} \tag{VI.28}$$

where A and B are the complex planar amplitudes of the right going and the left going waves inside the cavity.

The acoustic field on the right side of the perforated plate can be formulated as it follows

$$\tilde{p}_2(x) = Re^{-ikx} + e^{ikx} \tag{VI.29}$$

$$\rho c\tilde{u}_2 = Re^{-ikx} - e^{ikx} \tag{VI.30}$$

where R is the amplitude of the reflected wave and thus represents the reflection coefficient.

$$\frac{p}{\rho c u} = \frac{Re^{-ikx} + e^{ikx}}{Re^{-ikx} - e^{ikx}} = \frac{R + e^{2ikx}}{R - e^{2ikx}} \tag{VI.31}$$

At $x = 0$ the impedance Z at the perforated wall is as follows:

$$Z = \frac{R+1}{R-1} \tag{VI.32}$$

Huges and Dowling [23] found out that the impedance Z is written as follows:

$$Z = i\,\{(k/\eta) - (1/\tan kl)\} \tag{VI.33}$$

where $-i/\tan kl$ represents the impedance caused by the presence of the cavity. And $i\,k/\eta$ is the portion of the impedance accounting for the presence of the slit and the bias flow. It is written in terms of perforated plate geometry and bias flow properties as follows:

$$k/\eta = (2kd/\pi)[(\ln 2/\varphi) - \ln(\pi v)] \tag{VI.34}$$

where η is the effective compliance and φ is a function of Strouhal number and accounts for the influence of the vortex shedding.

The Strouhal number is defined as in Eq (VI.35).

$$S_t = \frac{\omega s}{U} \tag{VI.35}$$

where

ω : Angular frequency

s : half width of the aperture

U : Vorticity convection velocity

The effective compliance η is defined as follows:

$$\eta = \frac{i\rho\omega Q}{p_2 - p_1} \tag{VI.36}$$

where $p_2 - p_1$is the pressure difference across the perforated plate and Q is the volume flow rate through the aperture. Using a simplified model of the fluctuating vorticity field, Hughes and Dowling [23] got the following expression for the flow rate

$$Q = -\{\pi/(i\omega\rho_0)\}/\{i\pi/(k_1 d) - ln(\pi v) + \ln 2/\varphi(S_t)\} \tag{VI.37}$$

φ is a function of Strouhal number and accounts for the influence of the vortex shedding.

$$\varphi(S_t) = 1 - \frac{1}{S_t \ln 2} \times \left\{\frac{\pi I_0(S_t)e^{-S_t} + 2i\sinh(S_t)\,K_0(S_t)}{\pi e^{-S_t}[I_1(S_t) + I_0(S_t)/(I_0(S_t)\ln 2)] + 2i\sinh(S_t)\,[K_0(S_t)/(S_t \ln 2) - K_1(S_t)]}\right\} \tag{VI.38}$$

where I_n and K_n are modified Bessel functions of order *n*.

For a screen with a backing plate, the reflection coefficient is given by Eq. (VI.39).

$$R = \frac{2kd[(\ln 2/\varphi) - \ln(\pi v)] - (\pi/\tan(kl)) - i\pi}{2kd[(\ln 2/\varphi) - \ln(\pi v)] - (\pi/\tan(kl)) + i\pi} \tag{VI.39}$$

where i is the imaginary unit, k is the wave number, l is the cavity depth

5. Modified models based on Hughes and Dowling model

5.1. Straight aperture model

In this study since the used plate have finite thickness, and in order to account for the thickness of the aperture in the theoretical model, for a straight aperture of thickness *h*, the impedance of the aperture thickness $Z_{Str.aperture}$ is given by Eq. (VI.40) and added to the impedance Z of the thin screen obtained from Eq. (VI.39) using Eq. (VI.32). The method is similar to what was proposed by Jing and Sun [43] for a circular aperture.

$$Z_{Str.aperture} = ikh \tag{VI.40}$$

The total impedance of the perforated plate backed by a cavity is then given by Eq. (VI.41) as it follows:

$$Z_t = Z + Z_{Str.aperture}/\nu \tag{VI.41}$$

where ν is the open area ratio.

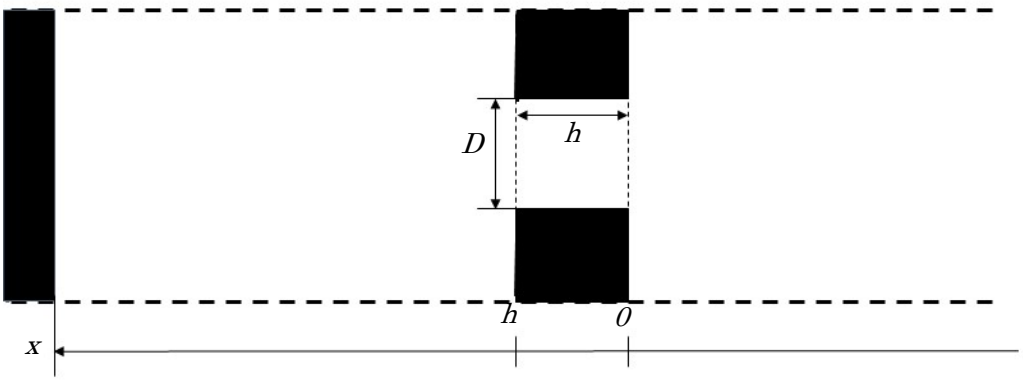

Figure VI-5 Perforated plate with straight aperture of finite thickness

5.2. Tapered aperture model

In this section, the reactance of the perforated plate with a tapered aperture is derived. The derivation is based on Webster's horn equation under the assumption of a gradually changing cross-section.

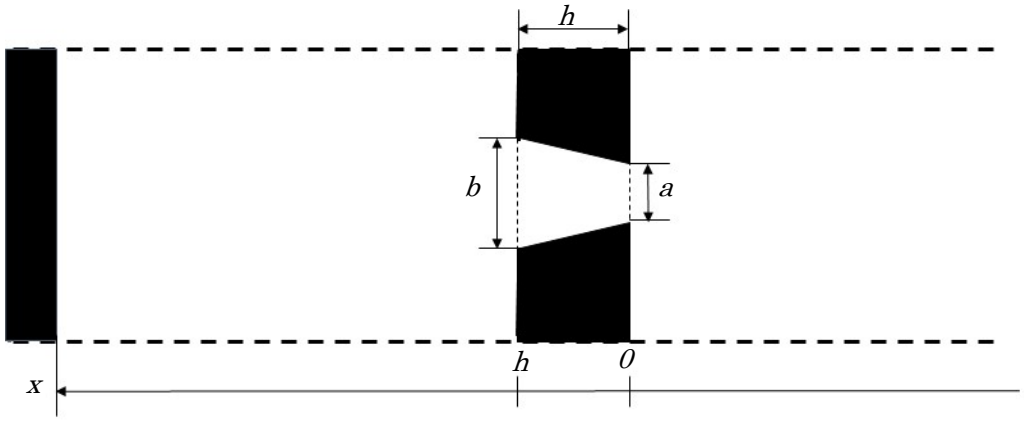

Figure VI-6 Perforated plate with tapered aperture

Figure VI-6 shows a resonator with a slit tapered aperture of trapezoidal shape with a width of b at the base and a at the top. The cross-sectional area A is function of x and it is written in Eq. (VI.42) as it follows:

$$A = (mx + a)L \tag{VI.42}$$

where L is the length of the slit, h is the thickness of the plate and m is the slope of the tapering such that $m = (b - a)/h$

Replacing the cross section in Eq. (VI.21) leads to the following equation:

$$\frac{\partial^2 p}{\partial x^2} + \frac{m}{(mx + a)}\frac{\partial p}{\partial x} + k^2 p = 0 \tag{VI.43}$$

Replacing $\alpha = mx + a$ in Eq. (VI.43) gives a differential equation of Bessel type as in Eq. (VI.44).

$$\frac{\partial^2 p}{\partial \alpha^2} + \frac{1}{\alpha}\frac{\partial p}{\partial \alpha} + \left(\frac{k}{m}\right)^2 p = 0 \tag{VI.44}$$

The general solutions for Eq. (VI.44) can be written in the form of Eq. (VI.45) as it follows:

$$p = C_1 J_0\left(\frac{\alpha k}{m}\right) + C_2 Y_0\left(\frac{\alpha k}{m}\right) \tag{VI.45}$$

Which can also be written as in Eq. (VI.46) by replacing $\alpha = mx + a$

$$p = C_1 J_0\big((mx + a)k/m\big) + C_2 Y_0\big((mx + a)k/m\big) \tag{VI.46}$$

where C_1 and are C_2 are complex constants depending on the boundary conditions. J_n and Y_n are respectively Bessel functions of the first and second kind of order n.

-Determination of the constants C_1 and are C_2

At the boundary $x = h$ the acoustic impedance is equal to the impedance of the cavity.

$$Z_b = \frac{p}{\rho c u}\Big|_{x=h} = -i\cot(kl) \tag{VI.47}$$

where u is the acoustic particle velocity.

According to the linearized momentum equation the pressure and velocity are related as given in Eq. (VI.10). Assuming a harmonic sound wave $u(x,t) = u(x)e^{i\omega t}$ and deriving with respect to time is written in the complex domain as it follows $\frac{du}{dt} = i\omega u$.

By substituting it into the linearized momentum equation (VI.10) we get the expression for the particle velocity as in Eq. (VI.48).

$$u = -\frac{1}{i\rho c k}\frac{dp}{dx} \tag{VI.48}$$

By deriving the general solution of pressure given in Eq. (VI.46) with respect to x coordinate and replace it in Eq. (VI.48) we can get the expression for the particle velocity as it follows:

$$u = \frac{1}{i\rho c}\left(C_1 J_1\left(\frac{(mx+a)k}{m}\right) + C_2 Y_1\left(\frac{(mx+a)k}{m}\right)\right) \tag{VI.49}$$

Replacing the expression of pressure and velocity in Eq. (VI.47) we get the expression of the impedance at $x = h$ as it follows:

$$Z_b = i\frac{C_1 J_0(bk/m) + C_2 Y_0(bk/m)}{\left(C_1 J_1\left(\frac{bk}{m}\right) + C_2 Y_1\left(\frac{bk}{m}\right)\right)} \tag{VI.50}$$

Dividing both the nominator and denominator with C_2 and solving for $\frac{C_1}{C_2}$ leads to Eq. (VI.51) as it follows:

$$\frac{C_1}{C_2} = \frac{iY_0\left(\frac{bk}{m}\right) - Y_1\left(\frac{bk}{m}\right)Z_b}{-iJ_0\left(\frac{bk}{m}\right) + J_1\left(\frac{bk}{m}\right)Z_b} \tag{VI.51}$$

In the same manner, the acoustic impedance at the boundary $x = 0$ is calculated as in Eq. (VI.52).

$$Z_a = \frac{p}{\rho c u}\Big|_{x=0} = i\frac{\frac{C_1}{C_2}J_0(ak/m) + Y_0(ak/m)}{\frac{C_1}{C_2}J_1\left(\frac{ak}{m}\right) + Y_1\left(\frac{ak}{m}\right)} \tag{VI.52}$$

If the aperture is considered in isolation, the impedance Z_b of the cavity will be replaced by zero and this will result in the term $\frac{C_1}{C_2}$ reducing to C as given in Eq. (VI.53).

$$C = -\frac{Y_0\left(\frac{bk}{m}\right)}{J_0\left(\frac{bk}{m}\right)} \tag{VI.53}$$

By replacing the coefficient C obtained in Eq. (VI.53) in Eq. (VI.52) we get the impedance at the inlet of the aperture as in Eq. (VI.54).

$$Z_{Tap.aperture} = i\frac{CJ_0(ak/m) + Y_0(ak/m)}{CJ_1\left(\frac{ak}{m}\right) + Y_1\left(\frac{ak}{m}\right)} \tag{VI.54}$$

5.3. Impedance model of the slit tapered aperture with bias flow

By combining the impedance derived from Hughes and Dowling's model as in Eq.(VI.33) with the reactance of the tapered aperture derived in Eq. (VI.54) we get the total impedance of the slit tapered aperture with bias flow as follows:

$$Z_{total} = Z + Z_{Tap.aperture}/\nu \tag{VI.55}$$

5.4. Theoretical model results for the slit straight aperture

In this section, Results obtained from theoretical models explained in the previous sections are compared to the results obtained by numerical simulation and also by the impedance tube experiment.

5.4.1. Straight aperture without bias flow

For the straight slit aperture, Ulf and Tor [42] proposed a theoretical model which is explained in section VI.3.

The straight aperture used in this study has a width D= 1 mm and a thickness h = 1 mm. This values are replaced in Eqs. (VI.26) and (VI.27) to obtain the impedance of the aperture, then using Eq. (VI.22) the total impedance of the resonator is obtained.

Figure VI-7 compares results of the absorption coefficients obtained experimentally, numerically, and theoretically for the straight slit aperture. Incident sound pressure level of approximately 100 dB is considered in the case without bias flow. The numerical and experimental results are in good agreement with the theoretical results, especially at frequencies higher than the resonance frequency. At around 350 Hz, a 10% difference is observed with respect to the experimental results. The theoretical results are underestimated at frequencies lower than the resonant frequency.

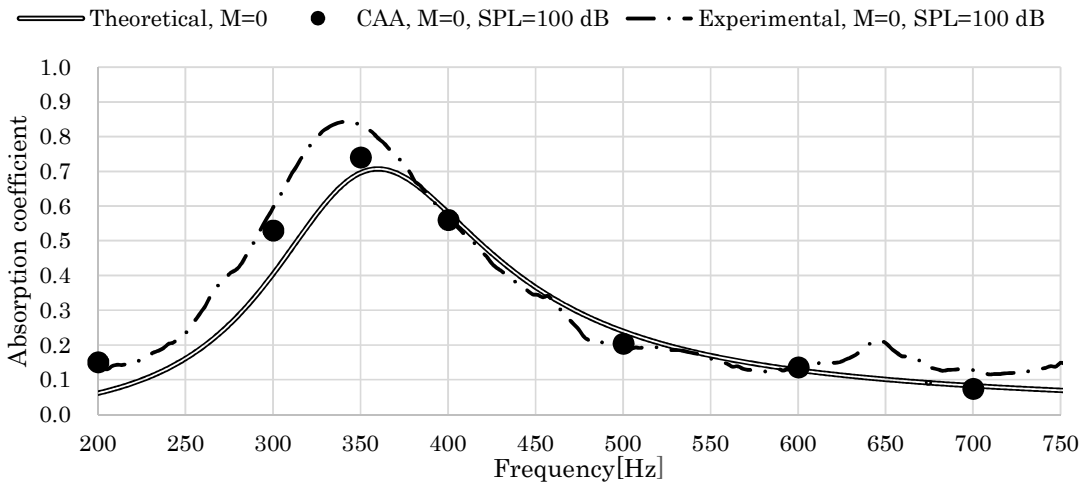

Figure VI-7 Comparison of the absorption coefficient between experiment, CAA and theoretical models results: case without bias flow

5.4.2. Straight aperture with bias flow

In the presence of a bias flow, unsteady vortex shedding from the apertures converts acoustic energy into vortical kinetic energy. Hughes and Dowling [23] approximated the vorticity convection velocity by the mean velocity at the aperture. Since in this section the perforated plate has a finite thickness, the modified theoretical model explained in section VI.1 of this chapter is used.

Using Eq. (VI.41), and replacing the Strouhal number defined as in Eq (VI.35) with a taken to be equal to half the apertures width D = 1 mm.

The comparison is made for the straight aperture and with a 10 L/min ($M = 4.85 \times 10^{-3}$), 20 L/min ($M = 9.71 \times 10^{-3}$) and 40 L/min ($M = 1.94 \times 10^{-2}$) bias flow respectively.

Figure VI-8 shows the comparison of the absorption coefficient results obtained numerically, experimentally and with the theoretical model. In this case a bias flow Mach number of $M = 4.85 \times 10^{-3}$ is applied. Very good agreement is obtained between the theoretical and the simulated CFD cases. The experimental results are also in good agreement with theoretical results, especially at frequencies higher than the resonance frequency. The theoretical results are slightly underestimated compared to experimental results for frequencies lower than the resonance frequency.

Figure VI-9 shows the absorption coefficient results in the case of an applied bias flow Mach number of $M = 9.71 \times 10^{-3}$. In this case, the theoretical results are in very good agreement with the experimental and numerical results.

Figure VI-10 shows the absorption coefficient results obtained when a bias flow Mach number of $M = 1.94 \times 10^{-2}$ is applied. The experimental and numerical results are again in good agreement with the theoretical results.

The modified theoretical model accounting for the thickness of the plate agrees very well with the CFD results of the straight aperture for all the bias flow cases considered.

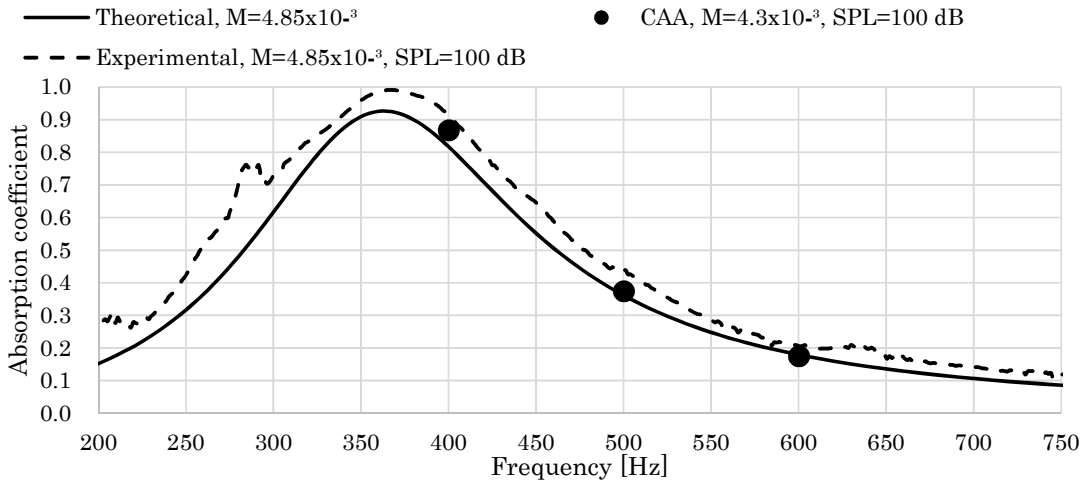

Figure VI-8 Comparison of the absorption coefficient between experiment, CAA and theoretical models results: with bias flow M=4.85× 10^{-3}

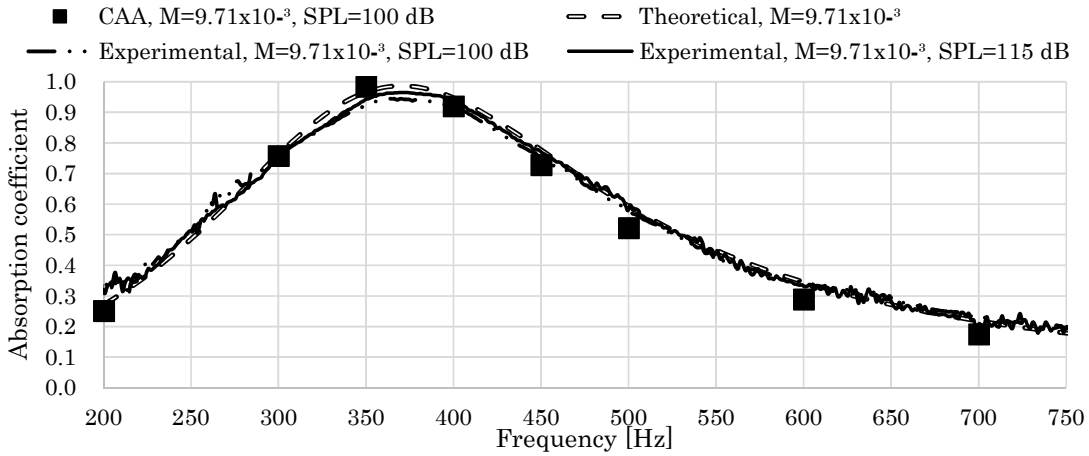

Figure VI-9 Comparison of the absorption coefficient between experiment, CAA and theoretical models results: with bias flow M=9.71× 10^{-3}

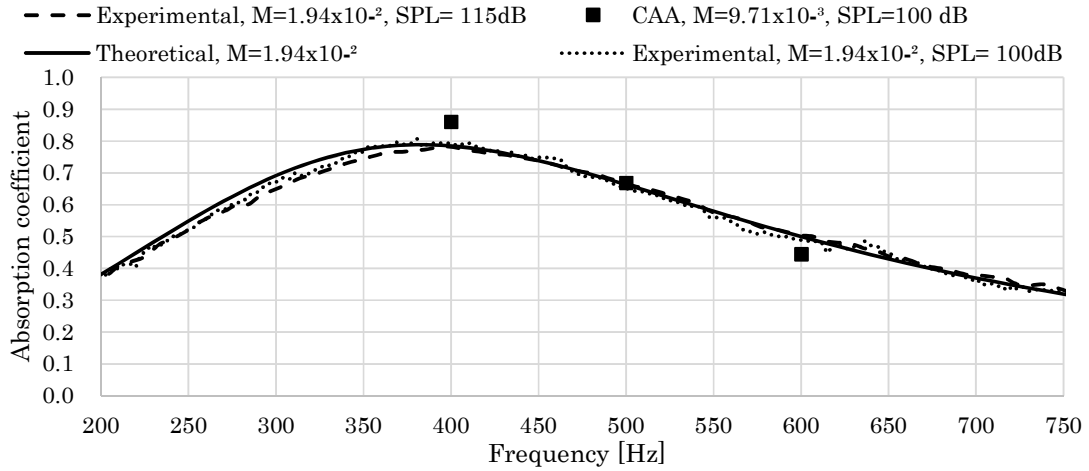

Figure VI-10 Comparison of the absorption coefficient between experiment, CAA and theoretical models results: with bias flow M=1.94× 10^{-2}

5.5. Theoretical model results for the slit tapered aperture

In this section, the comparison of the absorption coefficients between results obtained experimentally and through CFD with the prediction results from the modified theoretical model based on Hughes and Dowling [23] accounting for the thickness and shape of the perforated plate.

5.5.1. Tapered aperture without bias flow

In the case of the tapered aperture, the total impedance of the resonator is given by Eq. (VI.55). Since at the moment a model for the resistance of the tapered aperture is not yet available, the non-dimensional value of the resistance $r = 0.145$ obtained experimentally at the resonance is used. The impedance of the aperture is then obtained by adding the resistance part r to the reactance given by Eq. (VI.54) for the tapered aperture. The tapered aperture used in this study has a base $b = 7$ mm at the base and $a = 1$ mm at the top. This leads to tapering slope $m = 2$.

Figure VI-11 shows the absorption coefficient results obtained experimentally, numerically and theoretically. The results are for the case of an applied sound pressure level of 100 dB and without bias flow.

It can be seen that the experimental and numerical results are in good agreement with the theoretical results.

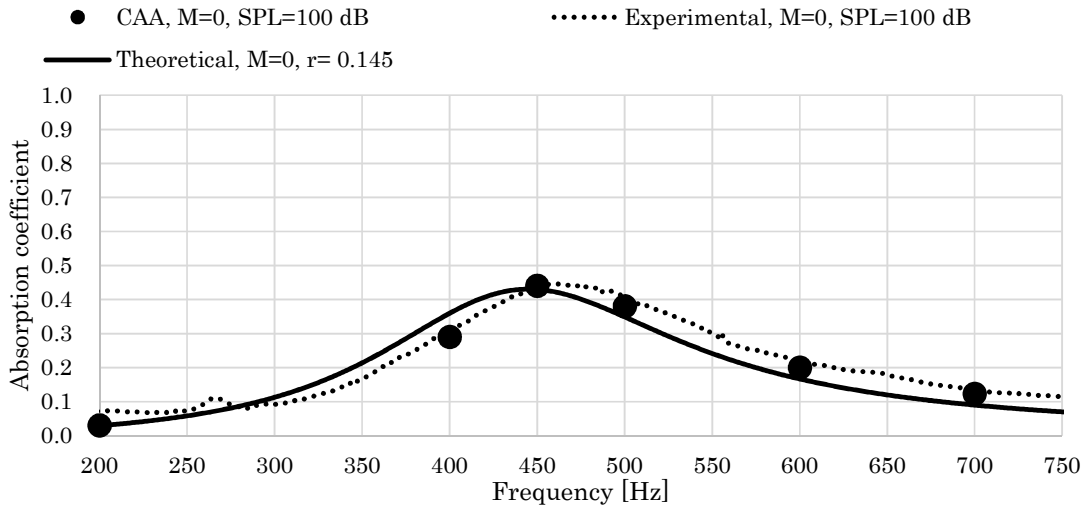

Figure VI-11 Absorption coefficient for tapered slit aperture without bias flow

5.5.2. Tapered aperture with bias flow

In this section, the modified theoretical model for tapered aperture with bias flow explained in section 5.3 of this chapter is used.

The comparison is made for the tapered aperture with a 10 L/min, 20 L/min and 40 L/min bias flow respectively.

Figure VI-12 shows the comparison of the absorption coefficient results obtained numerically, experimentally and with the theoretical model. In this case a bias flow Mach

number of $M = 4.85 \times 10^{-3}$ is applied. The numerical results and theoretical results are in good agreement. For the 100 dB case, the numerical and theoretical results are overestimated. When the sound source level is set to 115 dB, good agreement is obtained with the theoretical results.

Figure VI-13 shows the absorption coefficient results in the case of an applied bias flow Mach number of $M = 9.71 \times 10^{-3}$. In this case, the theoretical results are in good agreement with the numerical results. Slight differences between theoretical and experimental results are obtained.

Figure VI-14 shows the absorption coefficient results obtained when a bias flow Mach number of $M = 1.94 \times 10^{-2}$ is applied. Good agreement is obtained between the numerical and theoretical results. However, the theoretical results underestimate the absorption coefficient for high frequencies.

The modified theoretical model accounting for the thickness of the plate and the shape of the aperture agrees well with the CFD results of the tapered aperture for all the bias flow cases considered.

Generally, the correspondence of the absorption coefficients of theoretical, numerical and experimental results is qualitatively good.

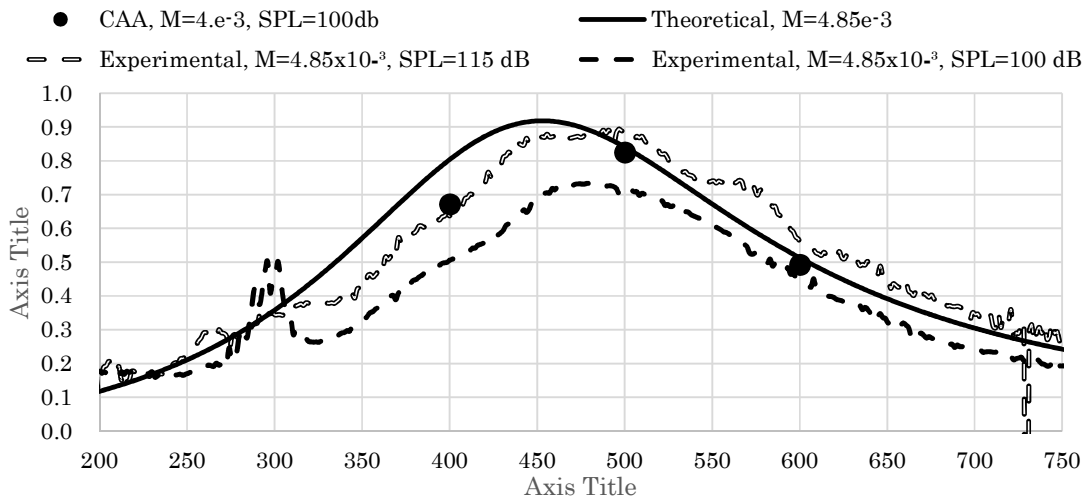

Figure VI-12 Absorption coefficient for tapered slit aperture with bias flow M=4.85× 10^{-3}

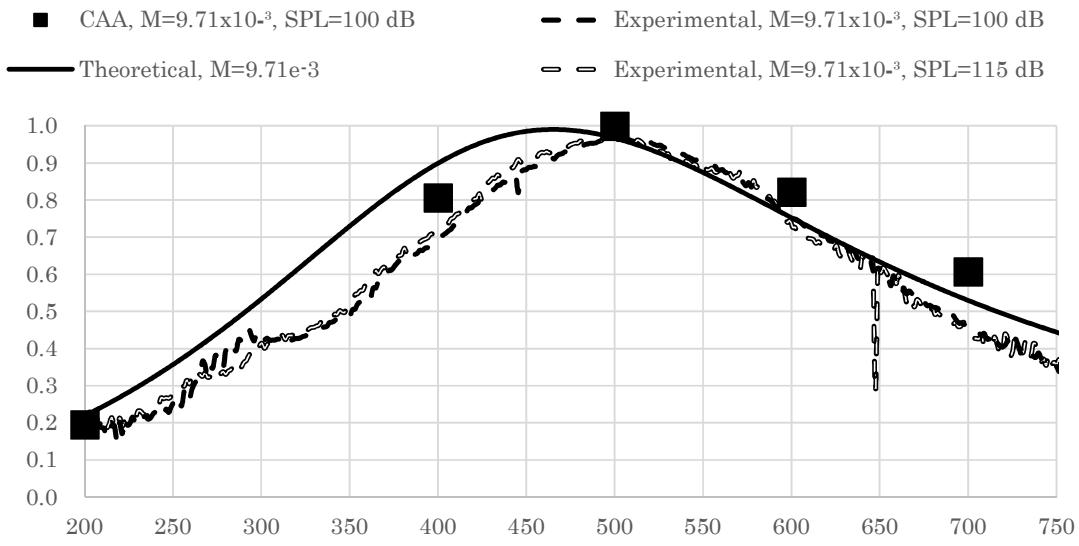

Figure VI-13 Absorption coefficient for tapered slit aperture with bias flow M=9.71× 10^{-3}

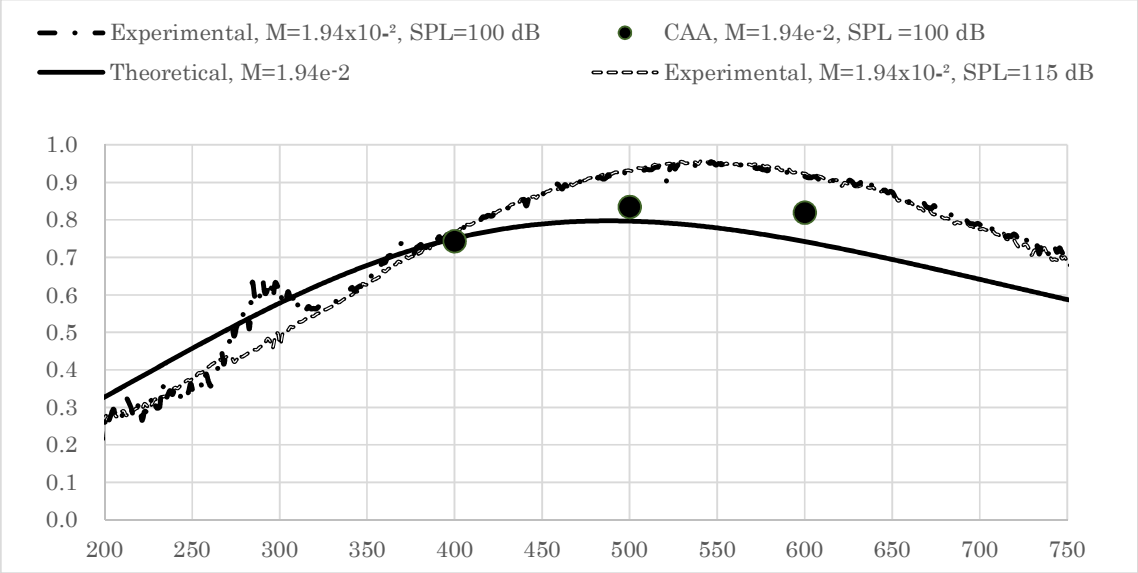

Figure VI-14 Absorption coefficient for tapered slit aperture with bias flow M=1.94× 10^{-2}

5.5.3. Effect of tapering slope m

The general solutions for Eq. (VI.44) written in Eq. (VI.45) is not defined for a zero tapering slope $m = 0$ which is a singularity for the Bessel function of second kind Y_n. Here the behavior of the solution when the tapering slope m goes toward $m \to 0$ is described.

The expression of the tapered impedance given in Eq. (VI.54) can be rewritten as follows:

$$Z_{Tap.aperture} = i\frac{-Y_0(Ar_b)J_0(Ar_a) + Y_0(Ar_a)J_0(Ar_b)}{-Y_0(Ar_b)J_1(Ar_a) + Y_1(Ar_a)J_0(Ar_b)} \tag{VI.56}$$

where $Ar_b = \frac{bk}{m}$ and $Ar_a = \frac{ak}{m}$.

When the tapering slope goes toward zero $m \to 0$, the arguments Ar_b and Ar_a go towards infinity.

The asymptotic approximations of Bessel functions of first kind $J_n(Ar)$ and second kind $Y_n(Ar)$ for large arguments ($Ar \to \infty$) are written as it follows [44]:

$$J_n(Ar) \sim \sqrt{\frac{2}{\pi A}}\cos\left(A - \frac{(2n+1)\pi}{4}\right) \tag{VI.57}$$

$$Y_n(Ar) \sim \sqrt{\frac{2}{\pi A}}\sin\left(A - \frac{(2n+1)\pi}{4}\right) \tag{VI.58}$$

By replacing Eqs. (VI.57) and (VI.58) in Eq. (VI.56), the impedance of the tapered aperture becomes as given in Eq. (VI.59).

$$Z_{Tap.aperture} = i\frac{-\sin\left(A_b - \frac{\pi}{4}\right)\cos\left(A_a - \frac{\pi}{4}\right) + \sin\left(A_a - \frac{\pi}{4}\right)\cos\left(A_b - \frac{\pi}{4}\right)}{-\sin\left(A_b - \frac{\pi}{4}\right)\cos\left(A_a - \frac{3\pi}{4}\right) + \sin\left(A_a - \frac{3\pi}{4}\right)\cos\left(A_b - \frac{\pi}{4}\right)} \tag{VI.59}$$

By using the trigonometric identities Eq. (VI.59) reduces to (Eq. 60).

$$Z_{Tap.aperture} = i\frac{\sin(A_b - A_a)}{\sin\left(A_b - A_a + \frac{\pi}{2}\right)} \tag{VI.60}$$

For $A_b \to A_a$, the difference of the arguments goes toward zero $(A_b - A_a) \to 0$. Thus Eq. (VI.60) can be rewritten as it follows:

$$Z_{Tap.aperture} = i\frac{(A_b - A_a)}{\sin\left(\frac{\pi}{2}\right)} = i(A_b - A_a) = i\frac{(b-a)k}{m} = ikh \qquad \text{(VI.61)}$$

Equation VI.61 has the same expression as the impedance of the straight aperture given in Eq. (VI.40).

Figure VI-15 shows the absorption coefficient results when a bias flow Mach number $M = 9.71 \times 10^{-3}$ obtained with the theoretical for tapered aperture at different tapering slopes m. The results are compared to the theoretical results for the straight aperture model as well as the thin plate model.

The resonance frequency has tendency to increase when the tapering slope increases. Moreover, the absorption coefficient range widens when the tapering slope m increases and becomes narrow when it reduces.

When the tapering slope goes toward zero $m \to 0$, the absorption coefficient goes toward the results of the absorption coefficient of the straight aperture model.

When the tapering slope goes toward infinity $m \to \infty$, the absorption coefficient goes toward the results of the absorption coefficient of the thin plate model by Hughes and Dowling[23].

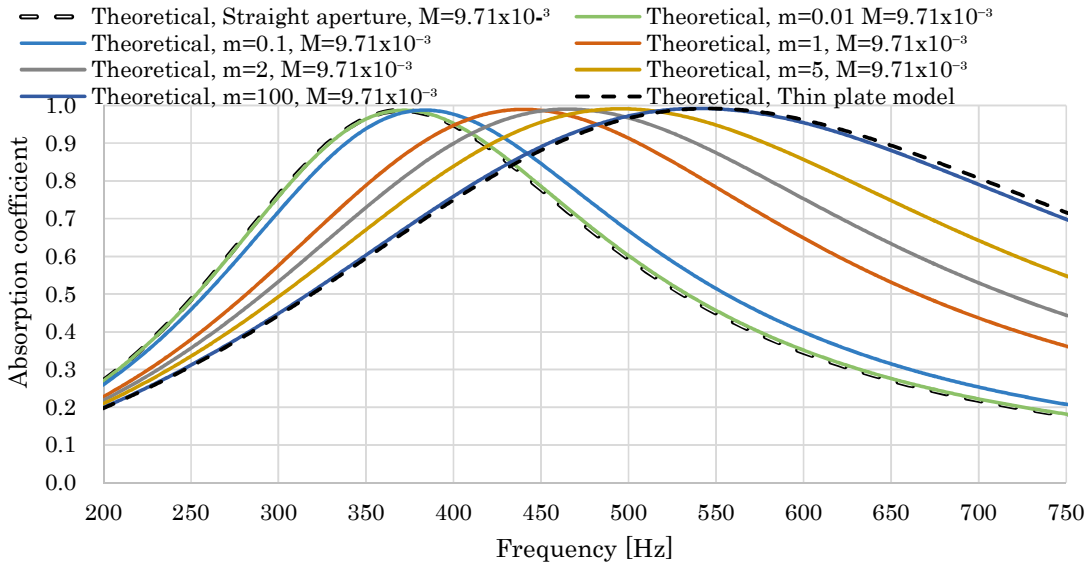

Figure VI-15 Absorption coefficient at different tapering slope

Chapter 7

VII. Conclusion

Noise emitted from airplanes is considered as a component of environment pollution, which causes annoyance and discomfort for population around airports and even health illness for people working close to airplanes, this is why regulations are trying to reduce the level of permissible noise of airplanes.

One of the major sources of noise in commercial airplane is the turbofan engine, and more specifically the fan noise consisting of broadband and tone noises. As a remedy to this problem, acoustic liners are installed on the inner side of the nacelle of the turbo-fan engines, and they consist of a perforated plate backed by hard wall, in addition to a honeycomb support in between.

Two regimes contribute to the noise reduction in acoustic liners, i.e. the developed vortices at the perforated plates for high SPL and the viscous dissipation at the walls of the aperture for low SPL. ,

In this study, experimental results of the acoustic behavior of two different slit apertures (i.e., straight and tapered apertures with and without bias flow) were obtained via an impedance tube test rig.

In the case without bias flow, straight aperture results in a narrow absorption frequency range centered around the resonant frequency. Conversely, the tapered aperture tends to exhibit a wider absorption frequency range. Additionally, the tapered aperture has a higher resonant frequency than the straight aperture.

Large eddy simulations were conducted in conditions approximately similar to that of experiments for validation purposes of the acoustic behavior of the resonators, and also to visualize the flow field around the apertures. The absorption coefficients obtained by CAA agree well with the experimental results.

The study also discusses the flow field around the apertures and effect of flow structures around the apertures on the absorption performance of the resonators.

The results indicate that the presence of vortex shedding increases the absorption coefficient. Increases in the sound pressure level intensifies the vortex shedding, thereby leading to a better absorption performance than that for lower sound pressure levels. Additionally, the introduction of a bias flow (which is a method to facilitate the vortex shedding even for lower sound pressure levels) improves the absorption performance.

A study in the case of high sound pressure level sound source excitation is also conducted and validated by the experimental results of the slit liner investigated for the case with no bias flow earlier by Tam et al. [21], and good agreement is obtained when calculating the absorption coefficients using the viscous dissipation method at the sound source pressure level of and 130 dB and 150 dB.

The acoustic performance of the liner is also investigated when a bias flow passing through the aperture is introduced. A comparison of the flow behavior at the aperture with a conventional liner shows that when the sound pressure level is equal to 130 dB, an increase in the absorption is obtained for frequencies above the resonance frequency when bias flow passing through the aperture is introduced. On the other hand, the absorption is reduced for the resonance frequency. However, when the SPL is equal to 150 dB, the absorption coefficient is higher near the resonance frequency, while for higher frequencies the absorption coefficient is lower.

The flow behavior for the conventional acoustic liner is periodic in time with an observable pattern for vortices generation, and the flow is also symmetric with respect to the surface $y = 0$, while for the liner with bias flow, the behavior is not symmetric anymore and the flow is highly disturbed and random with no observable pattern.

The theoretical model by Hughes is modified in order to account for perforated plate thickness as well as the shape of the aperture. The results obtained are in good agreement with the results obtained experimentally and numerically for the tapered aperture case.

Bibliography

[1] EASA, "European Aviation Environmental Report," 2016.

[2] Secretariat, "Aircraft noise certification and new ICAO noise standards," ICAO Environmental Report, 2013.

[3] R. Sugimoto, J. Astley, and P. Murray, "Low frequency liners for turbofan engines," *International Congress On Acoustics*, 2010.

[4] L. Leylekian and M. L. P. Lempereur, "An Overview of Aircraft Noise Reduction Technologies," *Onera AerospaceLab Journal*, vol. 7.

[5] G. H. Markstein, H. Guenoche, and A. A. Putnam, "Nonsteady flame propagation.," *AGARDograph*, vol. 75, 1964.

[6] C. J. Goy, S. R. James, and S. Rea, "Monitoring Combustion Instabilities: E.ON UK's Experience," *Progress on Astronautics and Aeronautics*, vol. 210, pp. 163–175, 2005.

[7] M. Azimi, F. Ommi, and N. Jamshidi, "Using acoustic liner for fan noise reduction in modern turbofan engines," *International Journal of Aeronautical and Space Sciences*, 2014.

[8] F. Liu, S. B. Horowitz, T. Nishida, and L. Cattafesta, "A Tunable Electromechanical Helmholtz Resonator," *Ph.D. Thesis, University of Florid*, 2007.

[9] K. Wada and T. Ishii, "Acoustic Absorption of Perforated Plates with Fine Jets: Experimental Results and Analytical Models," *Proceedings of 4th International Conference on Jets, Wakes and Separated Flows*, 2013.

[10] M. S. Howe, *Acoustics and Aerodynamic Sound*. Cambridge University Press, 2014.

[11] M. S. Howe, "Attenuation of sound in a low Mach number nozzle flow," *Journal of Fluid Mechanics*, vol. 91, pp. 209–229, 1979.

[12] D. W. Bechert, "Sound Absorption Caused by Vorticity Shedding, Demonstrated with a Jet Flow," *Journal of Sound and Vibration*, vol. 70(3), pp. 389–405, 1980.

[13] I. J. Hughes and A. P. Dowling, "The absorption of sound by perforated linings," *Journal of Fluid Mechanics*, vol. 218, pp. 299–335, 1990.

[14] C. Lahiri, L. Enghardt, F. Bake, S. Sadig, and M. Gerendas, "Establishment of a high-quality database for the modelling of perforated liners," *Journal of Engineering for Gas Turbines and Power*, vol. 133(9):091503, 2011.

[15] D. Zhao and X. Y. Li, "A review of acoustic dampers applied to combustion chambers in aerospace industry," *Progress in Aerospace Science*, vol. 74, pp. 114–130, 2015.

[16] S. Mendez and J. D. Eldredge, "Acoustic modeling of perforated plates with bias flow for large-eddy simulations," *Journal of Computational Physics*, vol. 228, no. 13, pp. 4757–4772, 2009.

[17] C. Ji and D. Zhao, "Lattice Boltzmann simulation of sound absorption of an in-duct orifice," in *Proceedings of Meetings on Acoustics ICA2013*, 2013, vol. 19, no. 1, p. 030015.

[18] J. Roche, L. Leylekian, G. Delattre, and F. Vuillot, "Aircraft Fan Noise Absorption: DNS of the Acoustic Dissipation of Resonant Liners," *15th AIAA/CEAS Aeroacoustics Conference*, 2009.

[19] C. K. W. Tam, H. Ju, M. G. Jones, W. R. Watson, and T. L. Parrott, "A computational and experimental study of slit resonators," *Journal of Sound and Vibration*, vol. 284, no. 3–5, pp. 947–984, 2005.

[20] Q. Zhang and D. J. Bodony, "Numerical Simulation of Two-Dimensional Acoustic Liners with High-Speed Grazing Flow," *AIAA Journal*, vol. 49(2), 2011.

[21] C. K. W. Tam, K. A. Kurbatskii, K. K. Ahuja, and J. R. J. Gaeta, "A Numerical and Experimental Investigation of the Dissipation Mechanisms of Resonant Acoustic Liners," *Journal of Sound and Vibration*, vol. 245(3), pp. 545–557, 2001.
[22] T. Luong, M. S. Howe, and R. S. McGowan, "On the Rayleigh conductivity of a bias-flow aperture," *Journal of Fluids and Structures*, vol. 21, no. 8, pp. 769–778, 2005.
[23] A. P. Dowling and I. J. Hughes, "Sound absorption by a screen with a regular array of slits," *Journal of Sound and Vibration*, vol. 156, no. 3, pp. 387–405, 1992.
[24] H. Kobayashi, "On a Class of Pade Finite Volume Methods," *Journal of Computational Physics*, vol. 156, pp. 137–180, 1999.
[25] J. Blazek, *COMPUTATIONAL FLUID DYNAMICS Principles and Applications*. Elsevier, 2015.
[26] S. Hickel, C. P. Egerer, and J. Larsson, "Subgrid-scale modeling for implicit large eddy simulation of compressible flows and shock-turbulence interaction," *Physics of fluid*, vol. 26, 2014.
[27] F. F. Grinstein, L. G. Margolin, and W. J. Rider, "Implicit Large Eddy Simulation-Computing Turbulent Fluid Dynamics," *Cambridge University Press*, 2007.
[28] J. Smagorinsky, "General circulation experiments with the primitive equations," *Monthly Weather Review*, 1963.
[29] B. Vreman, B. Geurts, and H. Kuerten, "Subgrid-modeling in LES of Compressible Flow," *Applied scientific researchApplied Scientific Research*, vol. 54(3), pp. 191–203, 1995.
[30] S. Enomoto, S. Nozaki, T. Imamura, and K. Yamamoto, "Large-Eddy Simulation of Jet Noise using Multi-block Structured Grid," *International Gas Turbine Congress*, 2007.
[31] J. W. Deardoff, "The use of subgrid transport equations in a three-dimensional model of atmospheric turbulence," *ASME Fluid Engineering Journal*, vol. 95(3), pp. 429–438, 1973.
[32] P. A. Nelson and S. J. Elliott, *Active Control of sound*. Academic Press, 1993.
[33] M. Wolkesson, "Evaluation of impedance tube methods- A two microphone in-situ method for road surfaces and the three microphone transfer function method for porous materials," Masters Thesis, Chalmers University of Technology, 2013.
[34] 10534-2 ISO, "Acoustics — Determination of sound absorption coefficient and impedance in impedance tubes — Part 2: Transfer-function method," ISO, 1998.
[35] *Tecplot 360 Software, "Scripting Guide," 2015.* .
[36] S. K. Tang, "On Helmholtz resonators with tapered necks," *Journal of Sound and Vibration*, vol. 279, pp. 1085–1096, 2005.
[37] K. Wada, "INTERNATIONAL CONFERENCE ON JETS, WAKES AND SEPARATED FLOWS." .
[38] Y. Tanaka, N. Yamasaki, Y. Inokuchi, and T. Ishii, "Effects of Aperture Geometry on Impedance of Active Acoustic Liners," *Proceedings of International Gas Turbine Conference*, vol. ISBN978–4–89111–008–6, pp. 1052–1058, 2015.
[39] C. K. W. Tam, H. Ju, and B. E. Walker, "Numerical Simulation of a Slit Resonator in a Grazing Flow under Acoustic Excitation," *Journal of Sound and Vibration*, vol. 313, pp. 449–471, 2008.
[40] E. M. Greitzer, C. S. Tan, and M. B. Graf, *Internal Flow-Concepts and Applications*. Cambridge University Press, pp. 94-103., 2004.
[41] A. G. Webster, "Acoustical Impedance and the theory of Horns and of the Phonograph," *Proceedings of the National Academy of Sciences*, pp. 275–282, 1919.
[42] R. K. Ulf and E. Tor, "On the design of resonant absorbers using a slotted plate," *Applied Acoustics Journal*, vol. 43, pp. 39–48, 1994.
[43] X. Jing and X. Sun, "Effect of plate thickness on impedance of perforated plates with bias flow," *AIAA Journal*, vol. 38, no. 9, pp. 1573–1578, 2000.

[44] M. Abramowitz and I. A. stegun, *Handbook of Mathematical Functions With Formulas, Graphs, and Mathematical Tables*. Dover Publications, 1972.

Appendix A: Compact schemes in upacs-LES

A1. The Burgers equation

The Burgers equation is frequently used for the basic test of numerical schemes. Although the Burgers equation is a scalar equation, it has basic elements such as the non-linear convective term, diffusion term, and time-dependent term. The numerical schemes that are used in the upacs-LES code are tested here by using the Burgers equation. The purpose is as follows:

- any unphysical disturbances are observed when a wave passes the block boundary? (In many numerical codes that are based on the compact scheme, this problem is commonly observed.)
- Does an implicit time integration work fine? (In upacs-LES code, the second order backward Euler implicit time integration with MFGS, Matrix-Free Gauss Seidel, method works only with small CFL numbers such as 1.1 or 1.2, or the solution will diverge.)
- Do the compact interpolation, difference, and filtering works with non-uniform grid correctly? (In upacs-LES code, only the compact schemes for uniform grid spacing are officially supported.)

The Burgers equation can be written as [1]

$$\frac{\partial u}{\partial t} + u\frac{\partial u}{\partial x} = \nu\frac{\partial^2 u}{\partial x^2} \tag{1}$$

When the velocity u, length x, and time t are scaled by u_∞, L, and L/u_∞, respectively, and the Reynolds number $\mathrm{Re} = u_\infty L/\nu_\infty$ is introduced, the Eq. (2) can be non-dimensionalized as

$$\frac{\partial u^*}{\partial t^*} + u^*\frac{\partial u^*}{\partial x^*} = \frac{1}{\mathrm{Re}}\nu^*\frac{\partial^2 u^*}{\partial x^{*2}} \tag{2}$$

The superscript $*$ denotes the non-dimensional variable. Let us assume that the kinematic viscosity ν is uniform in space, then $\nu^* = \nu/\nu_\infty = 1$. We omit the superscript $*$ hereafter for the simplicity. Then, the Eq. (2) becomes

$$\frac{\partial u}{\partial t} + u\frac{\partial u}{\partial x} = \frac{1}{\mathrm{Re}}\frac{\partial^2 u}{\partial x^2} \tag{3}$$

By expressing the convective and viscous fluxes as

$$\begin{aligned} E_\mathrm{c}(u) &= \frac{u^2}{2} \\ E_\mathrm{v}(u) &= -\frac{1}{\mathrm{Re}}\frac{\partial u}{\partial x} \end{aligned} \tag{4}$$

We obtain the governing equation in the strong conservation form as

$$\frac{\partial u}{\partial t} + \frac{\partial E_\mathrm{c}}{\partial x} + \frac{\partial E_\mathrm{v}}{\partial x} = 0 \tag{5}$$

or in another expression,

$$\frac{\partial u}{\partial t} = -R(u), \qquad R(u) = \frac{\partial}{\partial x}[E_{\mathrm{c}}(u) + E_{\mathrm{v}}(u)] \tag{6}$$

Let us discretize Eq. (6) in a finite volume manner. To do so, Eq. (5) is rewritten in a control-volume form as

$$\frac{\partial}{\partial t}\int u\mathrm{d}V + \int (E_{\mathrm{c}} + E_{\mathrm{v}})\mathrm{d}S = 0 \tag{7}$$

where V and S denote the volume and area of the control volume, respectively. We are now considering one dimensional problem and in this case V and S denote the area and length of the control volume. The Eq. (7) can be integrated in time, for example, by the first-order Euler explicit scheme (implicit time integration is explained in Section 5) as

$$u^{n+1} = u^n - \frac{\Delta t}{V} R(u^n) \tag{8}$$

where superscript n and n+1 indicate the current and next time level, and Δt is the time step of the numerical integration. The convective and viscous terms can be discretized in a finite volume manner as

$$\begin{aligned} \left.\frac{\partial E_{\mathrm{c}}}{\partial x}\right|_i &= \left[E_{\mathrm{c}_{i+\frac{1}{2}}} S_{i+\frac{1}{2}} - E_{\mathrm{c}_{i-\frac{1}{2}}} S_{i+\frac{1}{2}}\right] \\ \left.\frac{\partial E_{\mathrm{v}}}{\partial x}\right|_i &= \left[E_{\mathrm{v}_{i+\frac{1}{2}}} S_{i+\frac{1}{2}} - E_{\mathrm{v}_{i-\frac{1}{2}}} S_{i+\frac{1}{2}}\right] \end{aligned} \tag{9}$$

where i is the index for cell-center and $i \pm 1/2$ are the indices for cell-interfaces surrounding the cell-center i. When there are no area changes in the x direction, Eqs. (8) and (9) reduce to a finite difference formulation of

$$u^{n+1} = u^n - \Delta t \frac{1}{\Delta x}\left(\left[E_{\mathrm{c}_{i+\frac{1}{2}}} - E_{\mathrm{c}_{i-\frac{1}{2}}}\right] + \left[E_{\mathrm{v}_{i+\frac{1}{2}}} - E_{\mathrm{v}_{i-\frac{1}{2}}}\right]\right) \tag{10}$$

where $\Delta x = V/S$ is the length between the cell interfaces $i \pm 1/2$. Note that Δx can be changeable in the x direction and is not necessarily uniform.

The unknown values of $E_{\mathrm{c}_{i\pm1/2}}$ at the cell-interface can be obtained from the known values of u_i at the cell-center by using the compact interpolation formula. On the other hand, the viscous term $E_{\mathrm{v}_{i\pm1/2}}$ includes the derivative of u, which should be evaluated by using the compact difference formula. These compact formulas will be explained in detail in the following sections.

The stability of the numerical schemes of this kind of problem can be approximately judged by the Courant number C and the diffusion number D, which are defined as

$$C \equiv \frac{u\Delta t}{\Delta x}, \qquad D \equiv \frac{\nu \Delta t}{(\Delta x)^2}$$

with the usual criterion of $C \leq 1$ and $D \leq 1/2$ for the explicit schemes, which can be written for the time step Δt as[1]

$$\Delta t \leq \min\left(\frac{\Delta x}{u}, \frac{(\Delta x)^2}{2\nu}\right)$$

In the non-dimensional formulation with $\Delta x = 1,\ u = 1,\ \nu = 1$, the criterion stipulates that the non-dimensional time step should be $\Delta t \leq 0.5$ for stable calculation of the explicit time integration.

A usual compact scheme cannot handle the discontinuities such as a shock wave. Therefore, we take a convection problem that has small non-linearity as our test problem here. That is, the initial condition is given by

$$u(x) = 1 + \varepsilon \sin(kx)\ \ (\varepsilon = 0.01, 0 \leq kx \leq 2\pi) \tag{11}$$

This problem produces a shock wave when ε is large as 0.1, as the initial wave propagates downstream.

A2. Compact interpolation for convective terms

The 6th-order implicit compact interpolation formula is given by

$$\alpha_{\mathrm{i6}}\hat{f}_{i-\frac{1}{2}} + \hat{f}_{i+\frac{1}{2}} + \alpha_{\mathrm{i6}}\hat{f}_{i+\frac{3}{2}} = a_{\mathrm{ii6}}\left(\bar{f}_i + \bar{f}_{i+1}\right) + b_{\mathrm{ii6}}\left(\bar{f}_{i-1} + \bar{f}_{i+2}\right) \tag{12}$$

(169)[2]

$$\alpha_{\mathrm{i6}} = \frac{1}{3}, \qquad a_{\mathrm{ii6}} = \frac{1}{2}\,\frac{29}{18}, \qquad b_{\mathrm{ii6}} = \frac{1}{2}\,\frac{1}{18}$$

(4)[3]

TABLE I[3]

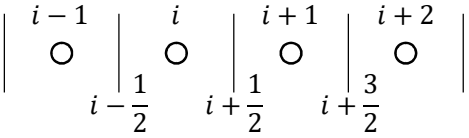

where $\bar{f}$ denotes the known values at the cell-center, which is the averaged value in a cell in the case of finite-volume formulation, and $\hat{f}$ denotes the unknown values at the cell-interface. The 8th-order explicit interpolation formula is given by

$$\hat{f}_{i+\frac{1}{2}} = a_{\mathrm{ib8}}\left(\bar{f}_i + \bar{f}_{i+1}\right) + b_{\mathrm{ib8}}\left(\bar{f}_{i-1} + \bar{f}_{i+2}\right) + c_{\mathrm{ib8}}\left(\bar{f}_{i-2} + \bar{f}_{i+3}\right) + d_{\mathrm{ib8}}\left(\bar{f}_{i-3} + \bar{f}_{i+4}\right) \tag{13}$$

(169)[2]

$$a_{\mathrm{ib8}} = \frac{1}{2}\,\frac{533}{420}, \qquad b_{\mathrm{ib8}} = -\frac{1}{2}\,\frac{139}{420}, \qquad c_{\mathrm{ib8}} = \frac{1}{2}\,\frac{29}{420}, \qquad d_{\mathrm{ib8}} = -\frac{1}{2}\,\frac{1}{140}$$

TABLE II[3]

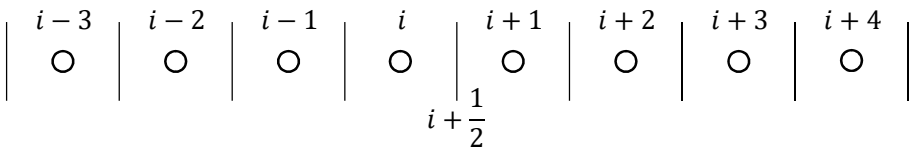

At the left hand side boundary, the 8th order explicit formula is

$$\hat{f}_{-\frac{1}{2}} = a_{\mathrm{ib8}}\left(\bar{f}_{-1} + \bar{f}_0\right) + b_{\mathrm{ib8}}\left(\bar{f}_{-2} + \bar{f}_1\right) + c_{\mathrm{ib8}}\left(\bar{f}_{-3} + \bar{f}_2\right) + d_{\mathrm{ib8}}\left(\bar{f}_{-4} + \bar{f}_3\right) \tag{14}$$

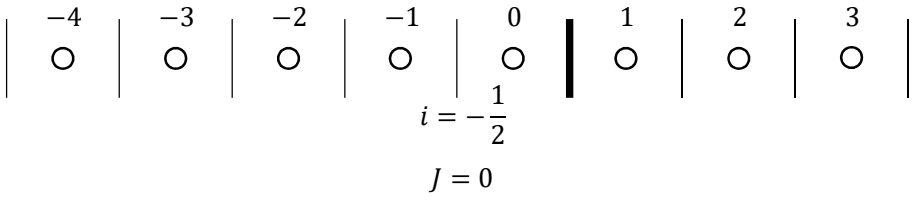

At the right hand side boundary, the 8th order explicit formula is

$$\hat{f}_{N+\frac{1}{2}} = a_{\mathrm{ib8}}\left(\bar{f}_N + \bar{f}_{N+1}\right) + b_{\mathrm{ib8}}\left(\bar{f}_{N-1} + \bar{f}_{N+2}\right) + c_{\mathrm{ib8}}\left(\bar{f}_{N-2} + \bar{f}_{N+3}\right) + d_{\mathrm{ib8}}\left(\bar{f}_{N-3} + \bar{f}_{N+4}\right) \tag{15}$$

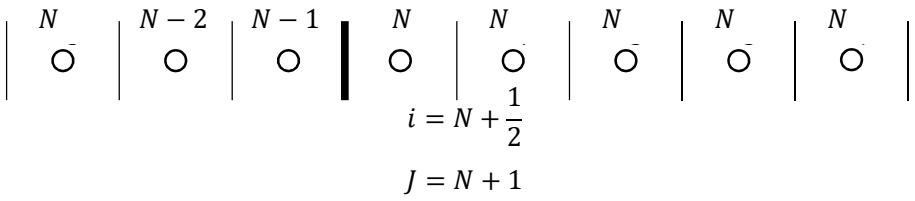

The resulting linear algebraic equation is expressed by using the cell-center index i as

$$\begin{bmatrix} 1 & \alpha & & & \\ \alpha & 1 & \alpha & & \\ & \ddots & \ddots & \ddots & \\ & & \alpha & 1 & \alpha \\ & & & \alpha & 1 \end{bmatrix} \begin{bmatrix} \hat{f}_{\frac{1}{2}} \\ \hat{f}_{\frac{3}{2}} \\ \vdots \\ \hat{f}_{N-\frac{3}{2}} \\ \hat{f}_{N-\frac{1}{2}} \end{bmatrix} = \begin{bmatrix} a\left(\bar{f}_0 + \bar{f}_1\right) + b\left(\bar{f}_{-1} + \bar{f}_2\right) \\ a\left(\bar{f}_1 + \bar{f}_2\right) + b\left(\bar{f}_0 + \bar{f}_3\right) \\ \vdots \\ a\left(\bar{f}_{N-2} + \bar{f}_{N-1}\right) + b\left(\bar{f}_{N-3} + \bar{f}_N\right) \\ a\left(\bar{f}_{N-1} + \bar{f}_N\right) + b\left(\bar{f}_{N-2} + \bar{f}_{N+1}\right) \end{bmatrix} - \alpha \begin{bmatrix} \hat{f}_{-\frac{1}{2}} \\ 0 \\ \\ 0 \\ \hat{f}_{N+\frac{1}{2}} \end{bmatrix} \tag{16}$$

and is expressed by using the cell-interface index J as

$$\begin{bmatrix} 1 & \alpha & & & \\ \alpha & 1 & \alpha & & \\ & \ddots & \ddots & \ddots & \\ & & \alpha & 1 & \alpha \\ & & & \alpha & 1 \end{bmatrix} \begin{bmatrix} \hat{f}_{J=1} \\ \hat{f}_{J=2} \\ \vdots \\ \hat{f}_{J=N-1} \\ \hat{f}_{J=N} \end{bmatrix} = \begin{bmatrix} a\left(\bar{f}_{i=0} + \bar{f}_1\right) + b\left(\bar{f}_{-1} + \bar{f}_2\right) \\ a\left(\bar{f}_{i=1} + \bar{f}_2\right) + b\left(\bar{f}_0 + \bar{f}_3\right) \\ \vdots \\ a\left(\bar{f}_{i=N-2} + \bar{f}_{N-1}\right) + b\left(\bar{f}_{N-3} + \bar{f}_N\right) \\ a\left(\bar{f}_{i=N-1} + \bar{f}_N\right) + b\left(\bar{f}_{N-2} + \bar{f}_{N+1}\right) \end{bmatrix} - \alpha \begin{bmatrix} \hat{f}_{J=0} \\ 0 \\ \\ 0 \\ \hat{f}_{J=N+1} \end{bmatrix}$$

(17)

The convective term can be discretized in a finite volume manner as

$$\left.\frac{\partial E_{\mathrm{c}}}{\partial x}\right|_i = \left[\hat{f}_{i+\frac{1}{2}} S_{i+\frac{1}{2}} - \hat{f}_{i-\frac{1}{2}} S_{i+\frac{1}{2}}\right] = \left[\hat{f}_J A_J - \hat{f}_{J-1} A_{J-1}\right] \tag{18}$$

(3)[3]

where $\hat{f} = E_{\mathrm{c}}$ in this case.

The interpolation formula in this section can only be applied to the uniform grid spacing, because the coefficients α and a, b, c, d are determined so that they fulfill the matching conditions of the terms in the Tayler expansion of both sides of the Eq. (12), and in the Tayler expansion the grid spacing are assumed to be uniform.

A3. Compact difference for viscous terms

The viscous term can be discretized in a finite volume manner as

$$(\text{viscous term})_i = \left[f'_{i+\frac{1}{2}} S_{i+\frac{1}{2}} - f'_{i-\frac{1}{2}} S_{i+\frac{1}{2}}\right] = \left[f'_J A_J - f'_{J-1} A_{J-1}\right] \tag{19}$$

(130)[2]

where f' is the first derivative of f that is evaluated at the cell-interface, which can be obtained by using the compact difference formula as, with h being the grid spacing,

$$\alpha_{\mathrm{d6}} f'_{i-\frac{1}{2}} + f'_{i+\frac{1}{2}} + \alpha_{\mathrm{d6}} f'_{i+\frac{3}{2}} = a_{\mathrm{di6}} \frac{\left(\bar{f}_{i+1} - \bar{f}_i\right)}{h} + b_{\mathrm{di6}} \frac{\left(\bar{f}_{i+2} - \bar{f}_{i-1}\right)}{h} \tag{20}$$

$$\alpha_{\mathrm{d6}} = \frac{9}{62}, \qquad a_{\mathrm{di6}} = \frac{63}{62}, \qquad b_{\mathrm{di6}} = \frac{17}{62}\,\frac{1}{3}$$

(B.1.1)[4]

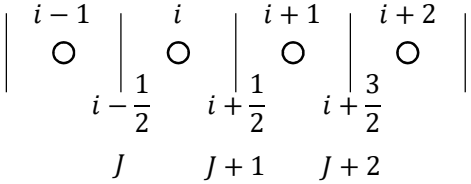

A 4th-order explicit formula is used for the boundary as

$$f'_{i+\frac{1}{2}} = a_{\mathrm{db4}} \frac{\left(\bar{f}_{i+1} - \bar{f}_i\right)}{h} + b_{\mathrm{db4}} \frac{\left(\bar{f}_{i+2} - \bar{f}_{i-1}\right)}{h} \tag{21}$$

$$a_{\mathrm{db4}} = \frac{9}{8}, \qquad b_{\mathrm{db4}} = -\frac{1}{8}\,\frac{1}{3}$$

(B.1.1)[4]

and is expressed explicitly at the boundaries as

$$f'_{-\frac{1}{2}} = a_{\mathrm{db4}} \frac{\left(\bar{f}_0 - \bar{f}_{-1}\right)}{h} + b_{\mathrm{db4}} \frac{\left(\bar{f}_1 - \bar{f}_{-2}\right)}{h}$$

$$f'_{N+\frac{1}{2}} = a_{\mathrm{db4}} \frac{\left(\bar{f}_{N+1} - \bar{f}_N\right)}{h} + b_{\mathrm{db4}} \frac{\left(\bar{f}_{N+2} - \bar{f}_{N-1}\right)}{h} \tag{22}$$

The resulting linear algebraic equation is

$$\begin{bmatrix} 1 & \alpha & & & \\ \alpha & 1 & \alpha & & \\ & \ddots & \ddots & \ddots & \\ & & \alpha & 1 & \alpha \\ & & & \alpha & 1 \end{bmatrix} \begin{bmatrix} f'_{\frac{1}{2}} \\ f'_{\frac{3}{2}} \\ \vdots \\ f'_{N-\frac{3}{2}} \\ f'_{N-\frac{1}{2}} \end{bmatrix} = \frac{1}{h} \begin{bmatrix} a(\bar{f}_1 - \bar{f}_0) + b(\bar{f}_2 - \bar{f}_{-1}) \\ a(\bar{f}_2 - \bar{f}_1) + b(\bar{f}_3 - \bar{f}_0) \\ \vdots \\ a(\bar{f}_{N-1} - \bar{f}_{N-2}) + b(\bar{f}_N - \bar{f}_{N-3}) \\ a(\bar{f}_N - \bar{f}_{N-1}) + b(\bar{f}_{N+1} - \bar{f}_{N-2}) \end{bmatrix} - \alpha \begin{bmatrix} f'_{-\frac{1}{2}} \\ 0 \\ \\ 0 \\ f'_{N+\frac{1}{2}} \end{bmatrix} \tag{23}$$

We solve the following equations, instead of solving the Eqs. (22)–(23),

$$\begin{aligned} \tilde{f}'_{-\frac{1}{2}} &= a_{\mathrm{db4}}(\bar{f}_0 - \bar{f}_{-1}) + b_{\mathrm{db4}}(\bar{f}_1 - \bar{f}_{-2}) \\ \tilde{f}'_{N+\frac{1}{2}} &= a_{\mathrm{db4}}(\bar{f}_{N+1} - \bar{f}_N) + b_{\mathrm{db4}}(\bar{f}_{N+2} - \bar{f}_{N-1}) \end{aligned} \tag{24}$$

$$\begin{bmatrix} 1 & \alpha & & & \\ \alpha & 1 & \alpha & & \\ & \ddots & \ddots & \ddots & \\ & & \alpha & 1 & \alpha \\ & & & \alpha & 1 \end{bmatrix} \begin{bmatrix} \tilde{f}'_{\frac{1}{2}} \\ \tilde{f}'_{\frac{3}{2}} \\ \vdots \\ \tilde{f}'_{N-\frac{3}{2}} \\ \tilde{f}'_{N-\frac{1}{2}} \end{bmatrix} = \begin{bmatrix} a(\bar{f}_1 - \bar{f}_0) + b(\bar{f}_2 - \bar{f}_{-1}) \\ a(\bar{f}_2 - \bar{f}_1) + b(\bar{f}_3 - \bar{f}_0) \\ \vdots \\ a(\bar{f}_{N-1} - \bar{f}_{N-2}) + b(\bar{f}_N - \bar{f}_{N-3}) \\ a(\bar{f}_N - \bar{f}_{N-1}) + b(\bar{f}_{N+1} - \bar{f}_{N-2}) \end{bmatrix} - \alpha \begin{bmatrix} \tilde{f}'_{-\frac{1}{2}} \\ 0 \\ \\ 0 \\ \tilde{f}'_{N+\frac{1}{2}} \end{bmatrix} \tag{25}$$

and apply the coordinate transformation of

$$f' = \xi_x \tilde{f}' = \frac{1}{h} \tilde{f}' \tag{26}$$

Here it is assumed that the directions of the coordinate axis of ξ and x are the same. Otherwise in general,

$$\frac{\partial f}{\partial x} = f' = \xi_x \frac{\partial f}{\partial \xi} + \eta_x \frac{\partial f}{\partial \eta} + \zeta_x \frac{\partial f}{\partial \zeta} \tag{27}$$

(151)[2]

The compact difference formula in this section can be used for the non-uniform grid spacing, by using the transformation formula of Eq. (26) or (27).

A4. Compact filter

The compact filter of the type of

$$\alpha_f \bar{q}^*_{i-1} + \bar{q}^*_i + \alpha_f \bar{q}^*_{i+1} = \sum_{j=0}^{N} a_{fj} \frac{\left(\bar{q}_{i-j} + \bar{q}_{i+j}\right)}{2} \tag{28}$$

(170)[2]

(15)[5]

is applied to the conservative variable vector $\boldsymbol{q} = [\rho, \rho\boldsymbol{u}, E]^{\mathrm{T}}$ in the upacs-LES, where $\bar{q}$ and $\bar{q}^*$ are the unfiltered and filtered cell-center variables, respectively. The coefficients α and a_j are given by the table below, which is a copy from the upacs-LES manual.[2]

Table A1 Coefficients of the compact Filter

order	a_{f0}	a_{f1}	a_{f2}	a_{f3}	a_{f4}	a_{f5}	a_{f6}	a_{f7}	α_f
14th	$\frac{1619+858\alpha_f}{2084}$	$\frac{3003+10378\alpha_f}{8192}$	$\frac{1001(-1+2\alpha_f)}{4096}$	$\frac{-1001(-1+2\alpha_f)}{8192}$	$\frac{91(-1+2\alpha_f)}{2048}$	$\frac{-91(-1+2\alpha_f)}{8192}$	$\frac{7(-1+2\alpha_f)}{4096}$	$\frac{1-2\alpha_f}{8192}$	0.235
12th	$\frac{793+462\alpha_f}{1024}$	$\frac{99+314\alpha_f}{256}$	$\frac{459(-1+2\alpha_f)}{2048}$	$\frac{-55(-1+2\alpha_f)}{512}$	$\frac{33(-1+2\alpha_f)}{1024}$	$\frac{-3(-1+2\alpha_f)}{512}$	$\frac{-1+2\alpha_f}{2048}$		0.425
10th	$\frac{193+126\alpha_f}{256}$	$\frac{105+302\alpha_f}{256}$	$\frac{-15+30\alpha_f}{64}$	$\frac{45-90\alpha_f}{512}$	$\frac{-5+10\alpha_f}{256}$	$\frac{1-2\alpha_f}{512}$			0.48
8th	$\frac{93+70\alpha_f}{128}$	$\frac{7+18\alpha_f}{16}$	$\frac{7(-1+2\alpha_f)}{32}$	$\frac{1-2\alpha_f}{16}$	$\frac{-1+2\alpha_f}{128}$				0.495
6th	$\frac{11+10\alpha_f}{16}$	$\frac{15+34\alpha_f}{32}$	$\frac{3(-1+2\alpha_f)}{16}$	$\frac{1-2\alpha_f}{32}$					0.4987
4th	$\frac{5+6\alpha_f}{8}$	$\frac{1+2\alpha_f}{2}$	$\frac{-1+2\alpha_f}{8}$						0.4997
2nd	$\frac{1+2\alpha_f}{2}$	$\frac{1+2\alpha_f}{2}$							0.49992

These filters acts as a low-pass filter in order to suppress the unphysical cell-to-cell numerical oscillation. The order of the filter is gradually shifted from the 14th order to the 2nd order near the boundary, reducing the required number of data points for the filtering from 15 (14th order case) to 3 (2nd order case). Here, the term boundary means the numerical boundary in the ghost cells or the overlapping cells, as shown in the figure below, which is also a copy from the the upacs-LES manual.[2]

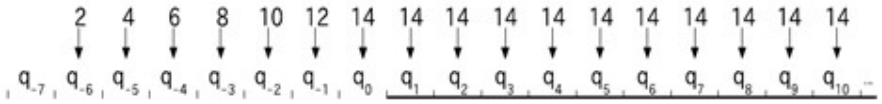

Figure 1 Order of the filter near the block boundary

On the other hand, the following parameters are specified in the setup file of upacs-LES.txt that has been used in our laboratory.

```
boundary_points = 6

filter_new_maximum_order = 10
```

Therefore in this case the relationship between the boundary points and filter order is given by

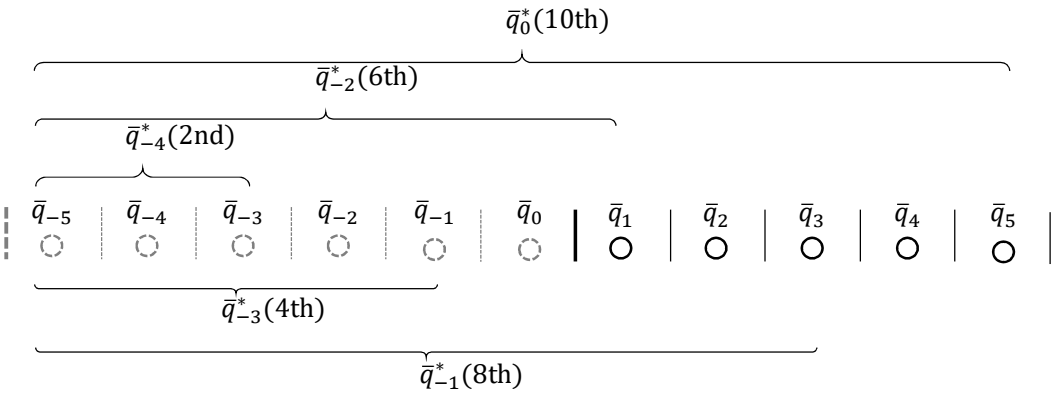

for the left-hand side boundary and

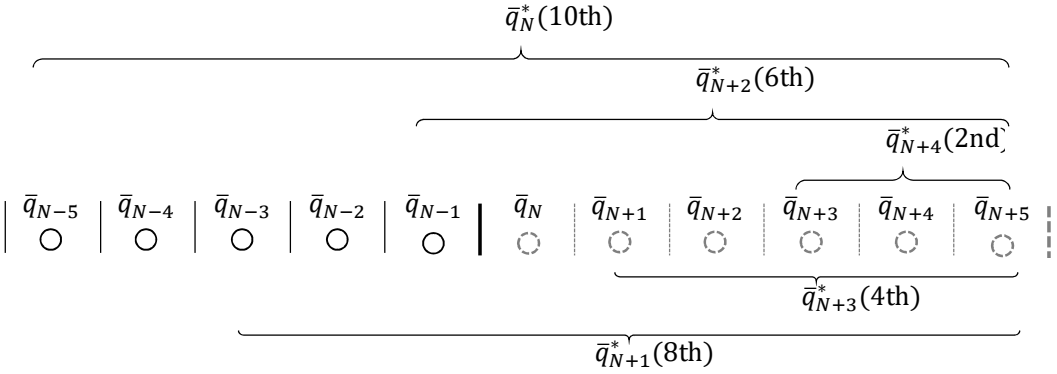

for the right-hand side boundary. Therefore, the resulting equation to be solved is given by

$$\begin{bmatrix} 1 & \alpha & & & \\ \alpha & 1 & \alpha & & \\ & \ddots & \ddots & \ddots & \\ & & \alpha & 1 & \alpha \\ & & & \alpha & 1 \end{bmatrix} \begin{bmatrix} \bar{q}_{-4}^* \\ \bar{q}_{-3}^* \\ \vdots \\ \bar{q}_{N+3}^* \\ \bar{q}_{N+4}^* \end{bmatrix} = \begin{bmatrix} \sum_{j=0}^{N=1} a_{fj}^{2\mathrm{nd}} \frac{(\bar{q}_{-4-j} + \bar{q}_{-4+j})}{2} \\ \sum_{j=0}^{N=2} a_{fj}^{4\mathrm{th}} \frac{(\bar{q}_{-3-j} + \bar{q}_{-3+j})}{2} \\ \vdots \\ \sum_{j=0}^{N=2} a_{fj}^{4\mathrm{th}} \frac{(\bar{q}_{N+3-j} + \bar{q}_{N+3+j})}{2} \\ \sum_{j=0}^{N=1} a_{fj}^{2\mathrm{nd}} \frac{(\bar{q}_{N+4-j} + \bar{q}_{N+4+j})}{2} \end{bmatrix} - \alpha \begin{bmatrix} \bar{q}_{-5} \\ 0 \\ \\ 0 \\ \bar{q}_{N+5} \end{bmatrix} \tag{29}$$

The filtering formula in this section can be applied exactly to the uniform grid spacing, as in the case of interpolation formula, due to the same reason described in Section 1. But compact filter is widely used in non-uniform grids in the FDM community.

References

[1] Pletcher, R.H., et al., "Computational Fluid Mechanics and Heat Transfer (3rd edition) ", CRC Press, 2013.

[2] Enomoto, S., "upacs-LES Users Guide", Japan Aeroscape Exploration Agency, 2011. (in Japanese)

[3] Kobayashi, M. H., "On a Class of Pade Finite Volume Methods", Journal of Computational Physics 156, pp.137–180, 1999.

Appendix B: Boundary conditions in the solver upacs-LES

B1. Notations

The equation and figure numbers in this document are those appeared in the Japanese upacs-LES manual [1]. In addition, equations in this document are labeled as (A1), (A2), …, and so on. In the later part of section 3 and the whole part of section 5, notations for mathematical variables follow the Fortran 90 program in upacs-LES source code, because there are no description in the manual. The mass-flow specified boundary conditions in section 6 are taken from the separate source [3], and notations in section 6 follow the reference [3].

B2. Summary of the theory of characteristics

The hyperbolic system of equations such as the Euler equations can be decomposed into uncoupled equations by diagonalizing the Jacobian matrix of the system. The resulting uncoupled equations describes the propagation of the Riemann variables with the propagation speed of the eigenvalues of the Jacobian matrix of the system. The propagation paths are called the characteristic lines. If the governing equations are linear then the characteristic lines are straight lines. When we focus on the left eigenvectors of the Jacobian matrix of the system, we can find the Riemann invariants that is conserved along the characteristic lines. However speaking in strictly, there are no such invariants in multi-dimensional problems. Even in this case we can find the quantities that are conserved across the characteristic line by considering the right eigenvectors of the Jacobian matrix of the system. Refer to the textbook [2] for more detail.

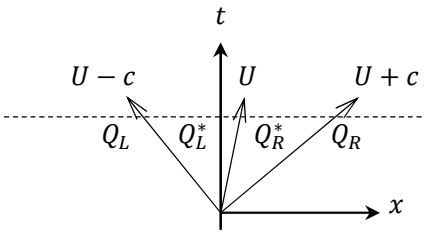

Figure 4: Definition of left and right states.

The quantities below are conserved across the characteristic lines of $dx/dt = U - c, U, U + c$.

$c_L + \frac{\gamma+1}{2} U_L = c_L^* + \frac{\gamma+1}{2} U_L^*$ $\frac{p_L}{(\rho_L)^\gamma} = \frac{p_L^*}{(\rho_L^*)^\gamma}$	across the characteristic line $U - c$	(A1)
$U_L^* = U_R^*$ $p_L^* = p_R^*$	across the characteristic line U	
$c_R^* - \frac{\gamma-1}{2} U_R^* = c_R - \frac{\gamma-1}{2} U_R$ $\frac{p_R^*}{(\rho_R^*)^\gamma} = \frac{p_R}{(\rho_R)^\gamma}$	across the characteristic line $U + c$	

where

$$c = \sqrt{(\gamma - 1)\left(H - \frac{1}{2}\boldsymbol{u} \cdot \boldsymbol{u}\right)}, \qquad U = \boldsymbol{n} \cdot \boldsymbol{u}, \tag{A2}$$

are the speed of sound and normal velocity, and

$\boldsymbol{n}$: inward-pointing unit normal vector on the boundary

γ: specific heat ratio (A3)

B3. Subsonic inflow B. C. (entry_subsonic_riemann, entry_subsonic)

The upacs-LES manual says that this B. C. cannot be used with the compact scheme

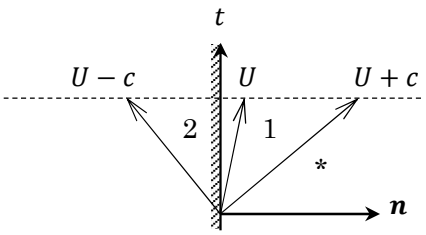

Figure 7: Inflow boundary

Across the $U + c$ characteristic line,

$$\begin{aligned} c_* - \frac{\gamma - 1}{2} U_* &= c_1 - \frac{\gamma - 1}{2} U_1 \,, \\ \frac{p_*}{{\rho_*}^\gamma} &= \frac{p_1}{{\rho_1}^\gamma}, \\ \mathbf{n} \times \mathbf{u}_* &= \mathbf{n} \times \mathbf{u}_1 \,, \end{aligned} \tag{A4}$$

where values with subscript * are known from the inner points. Across the U characteristic line,

$$\begin{aligned} U_1 &= U_2 \,, \\ p_1 &= p_2 \,. \end{aligned} \tag{A5}$$

The rest of the boundary conditions are givens as the physical boundary conditions as

$$\begin{aligned} \frac{c_2^2}{\gamma - 1} + \frac{1}{2} U_2 &= \text{total enthalpy } H_2 = \text{given as physical B.C.} \,, \\ \frac{p_2}{{\rho_2}^\gamma} &= \text{entropy } s_2 = \text{ given as physical B.C.} \,, \\ \boldsymbol{n} \times \boldsymbol{u}_2 &= \text{velocity paralell to the boundary} = \text{ given as physical B.C.} \,. \end{aligned} \tag{A6}$$

There are 12 unknowns of $c_1,\ p_1,\ \rho_1,\ \boldsymbol{u}_1,\ c_2,\ p_2,\ \rho_2,\ \boldsymbol{u}_2$ and 12 equations (U_i can be obtained from $U_i = \boldsymbol{n} \cdot \boldsymbol{u}_i$).

When we do not use the concept of the characteristic variable, the total enthalpy H_2, the entropy s_2, the total density ρ_{t2}, and the unit flow vector $\boldsymbol{n}_u$ are given at the inflow boundary and boundary conditions for this case are given by

$$
\begin{gathered}
p_* = \text{calculated from the inner point} \\
p_2 = p_* \\
p_{t2} = s_2 {\rho_{t2}}^{\gamma} \\
\text{if } (p_2 > p_{t2})\ p_{t2} = p_2 \\
M_2^2 = \frac{1}{\gamma - 1}\left(\left(\frac{p_{t2}}{p_2}\right)^{\frac{\gamma-1}{\gamma}} - 1\right) \\
\theta = 1 + \frac{\gamma - 1}{2} M_2^2 \\
T_{t2} = H_2 \frac{\gamma - 1}{\gamma} \\
T_2 = \frac{T_{t2}}{\theta} \\
c_2^2 = \gamma T_2 \\
p_{t2} = p_2\, \theta^{\frac{\gamma}{\gamma-1}} \\
\rho_{2t} = p_{t2}/T_{t2} \\
\rho_2 = \rho_{2t} \theta^{-\frac{1}{\gamma-1}} \\
U_2 = \sqrt{M_2^2 c_2^2} \\
\boldsymbol{u}_2 = U_2 \boldsymbol{n}_u\ .
\end{gathered}
\tag{A7}
$$

B4. Subsonic outflow B. C. (exit_subsonic)

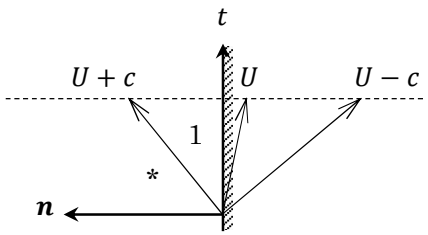

Figure 6: Outflow boundary

Because the unit normal vector $\boldsymbol{n}$ points inward, the normal velocity component $U = \boldsymbol{n} \cdot \boldsymbol{u}$ for the outflow is negative against the $\boldsymbol{n}$ direction. The incoming characteristics is $U + c$ in this case. Therefore across the $U + c$ characteristics[1]

$$\begin{aligned} c_* - \frac{\gamma - 1}{2} U_* &= c_1 - \frac{\gamma - 1}{2} U_1 \,, \\ \frac{p_*}{{\rho_*}^\gamma} &= \frac{p_1}{{\rho_1}^\gamma} \,, \\ \boldsymbol{n} \times \boldsymbol{u}_* &= \boldsymbol{n} \times \boldsymbol{u}_1 \,, \end{aligned} \tag{A8}$$

where values with subscript * are known from the inner points, as before. As a physical boundary condition, we can specify the outlet static pressure, p_{out}.

$$\begin{aligned} \rho_1 &= \left[p_{\text{out}} / \left(\frac{p_*}{{\rho_*}^\gamma} \right) \right]^{1/\gamma} \,, \\ U_1 &= \frac{2}{\gamma - 1} \left[\sqrt{\frac{\gamma p_1}{\rho_1}} - \left(c_* - \frac{\gamma - 1}{2} U_* \right) \right], \\ \boldsymbol{u}_1 &= U_1 \boldsymbol{n} + (\boldsymbol{n} \times \boldsymbol{u}_*) \times \boldsymbol{n} \,. \end{aligned} \tag{A9}$$

[1] If we choose the outward normal as the positive direction, the relation $c_* + (\gamma - 1)U_*/2 = c_1 + (\gamma - 1)U_1/2$ holds across the $U - c$ characteristics. This relationship is the same with Eq. (159), because the sign of the U changes according to the definition.

B5. Farfield B. C. (farfield_subsonic)

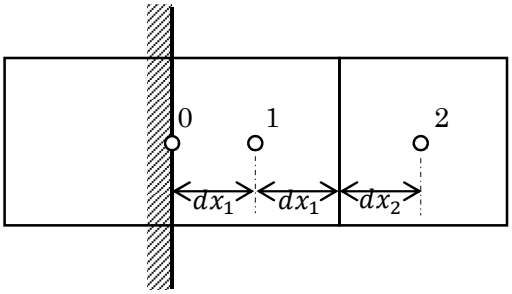

Figure X1: Points used for the extrapolation

The freestream Mach number M_∞, the unit flow vector $\boldsymbol{n}_u$, the pressure p_∞, and the temperature T_∞ are given at the farfield boundary. Then,

$$c_\infty = \sqrt{\frac{\gamma p_\infty}{\rho_\infty}}, \qquad \boldsymbol{u}_\infty = c_\infty M_\infty \boldsymbol{n}_u \,. \tag{A10}$$

The values on the boundary, which are denoted by the subscript 0, are roughly estimated by using the first order extrapolation from the inner points shown in Figure X1.

$$\begin{aligned} \tilde{\rho}_0 &= \rho_1 + dx_1(\rho_1 - \rho_2)/(dx_1 + dx_2)\,, \\ \tilde{\boldsymbol{u}}_0 &= \boldsymbol{u}_1 + dx_1(\boldsymbol{u}_1 - \boldsymbol{u}_2)/(dx_1 + dx_2)\,, \\ \tilde{p}_0 &= p_1 + dx_1(p_1 - p_2)/(dx_1 + dx_2)\,. \end{aligned} \tag{A11}$$

The direction of the $U - c$ characteristic wave is negative against the inward normal vector at the boundary. Therefore the Riemann invariant along the $U - c$ characteristic line can be determined from the inner point variables as

$$\Psi_{\text{inner}} = \sqrt{\frac{\gamma \tilde{p}_0}{\tilde{\rho}_0}} - \frac{\gamma - 1}{2} \boldsymbol{n} \cdot \tilde{\boldsymbol{u}}_0 \,, \tag{A12}$$

and the Riemann invariant along the $U + c$ characteristic wave can be determined from the farfield variables as

$$\Psi_\infty = \sqrt{\frac{\gamma p_\infty}{\rho_\infty}} + \frac{\gamma - 1}{2} \boldsymbol{n} \cdot \boldsymbol{u}_\infty \,. \tag{A13}$$

Therefore the speed of sound and the normal velocity on the boundary, at which these two waves cross, can be obtained from

$$\begin{aligned} c_0 &= \frac{\Psi_\infty + \Psi_{\text{inner}}}{2}, \\ U_0 &= \frac{\Psi_\infty - \Psi_{\text{inner}}}{\gamma - 1}. \end{aligned} \tag{A14}$$

When the farfield boundary is an inflow boundary, the entropy and the vorticity waves are given by the farfield information (because these waves are conserved along the U characteristic line) as

$$\begin{aligned} s_0 &= \frac{p_\infty}{{\rho_\infty}^\gamma}, \\ \boldsymbol{V}_0 &= \boldsymbol{n} \times \boldsymbol{u}_\infty \,. \end{aligned} \tag{A15}$$

On the other hand, when the farfield boundary is an outflow boundary, these waves should be calculated from the inner points (because these waves are conserved along the U characteristic line) as

$$\begin{aligned} s_0 &= \frac{\tilde{p}_0}{{\tilde{\rho}_0}^\gamma}, \\ \boldsymbol{V}_0 &= \boldsymbol{n} \times \tilde{\boldsymbol{u}}_0 \,. \end{aligned} \tag{A16}$$

As a result, the boundary conditions are given by

$$\rho_0 = \left(\frac{c_0^2}{\gamma s_0} \right)^{\frac{1}{\gamma - 1}}, \tag{A17}$$

$$p_0 = \frac{\rho_0 c_0^2}{\gamma},$$

$$\boldsymbol{u}_0 = U_0 \boldsymbol{n} + \boldsymbol{V}_0 \times \boldsymbol{n} \ .$$

B6. Mass-flow specified B. C.

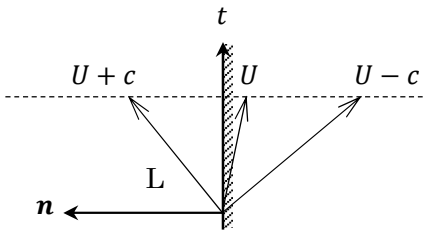

Figure 6: Outflow boundary

Dr. Yamamoto, the leader of the UPACS team, recently developed a mass-flow specified B. C. for the non-LES version of the UPACS [3]. When the mass flow per unit area at the outflow boundary is specified as $\dot{m}_{\mathrm{BC}}$, the physical boundary condition is expressed as

$$\begin{aligned} \rho_{\mathrm{B}} U_{\mathrm{B}} &= \dot{m}_{\mathrm{BC}} \,, \\ U_{\mathrm{B}} &= \boldsymbol{n} \cdot \boldsymbol{u}_{\mathrm{B}} \,, \end{aligned} \tag{A18}$$

where the subscript B denotes the boundary. As in the section 4 of this document[2],

$$\begin{aligned} c_{\mathrm{B}} - \frac{\gamma - 1}{2} U_{\mathrm{B}} &= c_{\mathrm{L}} - \frac{\gamma - 1}{2} U_{\mathrm{L}} \,, \\ \frac{p_B}{{\rho_B}^{\gamma}} &= \frac{p_L}{{\rho_L}^{\gamma}} \,, \\ \boldsymbol{n} \times \boldsymbol{u}_{\mathrm{B}} &= \boldsymbol{n} \times \boldsymbol{u}_{\mathrm{L}} \,, \end{aligned} \tag{A19}$$

,

[2] In the original equation in the reference[3], the positive direction is taken to be outward, and $c_{\mathrm{B}} + (\gamma - 1) U_{\mathrm{B}}/2 = c_{\mathrm{L}} + (\gamma - 1) U_{\mathrm{L}}/2$, where U_{B} and U_{L} are positive.

where the subscript L denotes the left state, which is the known state of the inner points. Then, we have 6 unknowns of ρ_{B}, $\boldsymbol{u}_{\mathrm{B}}$, p_B, c_{B} and 6 equations, and we can solve these equations, for example, for ρ_{B}. In addition, the relaxation method is used in reference [3], in order to dump the acoustic reflections as

$$\rho_{\mathrm{B}} U_{\mathrm{B}} = \frac{\dot{m}_{\mathrm{BC}} + \alpha(\rho_{\mathrm{L}} U_{\mathrm{L}})}{1+\alpha}, \tag{A20}$$

where $\alpha \geq 0$ is the adjustable parameter.

B7. Farfield B. C. as a mass-flow specified B. C.

Because the farfield boundary conditions specify the Mach number or the velocity at the farfield boundary, it is considered to be a kind of mass-flow specified boundary condition. In this section, the farfield B. C. in section 5 and the mass-flow specified B. C. in section 6 will be compared. Although the farfield boundary conditions include both the inflow and outflow conditions, only the outflow conditions are considered here.

The values on the boundary are expressed with the subscript 0 in section 5 and the subscript B in section 6. These expressions are unified as the subscript B in this section. Also, the values from the inner points are expressed as $\tilde{}_0$ in section 5 and expressed with the subscript L in section 6. These expressions are unified as the subscript L in this section.

Then, the conditions for the entropy and vorticity, from Eqs. (A16) and (A19), are the same between these two boundary conditions.

$$\frac{p_B}{{\rho_B}^{\gamma}} = \frac{p_L}{{\rho_L}^{\gamma}}, \tag{A16)'}$$

$$\boldsymbol{n} \times \boldsymbol{u}_{\mathrm{B}} = \boldsymbol{n} \times \boldsymbol{u}_{\mathrm{L}}. \tag{A19)'}$$

By using Eq. (A14) in the far-field B. C., we obtain

$$\begin{aligned} c_{\mathrm{B}} - \frac{\gamma-1}{2} U_{\mathrm{B}} &= c_{\mathrm{L}} - \frac{\gamma-1}{2} U_{\mathrm{L}}, \\ c_{\mathrm{B}} + \frac{\gamma-1}{2} U_{\mathrm{B}} &= c_{\infty} + \frac{\gamma-1}{2} U_{\infty}. \end{aligned} \tag{A14)'}$$

The former equation is the same with Eq. (A19) in the mass-flow specified B. C..
Therefore the following relationships are the same between these two boundary conditions

$$c_{\mathrm{B}} - \frac{\gamma-1}{2} U_{\mathrm{B}} = c_{\mathrm{L}} - \frac{\gamma-1}{2} U_{\mathrm{L}} ,$$
$$\frac{p_B}{{\rho_B}^{\gamma}} = \frac{p_L}{{\rho_L}^{\gamma}} , \qquad \text{(A19)}$$
$$\boldsymbol{n} \times \boldsymbol{u}_{\mathrm{B}} = \boldsymbol{n} \times \boldsymbol{u}_{\mathrm{L}} .$$

The equation that is found only in the far-field boundary condition is

$$c_{\mathrm{B}} + \frac{\gamma-1}{2} U_{\mathrm{B}} = c_{\infty} + \frac{\gamma-1}{2} U_{\infty} . \qquad \text{(A14)'}$$

The equation that is found only in the mass-flow specified boundary condition is

$$\rho_{\mathrm{B}} U_{\mathrm{B}} = \dot{m}_{\mathrm{BC}} . \qquad \text{(A18)'}$$

Although the far-field Mach number, pressure, and temperature are specified as boundary conditions in the far-field B. C. in section 5, they are not fixed but are solved, as in Eq. (A17), by considering the incoming and outgoing characteristic waves, while preventing the artificial reflection from the boundary. As a result, the mass flow through this boundary is slightly changing, depending on the waves passing the boundary.

On the other hand, the mass-flow specified B. C. in section 6 fixes the mass flow at the boundary, which produces the artificial reflection from the boundary. Therefore this B. C. requires the additional relaxation procedure of Eq. (A20) to reduce the reflection.

References

[1] Enomoto, S., "upacs-LES Users Guide", Japan Aerospace Exploration Agency, 2011.
[2] Laney, C.B., "Computational Gasdynamics, Chapter 3 Waves", Cambridge University Press, 1998.
[3] Yamamoto, K.,et al., "A mass flow boundary condition for compressible flow computations", Proceedings of the 45th Fluid Dynamics Conference/ Aerospace Numerical Simulation Symposium, 2013, Funahori, Japan, July 4-5, JSASS-2013-2039-A (7 pages) (in Japanese).

Appendix C: Two Microphone Method Matlab code

The matlab code used to calculate the absorption coefficient from the numerical results is made of three files the main file named “main_2MM_20140710”, the file calculating the cross spectrum named “F_cross_work4ver2.m” and file converting the input data from CSV to MAT named “CSV2MAT_octave.m”

main_2MM_20140710.m

```
% this program processes only one data file which contains the single tone
data
% and produces absorption coefficient data against the whole frequency
range
%

% clear all;
% close all;

currentFolder = pwd;
outputname1 = strcat(currentFolder,'¥output.txt');
fprintf('Output file name = %s¥n', outputname1);

fout1 = fopen(outputname1,'w');
fprintf(fout1,'Frequency Alpha¥r¥n');

s = 1;

for ia=1:s

    MF = load('raw_data_Grid.mat'); % *** EXPLICITLY SPECIFIED FOR THIS TEST
CASE ***

    time = MF.Time_24000Hz';
    delta_t = time(2) - time(1);

    p1 = MF.Ch1';
    p2 = MF.Ch2';

    f_samp = 1 / delta_t;
    N_res = 40; %resolution
    overlap = 0; % overlap, percent
    nave = floor(size(p1,1) / (N_res * (1 - overlap / 100))); % number of
average
    fprintf('nave = %d¥n', nave);

    fprintf('number of data points = %d¥n', size(p1,1));
    fprintf('sampling frequency = %d¥n', f_samp);
    fprintf('number of average = %d¥n', nave);

    H = F_cross_work4ver2(N_res, nave, overlap, p1, p2);

    delta_f = f_samp / N_res;
    fprintf('frequency resolution = %3.1f¥n', delta_f);

    % frequency
    N_res2 = floor(N_res / 2);
    for k=1:N_res2
        f(k,1) = (k-1) * f_samp / N_res;
```

```
    end

    %microphone positions
    x1 =0.2177852348993  ; %[m]
    x2 =0.1483557046980; %[m]

    fprintf('maximum frequency = %d¥n', max(f));
    fprintf('number of data = %d¥n', size(f));

    s = x1 - x2; %distance between two microphones[m]

    i = sqrt(-1); %imaginary unit

    theta = 20; %temperature [degrees Celcius]
    T = theta + 273.15; %temperature [K]
    c = 343.2020833; %sped of sound [m/s]


    % wave number
    k = 2 * pi * f / c;

    % transfer function for the incident wave
    H_I = exp(-i * k * s);

    % transfer function for the reflected wave
    H_R = exp(i * k * s);

    % transfer function of the sound field of the standing wave
    H_12 = H;

    % reflection coefficient, r
    r = ((H_12 - H_I) ./ (H_R - H_12)) .* exp(2 * i * k * x1);
    test=exp(-2 * i * k * x1);
    alpha = 1 - abs(r).^2;

    % plotting the absorption coefficient
hold on;
    figure(3);
    plot(f,alpha,'b.');
    hold on;
    xlabel('frequency [Hz]');
    ylabel('alpha');
    axis([0 2500 -1 1]);
    grid on;
    hold on;

    for k = 1 : N_res2
      fprintf(fout1,'%.4f %.4f¥r¥n',f(k,1), alpha(k));
    end

end


fclose(fout1);
```

F_cross_work4ver2.m

```
% N_res : resolution
% nave : number of average
% overlap : overlap of the data in percent
% ttp1 : reference signal
% ttp2 : measured signal


function y = F_cross_work4ver2(N_res, nave, overlap, ttp1, ttp2);


% (2-3) allocation of the arrays refave conave pcalc
transave=zeros(N_res,1); % integrated value
pcalc=zeros(N_res,1);    % instantaneous cross-spectrum, or, pressure signal
of the segmented data

ovpointer=floor((1-overlap/100)*N_res);


% (2-4) FFT for NCALC CASE
for jj=1:nave,  % --Averaging of ii_th Time Data
    kstart=(jj-1)*ovpointer;

    % (2-4-1) Reference Data Analysis
    for kk=1:N_res,
       pcalc(kk,1) = ttp1(kstart+kk,1);
    end

    % FFT of jj_th Segment
    fftref = fft(pcalc , N_res) / N_res;
    fftref = fftref / sqrt(2);

    % (2-4-2) Concerning Data Analysis
    for kk=1:N_res,
       pcalc(kk,1) = ttp2(kstart+kk,1);
    end

    % FFT of jj_th Segment
    fftcon = fft(pcalc , N_res) / N_res;
    fftcon = fftcon / sqrt(2);

    % (2-4-3) Computation of Cross Spectrum
%     pcalc = fftcon ./ fftref;
    cros = fftcon .* conj(fftref);
    auto = fftref .* conj(fftref);
    trans = cros ./ auto;

    % (2-4-4) integration of the Cross Spectrum
    transave = transave + trans;

end

% (2-4-5) averaging of the Cross Spectrum
transave = transave / nave;

N_res2 = floor(N_res / 2);
```

```
y = transave(1:N_res2, 1);
%=======================
```

CSV2MAT_octave.m

```
%=======================
%=this file converts the input data from CSV to MAT

pwd

input_file = 'raw_data_Grid.csv';
output_file =  strrep( input_file, '.csv', '.mat'  );

fprintf('input CSV file = %s¥n', input_file);

matrix = csvread(input_file);

Time_24000Hz = matrix(:,1)';
Ch1 = matrix(:,2)';
Ch2 = matrix(:,3)';

save (output_file, 'Time_24000Hz', 'Ch1', 'Ch2');

whos ('-file', output_file);
```